

CRACOW UNIVERSITY OF TECHNOLOGY

FACULTY OF CIVIL ENGINEERING

INSTITUTE FOR COMPUTATIONAL CIVIL ENGINEERING



DOCTORAL THESIS

Large strain thermomechanical
material models
accounting for inelasticity, instabilities
and gradient enhancement

Author:
Balbina WCISŁO, MSc

Supervisor:
Jerzy PAMIN, PhD, prof. of CUT

Cracow, 2017



Acknowledgement

I would like to express my sincere gratitude to my supervisor Professor Jerzy Pamin for his guidance, many inspiring discussions, motivation and patience during this doctoral project.

I would like to acknowledge valuable talks on the research with Dr. K. Kowalczyk-Gajewska and Dr. J. Lengiewicz from IPPT Warsaw, as well as with Prof. A. Menzel from TU Dortmund/Lund University.

I thank my family for invaluable constant support.

The research was carried out in years 2011-2014 within the grant "Doctus - Malopolska scholarships fund for PhD students". The financial support of the National Science Centre of Poland within the project "Numerical analysis of instabilities of isotropic thermo-plastic material at large strain" (grant number 2014/15/B/ST8/01322) started in the year 2015 is also gratefully acknowledged.

Contents

Acknowledgement	3
Contents	7
Abstract	9
Notation	11
1 Introduction	15
1.1 Motivation and objective of the research	15
1.2 Scope of the work	16
2 Large strain problem	19
2.1 Grounds of large strain kinematics	19
2.2 Measures of deformation	20
2.2.1 Deformation gradient	20
2.2.2 Deformation and strain tensors	21
2.3 Stress measures	21
2.4 Time derivatives	22
2.5 Work conjugacy	23
3 Instabilities	25
3.1 Introduction	25
3.2 Material instability	26
3.2.1 Small strain problem	26
3.2.2 Large strain problem	28
3.2.3 Pilot results for ellipticity verification	29
3.3 Thermal softening	31
3.4 Geometrical effects	33
4 Computational approach	37
4.1 Preliminaries	37
4.2 Symbolic–numerical tools	38
4.3 General procedure for user finite element subroutine	39

5	Isothermal inelastic models	43
5.1	Kinematics and constitutive description of local models	43
5.1.1	Multiplicative split of deformation gradient for elasto-plasticity . .	43
5.1.2	Finite elasto-plasticity	43
5.1.3	Finite elasto-plasticity with damage	45
5.1.4	Finite elasto-plasticity with degradation	46
5.2	Gradient enhancement	47
5.3	Governing equations	49
5.4	Aspects of implementation within AceGen	50
5.4.1	Computational approach for isothermal models coupled with gradi- ent averaging	50
5.4.2	Finite element types	51
5.5	Algorithms for isothermal models solved in AceGen	52
5.5.1	Solution of finite elasto-plasticity	52
5.5.2	Solution of nonlocal finite elasto-plasticity with damage	53
5.5.3	Solution of nonlocal finite elasto-plasticity with degradation	54
5.6	Numerical simulations	55
5.6.1	Nonlocal finite elasto-plasticity with damage	55
5.6.2	Nonlocal finite elasto-plasticity with degradation	66
6	Local thermomechanical model	73
6.1	General remarks	73
6.2	Description of thermo-elasto-plastic model	74
6.2.1	Kinematics for non-isothermal problem	74
6.2.2	Free energy functional for thermomechanical problem	75
6.2.3	Description of thermo-plasticity	76
6.2.4	Constitutive model for heat conduction	76
6.2.5	Energy balance equation	77
6.3	Implementation of local thermomechanical model	77
6.4	Numerical simulations	79
6.4.1	Simulation of circular bar necking	79
6.4.2	Simulation of plate in tension – influence of heat conductivity . . .	83
6.4.3	Simulation of plate in tension – influence of rate of deformation process	87
7	Nonlocal thermomechanical models	91
7.1	Introduction	91
7.2	Description of nonlocal models	92
7.2.1	Model with temperature averaging	92
7.2.2	Thermomechanical extension of nonlocal elasto-plasticity with de- gradation	92
7.3	Implementation of nonlocal thermomechanical models	93
7.4	Numerical simulations	93
7.4.1	Thermo-elasto-plasticity with temperature averaging	93
7.4.2	Nonlocal thermo-elasto-plasticity with degradation	98

8 Final remarks	105
8.1 Summary and conclusion	105
8.2 Prospects of future work	107
Appendix A	109
Appendix B	113
Appendix C	115
Bibliography	116
Summary (in Polish)	125

Abstract

This thesis deals with the development and the numerical verification of large strain inelastic models in isothermal and non-isothermal conditions. The presented descriptions can reproduce the softening behaviour of materials resulting from three sources: geometrical effects, material degradation and thermal influence, all of which are discussed in the dissertation. The models can be used to simulate the behaviour of metals and isotropic composites, however, they are not directly focused on a specific material.

Each presented model is numerically tested using the finite element method implemented within the symbolic-numerical packages working in *Wolfram Mathematica*. The user-supplied subroutines are developed in code generator *AceGen* whereas package *AceFEM* is used for the simulations of selected benchmarks. The employed software, capable of automatic differentiation, significantly improves the process of the code development, however, to obtain efficient subroutines particular algorithms are developed and presented in the thesis. The benchmark tests are performed for elongated samples, in particular: a perforated plate, a rectangular plate in plane strain conditions, and a bar with circular or variable rectangular cross-section.

In the isothermal case two gradient-enhanced material models are proposed. The first model covers nonlocal elasto-plasticity with damage acting on the elastic part of the free energy potential. The second one is nonlocal elasto-plasticity with degradation of the yield strength. In both cases the implicit gradient averaging of the variable responsible for softening is included. A few aspects of the analyzed models are investigated: the influence of the adopted finite elements on the results, the response of the material for different strain measures governing damage, the comparison of spatial and material averaging and, finally, the effect of the selected yield criterion on the damage growth.

The core part of the dissertation is related to finite thermo-plasticity. The presented material model involves thermal expansion, the production of heat due to plastic dissipation, thermal softening, understood as the reduction of the yield strength with increasing temperature, and the influence of geometry change on the heat flux. In numerical simulations special attention is paid to the regularizing effect of heat conduction.

Finally, two thermomechanical nonlocal models are presented: thermo-plasticity with gradient averaging of the temperature increase responsible for thermal softening and nonlocal thermo-plasticity coupled with degradation of the yield strength. The numerical verification of these material descriptions focuses on the influence of the adopted internal length scales, which result from implicit gradient averaging, on the material response when internal adiabaticity is assumed. Moreover, the simultaneous

application of the internal length scale and the heat conductivity leads to the simulation of an evolving shear band.

The conclusion includes some final remarks and prospects of future work.

Keywords: *large strains, instabilities, inelasticity, gradient averaging, thermomechanical coupling, AceGen package*

Notation

The following notation is used in the dissertation:

- normal Greek or Latin letters for scalars
- bold-face Greek or Latin letters for vectors and second-order tensors
- upper case letters for variables referred to Lagrangian coordinates and lower case letters for variables referred to Euler coordinates
- variables referred to the previous time moment are denoted with subscript n , those referred to current time are without subscription
- the following superscripts denote that the quantities are related to: d – damage, e – elasticity, p – plasticity, θ – thermal influence

Latin letters

Symbol	Description
a	area in current configuration
A	area in reference configuration
\mathbf{b}	left Cauchy-Green deformation tensor
\mathbf{B}	acceleration field (body force)
\mathcal{B}	deformable continuous body
c	heat capacity at constant deformation
\mathbf{C}	right Cauchy-Green deformation tensor
\mathbf{d}	rate of deformation tensor
\mathbf{d}_{el}	vector of fields interpolated in finite element
\mathbb{D}	material tangent (fourth order tensor)
\mathbf{e}	Eulerian (or Almansi) strain tensor
\mathbf{E}	Lagrangian (or Green) strain tensor
f	stress measure governing plasticity
\mathbf{f}	relative deformation gradient
F	damage or plasticity function (distinguished by superscript)
\mathbf{F}	deformation gradient
\mathbf{F}^m	mechanical part of deformation gradient
G	shear modulus
h	hardening function
h_{conv}	convection coefficient

H	linear hardening modulus
H_T	thermal softening modulus
\mathbf{I}	second order identity tensor
J	determinant of deformation gradient (Jacobian)
J_{xG}	Jacobian of isoparametric mapping from 'parent' element to element in current configuration
J_{XG}	Jacobian of isoparametric mapping from 'parent' element to element in reference configuration
k	heat conduction coefficient
K	bulk modulus
\mathbf{K}	tangent matrix for Newton-Raphson procedure
l	internal length scale
\mathcal{L}_v	Lie derivative
\mathbf{n}	vector normal to surface in current configuration
\mathbf{N}	vector normal to surface in reference configuration
\mathbf{N}^p	derivative of plasticity function with respect to stress tensor
\mathbf{N}_I	vector of interpolation functions for finite element
\mathbf{p}	vector of element unknowns
\mathbf{P}	first Piola-Kirchhoff stress tensor
\mathbf{q}	Kirchhoff heat flux
\mathbf{Q}	acoustic tensor
\mathbf{R}	residual vector for Newton-Raphson procedure
\mathcal{R}	heat source density
\mathbf{S}	second Piola-Kirchhoff stress tensor
t	time
T	absolute temperature
T_0	referential temperature
T_∞	temperature of surrounding medium
\mathbf{T}_I	vector of nodal temperatures for finite element
\mathbf{u}	displacement
\mathbf{u}_I	vector of nodal displacements for finite element
v	volume in current configuration
\mathbf{v}	velocity
V	volume in reference configuration
w_g	Gauss point weight
\mathbf{x}	vector of current position of particle
\mathbf{X}	vector of initial position of particle
z	nonlocal variable
z_{loc}	local counterpart of z
\mathbf{z}_I	vector of nodal values of nonlocal variable for finite element

Greek letters

α^d	damage evolution law parameter
α_p	material constant for Burzyński-Drucker-Prager yield function
α_T	coefficient of linear thermal expansion
β	ductility parameter for plastic degradation
β^d	damage evolution law parameter
γ	measure of plastic strain
δ	saturation parameter for hardening function
$\delta \cdot$	test function
$\partial \mathcal{B}$	boundary of body \mathcal{B}
ε	small strain tensor
$\tilde{\varepsilon}$	measure of strain which governs damage
η	entropy
κ	history parameter for damage or plastic degradation (distinguished by superscript)
λ	load multiplier
$\dot{\lambda}$	plastic multiplier
ν	Poisson ratio
Π	potential density per unit volume
Π_{conv}	potential density related to convection
Π_{en}	potential density related to energy balance
Π_z	potential density related to averaging equation
ρ_0	reference density
σ	Cauchy stress tensor
σ_y	yield stress
σ_{y0}	initial yield stress
$\sigma_{y\infty}$	residual yield stress
τ	Kirchhoff stress tensor
φ	motion function
χ	Taylor-Quinney heat dissipation factor
ψ	Helmholtz free energy functional
ω	damage or plastic degradation variable (distinguished by superscript)

Symbols, mathematic accents

$\nabla \cdot$	spatial gradient
$\nabla_0 \cdot$	material gradient
$\text{div}(\cdot)$	spatial divergence
$\Delta \cdot$	increment
$[[\cdot]]$	jump of quantity
\cdot^T	transposition
\hat{a}	prescribed value (for boundary conditions)
\dot{a}	material time derivative

Brackets

Parentheses () are used for function argument whereas square brackets [] for specifying order of operations or vector components.

Vectors in square brackets form one vector with the following components

$$[\mathbf{u}, \mathbf{v}] = [u_1, u_2, \dots, u_n, v_1, v_2, \dots, v_m]$$

where n and m are numbers of coefficients for vectors \mathbf{u} and \mathbf{v} , respectively.

Tensors

- Second order tensor \mathbf{S} is defined as linear mapping of vector to vector

$$\mathbf{u} = \mathbf{S}\mathbf{v}, \quad u_i = S_{ij}v_j$$

- Fourth order tensor \mathbb{C} is defined as linear mapping of second order tensor to second order tensor

$$\mathbf{S} = \mathbb{C}\mathbf{T}, \quad S_{ij} = C_{ijkl}T_{kl}$$

Products

- Inner (scalar) product of two vectors is denoted by

$$\mathbf{u} \cdot \mathbf{v} = u_i v_i$$

- Outer (tensor) product of two vectors is denoted by

$$[\mathbf{u} \otimes \mathbf{v}]_{ij} = u_i v_j$$

- Inner product (double contraction) of two second-order tensors is denoted by

$$\mathbf{S} : \mathbf{T} = S_{ij}T_{ij}$$

- Product (composition) of two second order tensors is denoted by

$$[\mathbf{ST}]_{ij} = S_{ik}T_{kj}$$

- Outer product of two second-order tensors is denoted by

$$[\mathbf{S} \otimes \mathbf{T}]_{ijkl} = S_{ij}T_{kl}$$

Introduction

1.1 Motivation and objective of the research

It can be observed in experiments that materials like metals, alloys or composites can exhibit large (possibly permanent) deformations and very often, after uniform deformation, strains start to localize in certain zone, e.g. shear band. This phenomenon, which can be triggered by material, thermal or geometrical effects, can lead to failure of the material. What is more, the complex material response is often determined by its microstructure. For instance, ductile damage is governed by nucleation, growth and coalescence of microvoids. Although their volume is small in comparison with the total material volume, they have noticeable effects on the global material behaviour. The standard local continuum theories fail to describe localization and are not able to reproduce scale effects originated from the microstructure. Moreover, from the mathematical point of view, in such situation the boundary value problem becomes ill-posed and does not have a unique solution.

It cannot be neglected that changes in temperature field can significantly influence the material response. The phenomena which should be taken into account in a material description are: thermal expansion, heat generation during plastic deformation and dependence of material parameters on temperature, which can lead to thermal softening. What is more, if large strains are admitted, the heat flux should be analyzed in the deformed configuration.

Classically, the main aspects of science were theory and experiment. With the development of computer science the third ingredient appeared – numerical simulations, which perfectly completes the remaining ones. However, models representing the complex response of a material are hardly reproduced by standard descriptions used in a finite element software, and in such situation only user-prepared subroutines can solve the problem.

Thus, having the above problems in mind, the objective of the research is to develop and numerically verify a family of material models accounting for large strains, nonlinear constitutive relations (plasticity, damage) with special attention paid to instabilities occurring in the material. Firstly, the attention is focused on modelling of materials in isothermal conditions, later, full thermomechanical coupling is approached. The models

can be used to reproduce the behaviour of metals and isotropic composites. However, they are not directly focused on a specific material but rather on phenomena leading to localization in the isothermal or non-isothermal conditions. The attention is limited to phenomenological modelling, however a bridge between the micro and macro scale is performed using an internal length scale introduced by gradient averaging, which regularizes the continuum descriptions and prevents ill-posedness of the boundary value problem.

All simulations are performed in *AceGen/FEM* environment using self-prepared finite element subroutines. Due to the novel symbolic-numerical approach to computations the particular solution algorithms taking the advantage of automatic differentiation are developed.

The main assumptions in the work are as follows: continuity and isotropy of the material, elasticity, rate-independent plasticity with associated flow rule. No inertial effects are considered, but non-stationary heat flow is admitted. All models are developed in the three-dimensional space. The developed material models are tested for elongated samples (bar with circular or rectangular cross section and perforated or rectangular plate).

It should be mentioned that a large part of the work was published in scientific journals. Thus, the selection of the tested benchmarks for material models was often made to create a consistent contents for a paper. The isothermal model of gradient-enhanced elasto-plasticity with damage was presented in [Wcisło and Pamin, 2013] and [Wcisło et al., 2013]. The isothermal and non-isothermal models for nonlocal elasto-plasticity with degradation of the yield strength were included in [Pamin et al., 2017]. Local thermo-elasto-plasticity and its enhancement with temperature averaging was published in [Wcisło and Pamin, 2017].

Initially, the project was planned to cover theoretical modelling, benchmark simulations and validation of the developed models by comparison of the obtained results with experiments. However, during the work the attention has shifted mainly to the two first aspects. The models presented in the dissertation, both the isothermal and the thermomechanical, can be used to reproduce the real behaviour of a material including large strain plasticity, ductile damage and/or thermal softening. Experimental validation of the models requires then the specification of proper material parameters and can be done in the future.

1.2 Scope of the work

The dissertation consists of 8 chapters, which are preceded by abstract and notation, and three appendices. The work is closed with a summary written in Polish. This section ends the introductory chapter including motivation and aim of the research as well as the dissertation structure.

In Chapter 2 the basic concepts of large strain description are presented. Chapter 3 deals with the grounds of instability analysis and contains the discussion of three sources of softening which may occur in large strain thermomechanical models - material, thermal and geometrical. Chapter 4 includes the discussion of the computational approach used in the work. In this part of the dissertation the applied symbolic-numerical

tools *AceGen/FEM* are presented with an extensive justification of the choice of software.

Chapter 5 includes the theoretical formulations, description of implementation and the numerical simulation results for large strain isothermal models. In particular, two gradient models are taken into account: gradient-enhanced plasticity with damage influencing the elastic free energy and nonlocal plasticity with degradation of the yield strength. Chosen aspects of these models are investigated in computational tests.

The local large strain thermomechanical model is considered in Chapter 6. The description of the material is included and the finite element algorithm for thermo-plasticity is presented. Numerical experiments are performed to verify the model behaviour, with special attention paid to the influence of heat conduction on localization. In Chapter 7 the gradient-enhanced models for thermomechanical coupling are presented. The first model includes averaging of temperature increase which governs the reduction of the yield strength. The second one is the thermomechanical extension of nonlocal plasticity with degradation of the yield strength. After a short presentation of numerical implementation valid for both models the results of benchmark simulations are shown.

Chapter 8 includes conclusions and prospects of future work. The appendices include simulation of plane strain state for two- and three-dimensional finite *F-bar* elements (Appendix A), aspects of implementation of convective boundary conditions for three-dimensional finite elements (Appendix B), and result for thermo-elasto-plasticity with temperature-dependent Young modulus (Appendix C).

Large strain problem

This Chapter is based on several books dealing with nonlinear continuum mechanics, especially [Bonet and Wood, 2008], [Wriggers, 2008] and [Gurtin et al., 2010]. Only essential information and definitions are presented which are needed for instability analysis or constitutive modelling included in the following Chapters. For detailed descriptions or derivations the reader is referred to the books listed above.

2.1 Grounds of large strain kinematics

Let us consider a deformable continuous body \mathcal{B} with boundary $\partial\mathcal{B}$. The body is treated as a three dimensional object composed of continuously distributed material points also called particles. The body can undergo finite deformations thus the description requires the distinction between initial (referential, undeformed) and current (deformed) configurations of the body and, consequently, two coordinate systems are involved. The referential placement of body \mathcal{B} at time $t = 0$ is specified in material (Lagrangian) coordinates defined with Euclidean basis $\{\mathbf{E}_1, \mathbf{E}_2, \mathbf{E}_3\}$. The initial position of the body particle is denoted with vector \mathbf{X} , which can be treated as a label of the particle that does not depend on time

$$\mathbf{X} = X_1\mathbf{E}_1 + X_2\mathbf{E}_2 + X_3\mathbf{E}_3 \quad (2.1)$$

The current position of body \mathcal{B} is described in a spatial (Euler) coordinate system specified by versors $\{\mathbf{e}_1, \mathbf{e}_2, \mathbf{e}_3\}$. At time t the particle labelled with \mathbf{X} occupies the spatial point denoted with vector \mathbf{x}

$$\mathbf{x} = x_1\mathbf{e}_1 + x_2\mathbf{e}_2 + x_3\mathbf{e}_3 \quad (2.2)$$

It is assumed in the further considerations that the bases of Lagrangian and Eulerian coordinates systems coincide, however, this distinction is introduced here to emphasize the spatial or material nature of quantities. Thus, two distinct descriptions are used in the following considerations according to the rule:

- material description: if a quantity is described with respect to the Lagrangian coordinates \mathbf{X} , i.e. $f(\mathbf{X}, t)$

- spatial description: if a quantity is defined on the basis of the current position of the body particles (Eulerian coordinates) \mathbf{x} , i.e. $f(\mathbf{x}, t)$

The vector field \mathbf{u} defined as follows

$$\mathbf{u}(\mathbf{X}, t) = \mathbf{x}(\mathbf{X}, t) - \mathbf{X} \quad (2.3)$$

represents the displacement field, whereas the motion of the body is described by a mapping of the initial position of a material point into its current location and is denoted with φ

$$\mathbf{x} = \varphi(\mathbf{X}, t) \quad (2.4)$$

The illustrative picture of particle neighbourhood motion is presented in Figure 2.1.

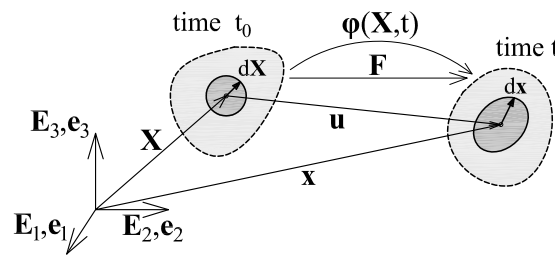


Figure 2.1: Motion of particle neighbourhood

2.2 Measures of deformation

2.2.1 Deformation gradient

Body \mathcal{B} changes its size and shape during deformation. The primary measure which characterizes them is the deformation gradient \mathbf{F} which is a two point tensor (i.e. it involves points in two configurations - referential and current) and expresses the relation between infinitesimal undeformed vector $d\mathbf{X}$ and its counterpart in the current deformed configuration $d\mathbf{x}$

$$d\mathbf{x} = \mathbf{F}d\mathbf{X} \quad (2.5)$$

The deformation gradient and its determinant (Jacobian) are defined as

$$\mathbf{F} = \frac{\partial \mathbf{x}(\mathbf{X}, t)}{\partial \mathbf{X}} \quad J = \det(\mathbf{F}) \neq 0 \quad (2.6)$$

In general, the deformation gradient is non-symmetric. For the rigid body transformation the deformation gradient is equal to the rotation tensor. The determinant of the deformation gradient J expresses the relation between the infinitesimal material volume element dV and its spatial counterpart dv according to formula

$$dv = JdV \quad (2.7)$$

For isochoric (volume-preserving) deformation the Jacobian is equal to $J = 1$.

Accordingly, the deformation gradient can be multiplicatively decomposed into its isochoric and volumetric parts:

$$\mathbf{F} = \mathbf{F}^{iso} \mathbf{F}^{vol}, \quad \mathbf{F}^{iso} = J^{-1/3} \mathbf{F}, \quad \mathbf{F}^{vol} = J^{1/3} \mathbf{I} \quad (2.8)$$

On the basis of the deformation gradient the relation between an elementary area in the reference configuration and its counterpart in the current configuration is also determined

$$d\mathbf{a} = J \mathbf{F}^{-T} d\mathbf{A} = \text{cof}(\mathbf{F}) d\mathbf{A} \quad (2.9)$$

where $d\mathbf{a} = da \mathbf{n}$ and $d\mathbf{A} = dA \mathbf{N}$. Vectors \mathbf{N} and \mathbf{n} are unit normals to area elements dA and da in the reference and current configurations, respectively.

2.2.2 Deformation and strain tensors

There are numerous formulations and names of strain measures in literature. Based on notation and definitions included in [Bonet and Wood, 2008] the following tensors are defined

- right Cauchy-Green deformation tensor:

$$\mathbf{C} = \mathbf{F}^T \mathbf{F}, \quad d\mathbf{x}_1 \cdot d\mathbf{x}_2 = d\mathbf{X}_1 \cdot \mathbf{C} d\mathbf{X}_2 \quad (2.10)$$

- left Cauchy-Green deformation tensor:

$$\mathbf{b} = \mathbf{F} \mathbf{F}^T, \quad d\mathbf{X}_1 \cdot d\mathbf{X}_2 = d\mathbf{x}_1 \cdot \mathbf{b}^{-1} d\mathbf{x}_2 \quad (2.11)$$

- Lagrangian (or Green) strain tensor:

$$\mathbf{E} = \frac{1}{2}(\mathbf{C} - \mathbf{I}), \quad \frac{1}{2}(d\mathbf{x}_1 \cdot d\mathbf{x}_2 - d\mathbf{X}_1 \cdot d\mathbf{X}_2) = d\mathbf{X}_1 \cdot \mathbf{E} d\mathbf{X}_2 \quad (2.12)$$

- Eulerian (or Almansi) strain tensor:

$$\mathbf{e} = \frac{1}{2}(\mathbf{I} - \mathbf{b}^{-1}), \quad \frac{1}{2}(d\mathbf{x}_1 \cdot d\mathbf{x}_2 - d\mathbf{X}_1 \cdot d\mathbf{X}_2) = d\mathbf{x}_1 \cdot \mathbf{E} d\mathbf{x}_2 \quad (2.13)$$

where $d\mathbf{X}_1$ and $d\mathbf{X}_2$ are two differential vectors which deform to $d\mathbf{x}_1$ and $d\mathbf{x}_2$, respectively. Looking at the above definitions it is clear that the first and the third measures are related to the material description whereas the remaining ones are spatial quantities.

2.3 Stress measures

The analyzed body \mathcal{B} can be loaded with mass or surface forces which cause stress state in the body. In the current configuration the basic stress measure is the well-known Cauchy stress tensor, related to the standard definition of stress vector as force per unit area, and denoted with

$$\boldsymbol{\sigma} = \sum_{i,j=1}^3 \sigma_{ij} \mathbf{e}_i \otimes \mathbf{e}_j \quad (2.14)$$

Next, the stress measure called Kirchhoff stress tensor is defined as

$$\boldsymbol{\tau} = J\boldsymbol{\sigma} \quad (2.15)$$

The stress measure referred to the reference configuration is the first Piola-Kirchhoff stress tensor

$$\mathbf{P} = J\boldsymbol{\sigma}\mathbf{F}^{-T} \quad (2.16)$$

which is unsymmetrical. On the other hand, the symmetric material tensor is the second Piola-Kirchhoff tensor which is defined as follows

$$\mathbf{S} = J\mathbf{F}^{-1}\boldsymbol{\sigma}\mathbf{F}^{-T} \quad (2.17)$$

2.4 Time derivatives

The velocity of a particle labelled with \mathbf{X} is defined as the following time derivative

$$\mathbf{v}(\mathbf{X}, t) = \frac{\partial \boldsymbol{\varphi}(\mathbf{X}, t)}{\partial t} \quad (2.18)$$

Although the velocity vector is expressed in terms of Lagrangian coordinates of the particle \mathbf{X} it is a spatial vector. In fact, the velocity can also be expressed as a function of spatial position: $\mathbf{v}(\mathbf{x}, t)$ when an inversion of Equation (2.4) is used.

The material time derivative of a scalar or tensorial quantity $\mathbf{G}(\mathbf{X}, t)$ is denoted with dot over the quantity and is defined as

$$\dot{\mathbf{G}} = \frac{\partial \mathbf{G}(\mathbf{X}, t)}{\partial t} \quad (2.19)$$

whereas the time derivative of spatial quantity $\mathbf{g}(\mathbf{x}, t)$ includes a part involving the velocity of the particle (convective derivative)

$$\dot{\mathbf{g}} = \frac{\partial \mathbf{g}(\mathbf{x}, t)}{\partial t} + (\nabla \mathbf{g})\mathbf{v} \quad (2.20)$$

where $\nabla \cdot$ denotes a gradient with respect to current coordinates (spatial gradient).

The velocity gradient tensor is defined as follows

$$\mathbf{l} = \frac{\partial \mathbf{v}(\mathbf{x}, t)}{\partial \mathbf{x}} = \nabla \mathbf{v} \quad (2.21)$$

and can be alternatively expressed using the deformation gradient and its material time derivative

$$\mathbf{l} = \dot{\mathbf{F}}\mathbf{F}^{-1} \quad (2.22)$$

The rate of deformation tensor \mathbf{d} , which is the spatial counterpart of tensor $\dot{\mathbf{E}}$, can be obtained using formulas

$$\mathbf{d} = \mathbf{F}^{-T}\dot{\mathbf{E}}\mathbf{F}^{-1} = \frac{1}{2}(\mathbf{l} + \mathbf{l}^T) \quad (2.23)$$

2.5 Work conjugacy

The equilibrium equation, which will be considered in the subsequent sections, can be formulated using different measures of stress and strain. However, the pairs cannot be chosen arbitrarily, but only work conjugate quantities can be combined. In particular, following [Bonet and Wood, 2008], the power of the internal forces can be specified using

- spatial quantities: the Cauchy stress tensor and the rate of deformation tensor

$$\int_v \boldsymbol{\sigma} : \mathbf{d} \, dv \quad (2.24)$$

- spatial quantities per unit of undeformed volume: the Kirchhoff stress tensor and the rate of deformation tensor

$$\int_V \boldsymbol{\tau} : \mathbf{d} \, dV \quad (2.25)$$

- material quantities: the first Piola-Kirchhoff stress tensor and the deformation gradient

$$\int_V \mathbf{P} : \dot{\mathbf{F}} \, dV \quad (2.26)$$

- symmetric material quantities: the second Piola-Kirchhoff stress tensor and the Lagrangian strain tensor

$$\int_V \mathbf{S} : \dot{\mathbf{E}} \, dV \quad (2.27)$$

Instabilities

3.1 Introduction

When a material experiences a load which grows to extreme values it initially deforms uniformly and from some point of the process strains increase only in a certain zone while the rest of the sample experiences unloading. This phenomenon, which precedes the failure of the material, is called strain localization and is closely related to the notion of instability. When a specimen exhibits large deformation, the strain increments are concentrated in narrow shear bands (localized mode) or neck (diffuse mode). In general, the loss of stability can have three sources: material degradation (caused by e.g. microcrack growth), temperature-induced softening (e.g. caused by the reduction of the yield strength due to the increase of temperature) and geometrical effects. In the following sections a short discussion on them is included.

The notion of material instability and its theoretical basis go back to [Hill, 1958, Thomas, 1961, Rice, 1976]. Significant contributions to the subject of numerical simulation of instability and strain localization for isothermal conditions were provided among others in [Rudnicki and Rice, 1975, Belytschko and Lasry, 1989, Sluys, 1992, de Borst et al., 1993, Vardoulakis and Sulem, 1995, Tvergaard, 1999, Menzel, 2002, Forest and Lorentz, 2004, Bigoni, 2012, Benallal and Marigo, 2007]. Much less work has been related to the aspects of stability including thermomechanical coupling, e.g. thermo-elasticity is addressed in [Abeyaratne and Knowles, 1999, Dunwoody and Ogden, 2002, Rooney and Bechtel, 2004], thermo-plasticity under the assumption of adiabatic conditions in [Duszek et al., 1992, Steinmann et al., 1999], whereas the analysis including heat conduction in thermo-inelastic materials is performed in [Benallal and Bigoni, 2004]. In fact, the specialists in the field of instabilities usually limited themselves either to isothermal conditions, or to thermo-elasticity, or to adiabatic case, or to small strain regime.

3.2 Material instability

3.2.1 Small strain problem

The notion of material stability goes back to [Hill, 1958] who called a material *stable* if the following requirement is satisfied

$$\dot{\boldsymbol{\epsilon}} : \dot{\boldsymbol{\sigma}} > 0 \quad (3.1)$$

In inequality (3.1) the quantity $\dot{\boldsymbol{\epsilon}}$ denotes a strain rate tensor and $\dot{\boldsymbol{\sigma}}$ is a stress rate tensor. It can be concluded from Equation (3.1) that the material is unstable if for positive strain increments the negative (or zero) stress increments are observed. This situation manifests itself with the descending stress-strain diagram, which is illustratively presented in Figure 3.1(a).

If the constitutive dependencies between the stress and strain rates can be expressed with the incrementally linear relation

$$\dot{\boldsymbol{\sigma}} = \mathbb{D}\dot{\boldsymbol{\epsilon}} \quad (3.2)$$

where \mathbb{D} is a material tangent operator, then the condition (3.1) can be reformulated

$$\dot{\boldsymbol{\epsilon}} : [\mathbb{D}\dot{\boldsymbol{\epsilon}}] > 0 \quad (3.3)$$

From the mathematical point of view, the above inequality is satisfied if the tangent matrix is positive definite.

A necessary condition for the local loss of solution uniqueness [Forest and Lorentz, 2004] is

$$\det(\mathbb{D}^s) = 0 \quad (3.4)$$

where \mathbb{D}^s is a symmetric part of the tangent matrix. In this work the considerations are limited to associative plasticity, thus, material tangent \mathbb{D} is symmetric and the condition of material stability coincides with the condition of uniqueness (also called limit point). The analysis of instabilities for non-associative plasticity theory is included in e.g. [Stankiewicz and Pamin, 2001].

Furthermore, the phenomenon of material instability is related to a so-called discontinuous bifurcation which can occur at a point. Following [Forest and Lorentz, 2004] and the references cited therein the deformation modes involving a jump of the velocity gradient across a discontinuity surface, see Figure 3.1(b), are considered for a static case

$$[[\dot{\boldsymbol{\epsilon}}]] = (\mathbf{g} \otimes \mathbf{n})^s \neq \mathbf{0} \quad (3.5)$$

where symbol $[[\cdot]]$ denotes a jump in a quantity across a discontinuity surface with normal \mathbf{n} , superscript \cdot^s denotes symmetrization and \mathbf{g} is a vector that describes the jump. Assuming that the analysis is limited to weak discontinuities [Jirásek, 2002], see Figure 3.1(c), no jumps of displacement \mathbf{u} (and velocity \mathbf{v}) are admitted.

For static loading, the traction equilibrium equation in the rate form for a material point on discontinuity surface can be written using Cauchy stress tensor

$$[[\dot{\boldsymbol{\sigma}}]]\mathbf{n} = \mathbf{0} \quad (3.6)$$

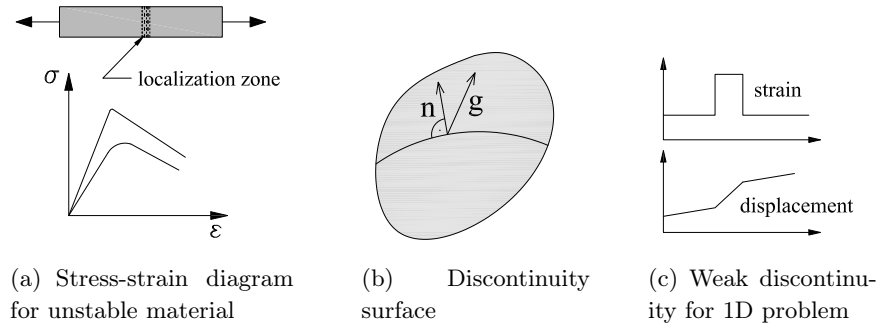


Figure 3.1: Material instability

By inserting the constitutive relation (3.2) and the formula for jump (3.5) into Equation (3.6), the following condition is obtained

$$\mathbb{D}[\mathbf{g} \otimes \mathbf{n}] \mathbf{n} = \mathbf{0} \quad (3.7)$$

The above equation has a non-trivial solution if and only if the determinant of acoustic tensor $\mathbf{Q}(\mathbf{n})$ which is defined as

$$\mathbf{Q}(\mathbf{n})\mathbf{g} = \mathbb{D}[\mathbf{g} \otimes \mathbf{n}]\mathbf{n} \quad (3.8)$$

is zero

$$\det(\mathbf{Q}) = 0 \quad (3.9)$$

The singularity of the acoustic tensor implies the loss of well-posedness of boundary value problem and the initially elliptic governing equations become hyperbolic.

The derivations for the general case involving inertial effects and propagation of the discontinuity surface are discussed in e.g. [Forest and Lorentz, 2004].

It is worthwhile to mention that alternatively to the jump conditions, the stability analysis can be performed using wave propagation approach. More precisely, before the onset of localization the homogeneous state is assumed and the following expansion of the displacement field is adopted

$$\mathbf{u} = \exp(ik[\hat{\mathbf{n}} \cdot \mathbf{x}])\hat{\mathbf{m}} \quad (3.10)$$

which corresponds to the assumption of stationary planar waves. In Equation (3.10) i is an imaginary number so that $i^2 = -1$, k denotes real and positive wave number, $\hat{\mathbf{n}}$ and $\hat{\mathbf{m}}$ are wave propagation direction and the polarization, respectively. Based on this approach and the balance of linear momentum, it is investigated if the homogeneous state admits a bifurcation into a solution of planar wave type [Liebe, 2003].

From the mathematical point of view, when the governing differential equations for the static case loses their ellipticity the boundary-value problem becomes ill-posed and has not a unique solution. Then, strains localize in the possibly smallest volume of the material which for the problem described with classical continuum model is a set of measure zero (the discontinuity surface). This situation manifests itself in the pathological mesh-sensitivity in numerical simulations as the smallest possible volume is determined by the finite element discretization. The example of such behaviour is

presented in Figure 3.2 where the results for an elongated bar simulated with the elasto-damage model are shown. It can be observed that the diagrams strongly depend on the adopted finite element mesh and inelastic deformation localizes in one row of elements when the rest of the bar is unloaded.

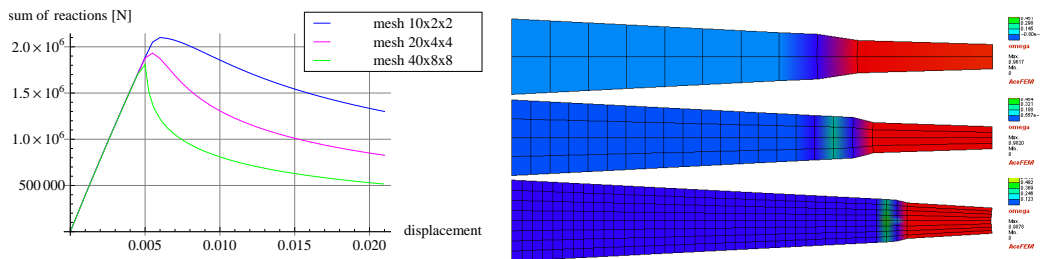


Figure 3.2: Sum of reactions vs enforced displacement (on the left) and deformed meshes with damage variable distribution (on the right) for elongated bar with variable square cross-section (local elasto-damage)

To reproduce numerically material softening two solutions can be used. Firstly, a proper regularization should be applied to continuum theories, which introduces an internal length parameter governing the width of the localization zone, for example nonlocal integral models [Bažant and Pijaudier-Cabot, 1988, Jirásek, 1998, Bobiński, 2006], rate dependent models [Sluys, 1992, Winnicki et al., 2001, Glema, 2004], micropolar continuum [de Borst, 1991, Tejchman and Wu, 1993] or higher order gradient enhancement [de Borst and Mühlhaus, 1992, Peerlings et al., 1996b, Liebe and Steinmann, 2001, Askes et al., 2002, Aifantis, 2014]. Secondly, the continuous-discontinuous modelling can be applied which assumes that the deformation concentrates in interfaces or discrete cracks [Rots, 1988]. In the dissertation the gradient enhancement of continuum description is adopted and introduced in the following sections.

3.2.2 Large strain problem

When geometrical nonlinearities are incorporated, then the equilibrium equation can be formulated in a few ways, depending on the stress measure involved. If the deformed configuration is considered then Equation (3.6) with the Cauchy stress tensor is valid assuming that vector \mathbf{n} is specified in the current configuration. The traction equilibrium can also be formulated in the reference configuration using Lagrangian quantities, e.g. the first Piola-Kirchhoff stress tensor

$$[[\dot{\mathbf{P}}]]\mathbf{N} = \mathbf{0} \quad (3.11)$$

Here, \mathbf{N} is a vector normal to the discontinuity surface in the reference configuration which is related to vector \mathbf{n} through the formula

$$\mathbf{n} = \frac{\mathbf{F}^{-T}\mathbf{N}}{|\mathbf{F}^{-T}\mathbf{N}|} \quad (3.12)$$

For a large strain problem the following jump in the velocity gradient across the discontinuity surface is assumed

$$[[\mathbf{l}]] = \mathbf{g} \otimes \mathbf{n} \neq \mathbf{0} \quad (3.13)$$

Analogously to the small strain problem, the ellipticity condition can be derived using the selected equilibrium equation (in the reference or current configuration), Equation (3.13) and the constitutive relation between deformation and stress measures.

For a problem formulated in the reference configuration, using the symmetric second Piola-Kirchhoff stress \mathbf{S} and the right Cauchy-Green deformation \mathbf{C} tensors with the relation between them $\dot{\mathbf{S}} = \mathbb{D}^{SC} \dot{\mathbf{C}}$, the components of the acoustic tensor have the following form [Khen et al., 1998]

$$Q_{ij} = \frac{1}{2} [N_K S_{KL} N_L] \delta_{ij} + N_L F_{iK} D_{KLMN}^{SC} F_{Mj} N_N \quad (3.14)$$

For the unsymmetric first Piola-Kirchhoff stress tensor \mathbf{P} and the deformation gradient \mathbf{F} , where $\dot{\mathbf{P}} = \mathbb{D}^{PF} \dot{\mathbf{F}}$, the simpler form is obtained [Kowalczyk-Gajewska, 2016]

$$Q_{ij} = D_{iKjL}^{PF} N_K N_L \quad (3.15)$$

Finally, using spatial quantities, the components of the acoustic tensor can be computed as [Khen et al., 1998]

$$Q_{ij} = \frac{1}{2} [n_k \sigma_{kl} n_l] \delta_{ij} + n_k D_{ikjl}^{\sigma d} n_l \quad (3.16)$$

where tangent $\mathbb{D}^{\sigma d}$ is a spatial counterpart of tangent \mathbb{D}^{SC} , for details see [Khen et al., 1998].

3.2.3 Pilot results for ellipticity verification

The investigation of ellipticity conditions for nonlocal or/and thermomechanical models is a subject of the current research carried out under grant funded by the National Science Centre of Poland. In the thesis the pilot results obtained for ideal elasto-plasticity are presented.

The analyzed problem is a rectangular plate in plane strain conditions with an imperfection in the center of the specimen (1% reduction of the initial yield strength) and elongated up to 1.2 of the plate length. Due to symmetry only one quarter is analyzed. The material model adopted for this test is ideal elasto-plasticity with Huber-Mises-Hencky yield criterion.

The force-elongation diagrams are presented on the left in Figure 3.3. In the diagram the response of the analyzed plate with imperfection is shown together with the primary path obtained for the plate simulated with one finite element. It can be observed that the descending diagram resulting from geometrical softening occurs for the plastic regime although ideal plasticity is assumed. The final deformation presented in the right picture of Figure 3.3 includes a shear band of certain width.

After every convergent step of the loading process the ellipticity condition is verified in the imperfect element at the Gauss point nearest to the center of the plate using Equation (3.15). Thus, the analysis is performed in the reference configuration. For this purpose the material tangent \mathbb{D}^{PF} is computed in *AceGen* and saved in a data base for the analysis in the *AceFEM* environment. The acoustic tensor \mathbf{Q} is computed for in-plane vectors $\mathbf{N} = [\cos \alpha, \sin \alpha, 0]$ where the analyzed angles are $\alpha = 0 : \pi/720 : \pi$ ($\alpha = 0 : 0.25 \text{ deg} : 180 \text{ deg}$). For every convergent load step the minimum value of

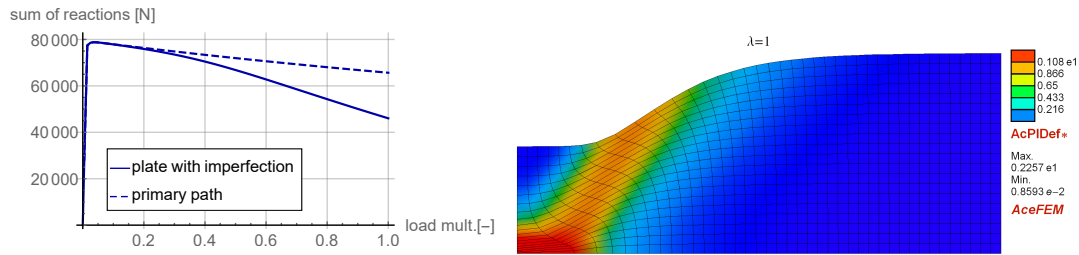


Figure 3.3: Sum of reactions vs enforced load multiplier (on the left) and deformed mesh with plastic strain measure distribution at the end of elongation (on the right)

the determinant of acoustic tensor is investigated, see the left diagram in Figure 3.4. The direction of the first associated normal to discontinuity surface \mathbf{N} for which the determinant of acoustic tensor reaches its minimum is presented in the right diagram of Figure 3.4.

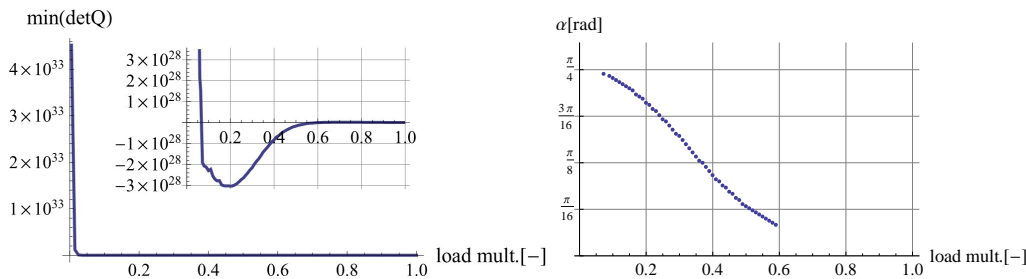


Figure 3.4: Minimum value of the determinant of acoustic tensor vs enforced load multiplier (on the left) and the direction of normal to discontinuity surface vs enforced load multiplier (on the right)

It can be observed that, for the adopted load steps, the determinant of the acoustic tensor reaches a negative value for the first time when the load multiplier is equal to 0.07. The value of $\det \mathbf{Q}$ becomes again positive when the load multiplier reaches about 0.6.

The analysis of the determinant of the acoustic tensor in the reference configuration in step $\lambda = 0.07$ (see upper diagrams in Figure 3.5), using the adopted discretization of angle α , reveals that a negative value of the determinant is reached for angles: $\alpha = 44$ deg and $\alpha = 136$ deg. The first corresponding vector to the discontinuity surface in the current configuration, computed with Equation 3.12, is inclined 45 deg with respect to the longitudinal axis.

Next, the acoustic tensor is investigated for the load multiplier equal to 0.20 and 0.50, see Figures 3.6 and 3.7. Vectors \mathbf{N} for which the determinant of the acoustic tensor becomes negative in step $\lambda = 0.20$ are inclined from 37 to 38 deg and from 142 to 143 deg with respect to longitudinal axis. The normal vectors in the current configuration \mathbf{n} corresponding to the first range are inclined from 45.5 to 46.5 deg. In turn, for $\lambda = 0.050$ the inclinations of vectors \mathbf{N} are from 12 to 12.5 deg and from 167 to 167.75 deg (the corresponding inclinations in the current configuration for the first range is from 45.3 to 46.6 deg). It can be concluded that with the deformation process

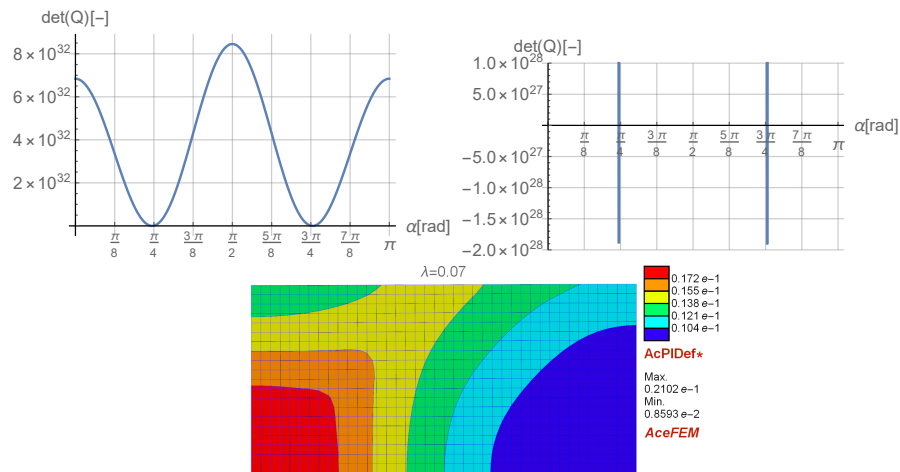


Figure 3.5: Ellipticity analysis for elongated plate in plane strain conditions for enforced displacement multiplier $\lambda=0.07$: determinant of acoustic tensor vs angle α related to direction of vector \mathbf{N} (upper) and deformed mesh with plastic strain measure distribution (lower)

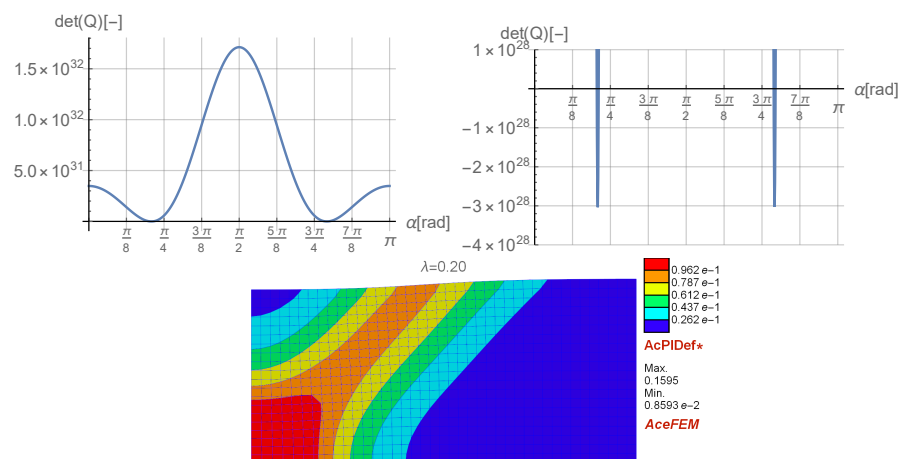


Figure 3.6: Ellipticity analysis for elongated plate in plane strain conditions for enforced displacement multiplier $\lambda=0.20$: determinant of acoustic tensor vs angle α related to direction of vector \mathbf{N} (upper) and deformed mesh with plastic strain measure distribution (lower)

the inclination of vector \mathbf{N} with respect to the longitudinal axis decreases whereas in the current configuration it is still about 45 deg.

3.3 Thermal softening

It is well-recognized that material parameters change with temperature. Usually, the increase of temperature for energetic materials [Holzapfel, 2000] causes decreasing elastic stiffness of the material and a reduction of the plastic strength, cf. Figure 9.10 in book [Cottrell, 1964]. For the yield strength which is a function of internal variables vector

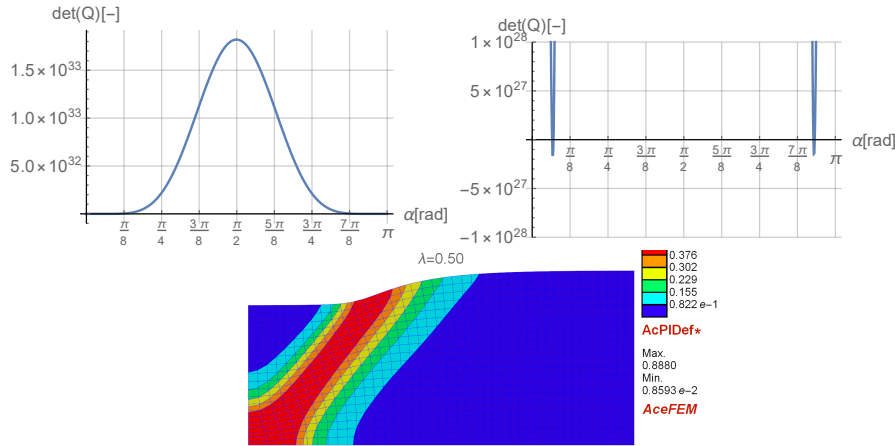


Figure 3.7: Ellipticity analysis for elongated plate in plane strain conditions for enforced displacement multiplier $\lambda=0.50$: determinant of acoustic tensor vs angle α related to direction of vector \mathbf{N} (upper) and deformed mesh with plastic strain measure distribution (lower)

$\boldsymbol{\alpha}$ and temperature the latter can be written as

$$\frac{\partial \sigma_y(\boldsymbol{\alpha}, T)}{\partial T} < 0 \quad (3.17)$$

Many materials, especially metals, generate heat resulting from the dissipation of energy when experience plastic strains. Thus, even in the absence of external sources of heat, temperature of the sample can increase during deformation and cause softening of the material. If localization occurs, then in the band with large plastic strains the heat generation is the strongest, and the yield strength is reduced progressively. It cannot be neglected that in a material subjected to a non-uniform distribution of temperature, heat flows through the material tending to a homogeneous state. Admittedly, heat conduction influences the localization behaviour but its regularizing properties depend on time in contrast to standard gradient-enhanced models. In fact, even if a high value of heat conduction coefficient is assumed for a material, the process can be treated as nearly adiabatic for deformation occurring in a very short time.

From the viewpoint of stability analysis, when the problem is formulated for thermomechanical coupling the additional requirement for the jumps of the heat flux to be zero across the discontinuity surface is formulated

$$[[\mathbf{q}]] \cdot \mathbf{n} = 0, \quad [[\dot{\mathbf{q}}]] \cdot \mathbf{n} = 0 \quad (3.18)$$

with spatial continuity of the temperature field

$$[[T]] = 0 \quad (3.19)$$

Assuming a stationary discontinuity surface, the jump of temperature rate can be non-zero, see [Benallal and Bigoni, 2004]

$$[[\dot{T}]] \neq 0 \quad (3.20)$$

Further, the thermomechanical analysis of instabilities leads to two equations resulting from Equation (3.6) and balance of energy which involves the jump of rate of temperature and jump of divergence of heat flux. For a detailed discussion on stability conditions for thermo-inelastic materials the reader is referred to [Benallal and Bigoni, 2004].

Accordingly, the problem of stability can also be solved using wave propagation analysis. Then the perturbation of the temperature field

$$T = \exp(ik[\hat{\mathbf{n}} \cdot \mathbf{x}])\hat{m} \quad (3.21)$$

is superposed on a homogeneously deformed body at uniform temperature. Variable \hat{m} in Equation (3.21) denotes polarization. The derivation of specific conditions for large strain thermo-elasticity using this approach is included in [Abeyaratne and Knowles, 1999].

3.4 Geometrical effects

When a material undergoes large plastic deformations during tension process, strain localization can occur even if no softening is observed in the stress-strain relationship at a material point. In such case localization is caused by geometrical effects and this structural instability is related to the decreasing area of a cross-section while stresses are limited by a yield function, cf. [Okazawa, 2009].

To demonstrate the problem a simple one dimensional example is now presented, see Figure 3.8. Let us assume a bar with a cross-section area A_0 made of elasto-ideally plastic material. The bar is elongated with an enforced displacement u and the change in its geometry is taken into account. The normal stress can be computed using formula $\sigma = P/A$, where P is the reaction caused by enforced displacement u and A is the current cross-section area. For ideal plasticity the value of stress σ is constrained and cannot exceed the yield strength σ_y . Thus, assuming that the bar cross-section area A decreases during elongation the value of P has to decrease in order to satisfy the equality

$$\sigma = \frac{P}{A} = \sigma_y \quad (3.22)$$

The phenomenon of geometrical softening can be observed not only for ideal plasticity but also for models including hardening in the yield function, cf. [Okazawa, 2009].

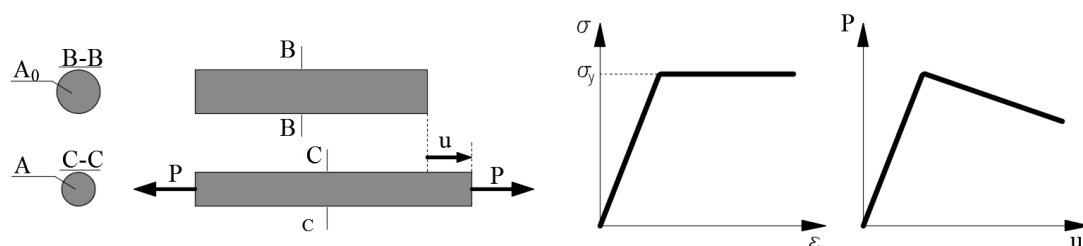


Figure 3.8: Elongation of ideal elasto-plastic bar

Depending on a tested configuration and adopted test parameters, geometrical softening can cause diffuse or localized mode of deformation. Figures 3.9, 3.10 and

3.11 present the results obtained for an elongated bar with a square cross-section modelled with ideal elasto-plasticity¹. The bar is simulated as an ideal or imperfect sample. In the latter case the imperfection is located in the center of the sample and is introduced as a reduction of the yield strength to $\sigma_{y,imp} = 0.97\sigma_y$. In both cases, the process in the plastic regime is unstable and the force-displacement diagrams are descending, see Figure 3.9. When the ideal bar is elongated it initially deforms uniformly and the results are then mesh-insensitive, however, at some point of deformation numerical inaccuracies cause strain localization which, in this example, has a form of multiple necking (different for each mesh), see Figure 3.10. On the other hand, if the imperfection is assumed, strains localize in the center of the analyzed bar in two rows of elements and the results are strongly mesh-dependent, cf. Figure 3.11.

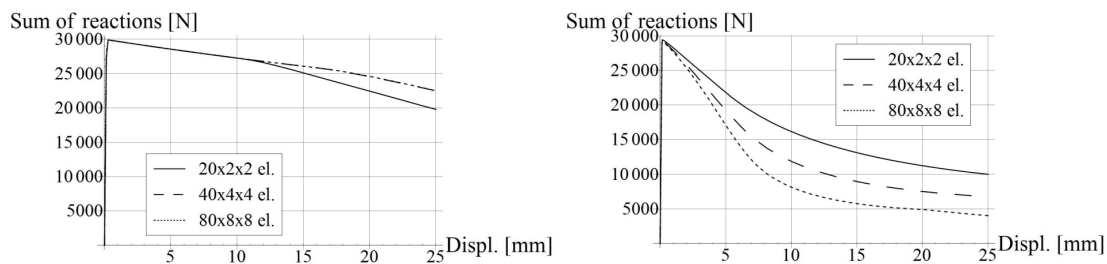


Figure 3.9: Sum of reactions vs displacement for the ideal bar (on the left) and for the bar with imperfection (on the right) - ideal elasto-plasticity

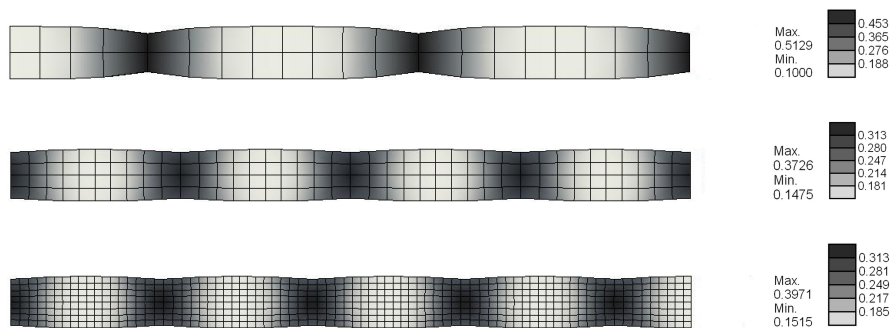


Figure 3.10: Final accumulated plastic strain for three meshes and ideal bar (elastic-ideal-plastic model)

To sum up, even if no material or thermal softening is incorporated into the model the response of the analyzed elongated sample can be unstable and the results can be mesh-sensitive.

¹The results were published in paper [Wcisło and Pamin, 2013]

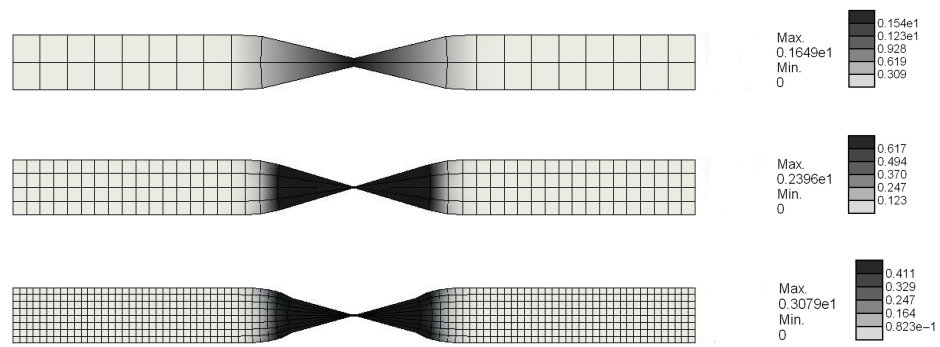


Figure 3.11: Final accumulated plastic strain for imperfect bar and three discretizations (elastic-ideal-plastic model)

Computational approach

4.1 Preliminaries

The material models which are considered in the dissertation include nonlinear geometrical equations (large strains), nonlinear mechanical constitutive relations (plasticity, damage), gradient averaging and full thermomechanical coupling. To verify the model descriptions benchmark numerical simulations should be performed as the analytical solution of such highly nonlinear problem is practically underivable. Therefore, the (initial) boundary value problem is solved using finite element method, see e.g. [Zienkiewicz and Taylor, 1989], which is commonly applied for the majority of solid mechanics problems. Due to the complexity of the analyzed models self-prepared user supplied subroutines are developed for a finite element environment. The set of nonlinear equations resulting from the adopted method is solved on the global level using the standard Newton-Raphson procedure, which requires the linearization of the governing equations for each iteration at every load step.

To obtain a solution for the given final load applied to a sample in simulation, the process is discretized to follow an entire load-displacement path. At every load step the set of nonlinear equations has to be solved to find the state of equilibrium. In general the set of equations can be written in the following form

$$\mathbf{R}(\mathbf{x}) = \mathbf{0} \quad (4.1)$$

where \mathbf{R} is a residual vector and \mathbf{x} is a vector of unknowns. The solution of Equation (4.1) is obtained through an iterative procedure. Using a given solution \mathbf{x}_i in iteration i a new value is computed for the next iteration $i + 1$

$$\mathbf{x}_{i+1} = \mathbf{x}_i + \Delta\mathbf{x}_i \quad (4.2)$$

where increment $\Delta\mathbf{x}_i$ is a solution of the following set of equations

$$\mathbf{K}(\mathbf{x}_i)\Delta\mathbf{x}_i = -\mathbf{R}(\mathbf{x}_i), \quad \mathbf{K}(\mathbf{x}_i) = \left. \frac{\partial\mathbf{R}(\mathbf{x})}{\partial\mathbf{x}} \right|_{\mathbf{x}_i} \quad (4.3)$$

Matrix \mathbf{K} which appears in Equation (4.3) is called consistent tangent matrix. Although the calculation of the tangent matrix can be computationally expensive, the quadratic

convergence for the procedure is guaranteed. For the detailed description of the Newton–Raphson procedure the reader is referred to e.g. [Bonet and Wood, 2008].

4.2 Symbolic–numerical tools

The implementation of all models developed in the dissertation is performed using *Wolfram Mathematica*-based packages *AceGen* and *AceFEM* developed by [Korelc, 2011]. The former is a code generator which creates formulae for a chosen programming language (e.g. FORTRAN, C, Wolfram language) from a symbolic input prepared in a special meta-language based on *Mathematica* notation. The latter is a finite element engine used for numerical simulations.

The *AceGen* tool combines the symbolic and algebraic powerful capabilities of *Wolfram Mathematica* with run-time efficient numerical procedures resulting from programming languages like *C* or *FORTRAN*. It includes a few key techniques, see [Korelc, 2011], the most important of which, from the author point of view, are simultaneous optimization of expressions and automatic differentiation (AD).

The former technique results in the avoidance of expression swell and an efficient final code. Concisely, the programme simplifies and optimizes symbolic formulae through creating auxiliary variables simultaneously with the derivation of the problem, cf. Figure 4.1.

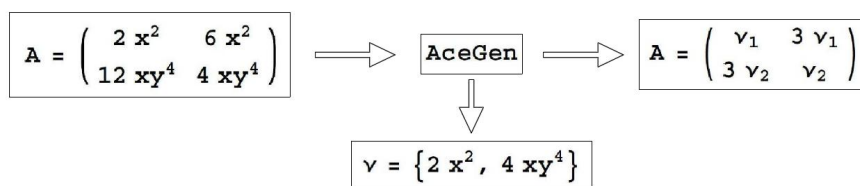


Figure 4.1: *AceGen* optimization of expressions

The latter technique allows for differentiation through employing an *AceGen* function `SMSD[f,x]` which computes the derivative of function f with respect to variable x using forward or backward mode of automatic differentiation. This feature is particularly important for the derivation of the consistent tangent matrix which can be computed automatically. Therefore, due to the application of AD the linearization of the constitutive equations is not considered in this dissertation.

It is worth mentioning that the AD technique in *AceGen* package allows for introduction of additional information to the process of differentiation through so-called *AD exceptions*. For example, let us assume for a given function of two variables $f(\mathbf{a}, \mathbf{b})$ that there is an implicit dependence between variables \mathbf{a} and \mathbf{b} , however, it does not follow from the algorithm itself. To include the relationship between \mathbf{a} and \mathbf{b} in the AD procedure the total derivatives of \mathbf{b} with respect to \mathbf{a} are set to be equal to matrix \mathbf{M} which is introduced in the AD process. This can be schematically written as

$$\nabla_{\mathbf{a}} f = \frac{\partial f(\mathbf{a}, \mathbf{b})}{\partial \mathbf{a}} \bigg|_{\frac{D\mathbf{b}}{D\mathbf{a}} = \mathbf{M}} \quad (4.4)$$

which is compatible with the following *AceGen* input

$$\nabla f = \text{SMSD}[f[a, b], a, \text{"Dependency"} \rightarrow \{b, a, M\}]$$

AD exceptions are especially useful when, for example,

- isoparametric mapping from an element in reference configuration to a 'parent' element has to be introduced in AD
- some implicit dependencies should be omitted in AD
- to ignore the sub-iteration loop in AD and introduce implicit relations instead

The profound explanation of AD procedure and different types of AD exceptions with examples are included in the report by [Korelc, 2011].

The second aforementioned package, *AceFEM*, is a finite element engine which can be replaced by another programme, e.g. *ABAQUS* or *FEAP*, but it is chosen for the numerical simulations due to its convenience and close cooperation with *AceGen*. The *AceFEM* session includes the definition of the analyzed domain, applied boundary conditions, discretization and material parameters. The solution of an initial boundary value problem is performed using Newton-Raphson procedure for which calculations are performed using solver Pardiso. The important advantage of *AceFEM* package is full user control of the computation process. The special debugging palette allows for investigation of all variables at each state of simulation. Finally, the postprocessing session can also be performed in *AceFEM* which includes all tools needed to results treatment as diagrams, graphics and animations.

From the computational point of view the numerical simulation should be performed in a most efficient way as it is possible. However, it should be stressed that the robustness covers not only the quality of the prepared source-code and performance of the finite element engine (i.e. solver) but also includes the time spent on the development of the code.

For a better substantiation of the choice of the presented numerical tools it should be emphasized that for the complex problem considered in the thesis the preparation of a user supplied subroutine for the finite element method using standard programming languages is very difficult and time-consuming. Moreover, further development of the material model would then require repeated analytical linearization of the constitutive equations. On the other hand, when the *AceGen* tool is used, the researcher has to prepare a code in a specific meta-language and the subroutine for a chosen finite element engine is produced automatically. Therefore, although the numerical robustness of the explicitly written code could be probably higher than for the automatically generated subroutine (this was not verified by the author), the application of the symbolic-numerical tools significantly simplifies the process of the user supplied subroutine preparation and facilitates its development in the future. To sum up, using the presented tools the researchers can focus their attention on the material description development instead of the finite element programming.

4.3 General procedure for user finite element subroutine

The application of the symbolic-numerical software requires a specific approach for the FE user supplied subroutines. The development of the appropriate algorithms based

on potentials is recommended by the author of *Ace* packages, see e.g. [Korelc, 2008]. The main advantage of this approach is the numerical efficiency of the solution when automatic differentiation is used in the code. In fact, a standard approach to the finite element method starting from the weak form of the balance equations could also be applied, however, the generated code would not be optimal.

Thus, the general approach to the solution of a problem using *AceGen* package is as follows. Firstly, the unknown field interpolation for a selected finite element has to be introduced

$$\mathbf{d}_{el} = \mathbf{N}_I \cdot \mathbf{p} \quad (4.5)$$

where \mathbf{p} is a vector of nodal unknowns (degrees of freedom) and \mathbf{N}_I is a vector of interpolation (shape) functions. Secondly, the potential Π for the problem should be defined. Upon the introduction of Equation (4.5) into the functional definition, Π becomes a function of the degrees of freedom \mathbf{p} . Then, for properly formulated dependencies the residual vector for the finite element is derived directly as a gradient of free energy functional Π with respect to element degrees of freedom \mathbf{p} integrated over the finite element domain

$$\mathbf{R}_{el} = \int_{V_{el}} \frac{\partial \Pi}{\partial \mathbf{p}} dV \quad (4.6)$$

In this work the Gauss integration is used for all analyzed models, thus, the element residual vector can be defined as follows

$$\mathbf{R}_{el} = \sum_{nG} w_G J_{XG} \mathbf{R}_G, \quad \mathbf{R}_G = \frac{\partial \Pi}{\partial \mathbf{p}} \quad (4.7)$$

where nG is the number of Gauss points, w_G is the weight of a Gauss point, J_{XG} denotes the Jacobian of isoparametric mapping from the parent element to the element in the reference configuration and, finally, \mathbf{R}_G refers to a Gauss point contribution to the element residual vector.

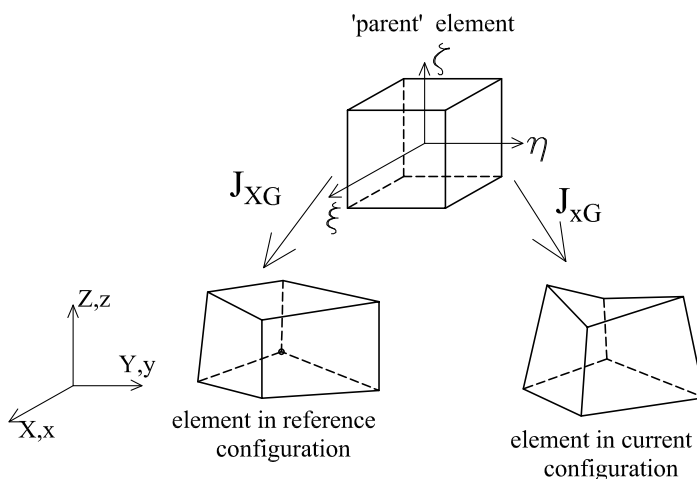


Figure 4.2: 'Parent' finite element vs element in reference and current configuration

In the finite element subroutines the initial coordinates are interpolated and due to that fact it is computationally more efficient to introduce Gauss quadrature in the

reference configuration (using Jacobian J_{X_G}) than using the current configuration (with Jacobian J_{x_G}), cf. Figure 4.2. For instance, for three dimensional hexahedral finite elements eight-point integration scheme is applied.

Accordingly, basing on the aforementioned definitions, the Gauss point contribution to the tangent matrix can be derived using formula

$$\mathbf{K}_G = \frac{\partial \mathbf{R}_G}{\partial \mathbf{p}} \quad (4.8)$$

and, consequently, the element tangent operator is equal to

$$\mathbf{K}_{el} = \frac{\partial \mathbf{R}_{el}}{\partial \mathbf{p}} = \sum_{n_G} w_G J_{X_G} \mathbf{K}_G \quad (4.9)$$

The global residual vector for the problem and the corresponding tangent operator are formed by the finite element assembly procedure which is a built-in tool of *AceFEM*.

Isothermal inelastic models

5.1 Kinematics and constitutive description of local models

5.1.1 Multiplicative split of deformation gradient for elasto-plasticity

In elasto-plastic analysis it is needed to distinguish between elastic (recoverable) and plastic (non-recoverable) deformation. Therefore, specific measures which represent this information should be introduced. This split can be formulated in different ways, see e.g. chapter 8.1 in [Maugin, 1992]. The approach which is used in this work is the well-known multiplicative decomposition of the deformation gradient into elastic \mathbf{F}^e and plastic \mathbf{F}^p parts:

$$\mathbf{F} = \mathbf{F}^e \mathbf{F}^p \quad (5.1)$$

with corresponding determinants

$$J^e = \det(\mathbf{F}^e), \quad J^p = \det(\mathbf{F}^p) \quad (5.2)$$

Decomposition (5.1) was introduced for finite elasto-plasticity by [Lee and Liu, 1967], [Lee, 1969], [Mandel, 1974], [Kroner and Teodosiu, 1974] and from that time has been commonly used by researchers. The split of the deformation gradient is developed using the idea of *intermediate local configuration* resulting from elastic unloading. The configuration is stress-free and includes non-recoverable deformation only, see Fig. 5.1. This approach has not only a phenomenological justification but a micromechanical one as well: the plastic deformation gradient \mathbf{F}^e represents deformation caused by distortion and rotation of the crystal lattice, whereas \mathbf{F}^p is related to the material flow through the crystal lattice by crystallographic slip [Taylor, 1938, Hill and Rice, 1972, Kroner and Teodosiu, 1974, Asaro and Rice, 1977].

5.1.2 Finite elasto-plasticity

In this work the kinematical framework for finite elasto-plasticity is based on multiplicative decomposition (5.1) and the main internal variable is assumed to be the elastic left Cauchy-Green tensor

$$\mathbf{b}^e = \mathbf{F}^e [\mathbf{F}^e]^T, \quad J^{be} = \det(\mathbf{b}^e) \quad (5.3)$$

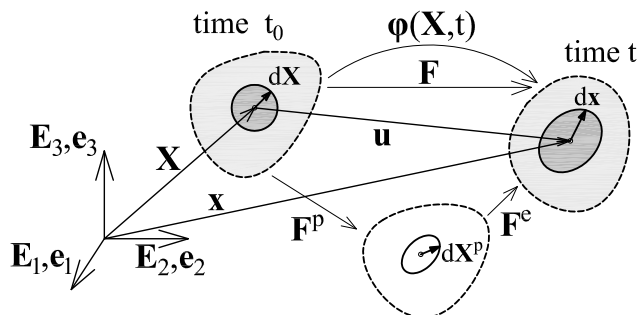


Figure 5.1: Multiplicative split of deformation gradient for elasto-plasticity

The state of a material is expressed by the Helmholtz free energy potential which is assumed as an isotropic function decomposed into elastic and plastic parts

$$\psi = \psi^e(\mathbf{b}^e) + \psi^p(\gamma) \quad (5.4)$$

where γ is for simplicity a scalar measure of plastic strain. This decoupled form of the Helmholtz functional is usually assumed in metal plasticity and is justified from the micromechanical point of view, see [Simo and Miehe, 1992] and the references therein.

In the following considerations the hyperelastic model with the uncoupled volumetric and deviatoric response is used [Simo, 1998a]

$$\psi^e(\mathbf{b}^e) = \frac{1}{2}G \left[\text{tr}([J^{be}]^{-1/3}\mathbf{b}^e) - 3 \right] + \frac{1}{2}K \left[\frac{1}{2}[J^{be} - 1] + \frac{1}{2}\log(J^{be}) \right] \quad (5.5)$$

where G and K are respectively the shear and bulk moduli.

The plastic potential for standard elasto-plasticity with strain hardening (without damage or degradation) has the form

$$\psi^p(\gamma) = \frac{1}{2}H_i\gamma^2 + [\sigma_{y\infty} - \sigma_{y0}]\left[\gamma + \frac{1}{\delta}e^{-\delta\gamma}\right] \quad (5.6)$$

where H_i is a linear hardening coefficient, σ_{y0} – an initial yield stress, $\sigma_{y\infty}$ – a residual yield stress, and δ denotes a saturation parameter.

On the basis of the second law of thermodynamics, which provides restrictions for the constitutive relations, and the adopted form of free energy (5.4) the following state functions are obtained (i.e. the Kirchhoff stress tensor and the hardening function):

$$\boldsymbol{\tau} = 2\frac{\partial\psi}{\partial\mathbf{b}^e}\mathbf{b}^e, \quad h = -\frac{\partial\psi}{\partial\gamma} \quad (5.7)$$

The Kirchhoff stress tensor can be decomposed into its deviatoric and volumetric parts:

$$\boldsymbol{\tau} = p\mathbf{I} + \mathbf{t}, \quad p = [\boldsymbol{\tau} : \mathbf{I}]/3, \quad \mathbf{t} = \boldsymbol{\tau} - p\mathbf{I} \quad (5.8)$$

The plastic regime is defined using a yield function F^p which is an isotropic function of the Kirchhoff stress tensor $\boldsymbol{\tau}$ and the measure of plastic strain γ

$$F^p(\boldsymbol{\tau}, \gamma) = f(\boldsymbol{\tau}) - \sqrt{\frac{2}{3}}[\sigma_{y0} + h(\gamma)] \leq 0 \quad (5.9)$$

The function $f(\boldsymbol{\tau})$ represents a selected stress measure which governs the plastic behaviour. In this work the Huber-Mises-Hencky (HMH) criterion is mostly adopted, however, the pressure-sensitive function of Burzyński-Drucker-Prager (BDP) is also implemented. The latter stress measure function can be written in the form

$$f = \sqrt{2J_2} + \frac{\alpha^p}{3}I_1 \quad (5.10)$$

where α^p is a material constant, I_1 and J_2 are invariants of the Kirchhoff stress tensor $\boldsymbol{\tau}$ and its deviatoric part \mathbf{t} , respectively:

$$I_1 = \boldsymbol{\tau} : \mathbf{I}, \quad J_2 = \frac{1}{2}\mathbf{t}^2 : \mathbf{I} \quad (5.11)$$

If the zero value of α_p is assumed then the HMH yield criterion is obtained.

Following [Simo, 1992] the associative flow rule is assumed in the form

$$-\frac{1}{2}\mathcal{L}_v\mathbf{b}^e = \dot{\lambda}\mathbf{N}^p\mathbf{b}^e \quad (5.12)$$

where \mathcal{L}_v is the Lie derivative of \mathbf{b}^e and \mathbf{N}^p is a normal to the yield function:

$$\mathcal{L}_v\mathbf{b}^e = \mathbf{F}\frac{\partial}{\partial t}[[\mathbf{C}^p]^{-1}]\mathbf{F}^T, \quad \mathbf{N}^p = \frac{\partial F^p}{\partial \boldsymbol{\tau}} \quad (5.13)$$

and $\dot{\lambda}$ is a plastic multiplier satisfying the standard Kuhn-Tucker conditions:

$$\dot{\lambda} \geq 0, \quad F^p \leq 0, \quad \dot{\lambda}F^p = 0 \quad (5.14)$$

For simplicity the considerations are limited to the plastic flow theories in which $\lambda = \gamma$.

5.1.3 Finite elasto-plasticity with damage

The constitutive description analyzed in this section includes damage which is understood here as degradation of the elastic free energy function with a scalar damage variable ω

$$\psi^{e,d} = [1 - \omega^d]\psi^e \quad (5.15)$$

The scalar damage parameter ω^d grows from zero for the intact material to one for a complete material destruction. The damage evolution law which determines the value of ω^d is a function of a history parameter κ^d

$$\omega^d = f^d(\kappa^d) \quad (5.16)$$

and can be formulated in different ways depending on the considered material, see e.g. [Geers, 2004]. In this work the evolution equation introduced in [Mazars and Pijaudier-Cabot, 1989] is used

$$\omega^d(\kappa^d) = 1 - [\kappa_0^d/\kappa^d][1 - \alpha^d + \alpha^d \exp(-\beta^d[\kappa^d - \kappa_0^d])] \quad (5.17)$$

The parameter κ^d in Equation (5.16) is obtained through the formula

$$\kappa^d = \max(\tilde{\varepsilon}, \kappa_0^d) \quad (5.18)$$

where κ_0^d describes the damage threshold and $\tilde{\varepsilon}$ is an equivalent local strain or energy measure. Parameters α^d and β^d are material constants.

The choice of the damage governing quantity $\tilde{\varepsilon}$ which should be applied in the model including large strains will be discussed now. In the literature different measures can be encountered, for instance stored energy [Steinmann, 1999] or accumulated plastic strain [Areias et al., 2003, Žebro et al., 2008]. Here we assume that the damage process is not directly determined by the plastic flow but that it is governed by a total deformation measure. In particular, two measures are taken into account:

$$\tilde{\varepsilon} = \det(\mathbf{F}) - 1 \quad (5.19)$$

$$\tilde{\varepsilon} = \sqrt{[e_1^+]^2 + [e_2^+]^2 + [e_3^+]^2} \quad (5.20)$$

where e_i^+ is a positive i -th eigenvalue of the Almansi strain tensor. The first measure (5.19) is closely connected with the increase of the material volume and can be related to the growth of the voids and cracks in the damage process. According to this model damage will not occur for incompressible materials or for deformation involving volume reduction.

The second measure (5.20) is related to principal stretches by taking into account the positive eigenvalues of Almansi strain tensor. Consequently, in the second case incompressible materials can exhibit damage since also in a compression test the local measure can grow, however in a different way than for tension. For an extended sample damage is governed by a longitudinal strain whereas for compression by a transverse one. Thus, the choice of the proper deformation measure should be connected with the physical behaviour of material, observed in experiments.

The damage loading condition complemented with the other Kuhn-Tucker conditions reads:

$$F^d(\tilde{\varepsilon}, \kappa^d) = \tilde{\varepsilon} - \kappa^d \leq 0, \quad \dot{\kappa}^d \geq 0, \quad \dot{\kappa}^d F^d(\tilde{\varepsilon}, \kappa^d) = 0 \quad (5.21)$$

Due to the incorporation of damage in the constitutive model the plastic process is now assumed to take place in the effective stress space, i.e. it governs the behaviour of the undamaged skeleton of the material. This approach is based on a principle of strain equivalence [Lemaitre, 1984] which states that the damaged material responds to a given stress $\boldsymbol{\tau}$ in the same way as the undamaged material responds to the effective stress $\hat{\boldsymbol{\tau}}$

$$\hat{\boldsymbol{\tau}} = \frac{\boldsymbol{\tau}}{1 - \omega^d} \quad (5.22)$$

Accordingly, the yield function (5.9), normal to the yield surface (5.13) and Kuhn-Tucker conditions are formulated with respect to effective Kirchhoff stress $\hat{\boldsymbol{\tau}}$ instead of $\boldsymbol{\tau}$.

5.1.4 Finite elasto-plasticity with degradation

In this section elasto-plasticity model based on the work of [Geers, 2004] is shortly presented. This model includes large strain elasto-plasticity and can reproduce softening and failure of the material due to an isotropic plastic-damage variable. The yield

condition which governs the plastic regime is defined as

$$F^p(\boldsymbol{\tau}, \gamma, \kappa^p) = f(\boldsymbol{\tau}) - \sqrt{2/3}\sigma_y(\gamma)[1 - \omega^p(\kappa^p)] \leq 0 \quad (5.23)$$

where $f(\boldsymbol{\tau})$ is a stress measure and $\sigma_y(\gamma)$ denotes the evolving yield stress. The analyzed model includes isotropic degradation of the plastic properties of the material, thus the yield stress is multiplied by factor $[1 - \omega^p(\kappa^p)]$ depending on the plastic-damage variable ω^p which varies between 0 for the intact material to 1 for the completely damaged material. The evolution of the value of ω^p is assumed in the dissertation in the following form

$$\omega^p(\kappa^p) = 1 - \exp(-\beta\kappa^p) \quad (5.24)$$

where β is a ductility parameter and κ^p is a history variable.

In the numerical simulations the value of κ^p is assumed to be related to the plastic strain measure, cf. [Geers, 2004],

$$\kappa^p = \sqrt{2/3}\gamma \quad (5.25)$$

It can be noticed that under the assumption (5.25) damage in this model is assumed to begin simultaneously with the plastic process (no damage threshold is considered).

5.2 Gradient enhancement

The incorporation of damage or degradation in the material description results in the softening stress-strain diagram which can cause the loss of ellipticity and ill-posedness of the boundary value problem as it is discussed in Section 3.2. The regularization strategy applied in the work is an implicit gradient enhancement which was first introduced by [Peerlings et al., 1996a] for small strain problem. The approach is motivated by micro-defect interactions and, from numerical point of view, is convenient for implementation. The nonlocality is introduced into the description of a material by incorporation of averaged (nonlocal) quantities. For the small strain case, the implicit gradient averaging expresses the relation between the local and the nonlocal variable in the following form

$$z - l^2 \nabla^2 z = z_{loc} \quad (5.26)$$

where z is the nonlocal variable, z_{loc} the local one and ∇ denotes the gradient operator. The parameter l appearing in Equation (5.26) is a material-dependent length parameter commonly called the internal length scale. In practice, the internal length scale influences the width of a localization zone e.g. shear band. The partial differential equation (5.26), which is solved at the global level, is completed with homogeneous natural boundary conditions, which are discussed in [Peerlings et al., 2001].

The term *implicit* results from the form of Equation (5.26), in which the nonlocal variable cannot be computed directly but it is required to solve the differential equation. The profound discussion on implicit and explicit gradient models is included in e.g. [Peerlings et al., 2001].

For models presented in Section 5.1.3 and 5.1.4 the averaging is performed for variables which govern damage or degradation. Particularly,

- for elasto-plasticity coupled with damage, presented in Section 5.1.3 the local strain measure $\bar{\varepsilon}$ is substituted in Equation (5.18) and in damage condition (5.21a) with its nonlocal counterpart $\bar{\bar{\varepsilon}}$,
- for elasto-plasticity coupled with degradation of the yield strength, described in Section 5.1.4, the local history parameter κ^p is replaced in Equation (5.24) with its nonlocal counterpart $\bar{\kappa}^p$.

The application of gradient enhancement to a material model including large strains requires a decision which configuration is selected for averaging. If material averaging is applied then the derivatives of the nonlocal variable are calculated with respect to Lagrangian coordinates and the internal length l_{mat} is defined in the undeformed configuration. Consequently, during the whole deformation process, the quantities for averaging are taken from the same material domain. In this case the differential equation for material averaging has the following form

$$z - l_{mat}^2 \nabla_0^2 z = z_{loc} \quad (5.27)$$

where ∇_0 denotes gradient with respect to the material coordinates.

On the other hand, if spatial averaging is considered then the internal length scale l_{spat} and the gradients in Equation (5.26) are referred to the deformed configuration (here symbol ∇ denotes gradient computed with respect to the spatial coordinates)

$$z - l_{spat}^2 \nabla^2 z = z_{loc} \quad (5.28)$$

In this case, during a deformation process the region for averaging is constant in the physical space.

The relation between the parameters can be derived from the assumption that $\Pi_{z,mat} = \Pi_{z,spat}$ which leads to the formula

$$l_{spat} = l_{mat} \sqrt{\frac{\nabla_0 z \cdot \nabla_0 z}{\nabla z \cdot \nabla z}} \quad (5.29)$$

The illustrative comparison of the material and spatial averaging is presented in Figure 5.2.

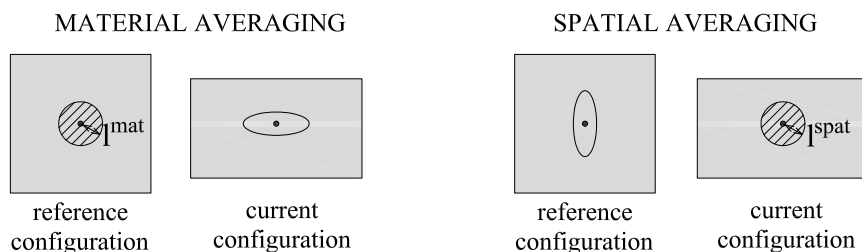


Figure 5.2: Material vs spatial averaging – domain for averaging

In the following numerical simulations the regularization properties of the two presented ways of averaging are investigated.

5.3 Governing equations

Due to the distinction between the reference and the current configuration in large strain analysis the governing equations can be formulated in material, see e.g. [Simo, 1998b], or spatial description, e.g. [Simo and Miehe, 1992]. In the presented model the spatial quantities are used, however, they are referred to the volume/surface in the reference configuration, see e.g. [Miehe, 1995]. Due to the adopted approach the material parameters used in the model are defined per unit of undeformed volume/surface and the integration appearing in weak forms is performed over referential volume, which is computationally less expensive, cf. Section 4.3.

The analyzed coupled problem is described with two governing equations. The first one is the balance of linear momentum formulated in the local form as follows

$$\rho_0 \frac{\partial^2 \boldsymbol{\varphi}}{\partial t^2} = J \operatorname{div}(\boldsymbol{\tau}/J) + \rho_0 \mathbf{B} \quad (5.30)$$

In Equation (5.30) $\operatorname{div}(\cdot)$ is the divergence computed with respect to Eulerian coordinates, ρ_0 is a reference density and \mathbf{B} is a given acceleration field. For the static analysis which is presented in the paper the left-hand side of Equation (5.30) is equal to zero.

The balance of linear momentum is completed with boundary conditions for displacements \mathbf{u} and tractions \mathbf{t}

$$\begin{aligned} \mathbf{u} &= \hat{\mathbf{u}} & \text{on} & \partial\mathcal{B}_u \\ \mathbf{t} &= \boldsymbol{\tau} \cdot \mathbf{n} = \hat{\mathbf{t}} & \text{on} & \varphi(\partial\mathcal{B}_\tau) \end{aligned} \quad (5.31)$$

where

$$\partial\mathcal{B}_u \cup \partial\mathcal{B}_\tau = \partial\mathcal{B} \quad \text{and} \quad \partial\mathcal{B}_u \cap \partial\mathcal{B}_\tau = \emptyset \quad (5.32)$$

Note that the essential boundary condition is defined in the reference configuration whereas the natural one in the current, cf. [Miehe, 1995].

The finite element implementation is based on weak forms of the governing equations. Applying the standard derivation: multiplication by test function $\delta \mathbf{u}$, integration over body \mathcal{B} , applying divergence theorem and Neumann boundary conditions, the balance of linear momentum has the following weak form

$$\int_{\mathcal{B}} [\nabla \delta \mathbf{u} : \boldsymbol{\tau} + \delta \mathbf{u} \cdot \mathbf{B}] dV + \int_{\varphi(\partial\mathcal{B}_\tau)} \delta \mathbf{u} \cdot \hat{\mathbf{t}} da = 0 \quad (5.33)$$

The second governing equation for the model including gradient enhancement is averaging equation discussed in Section 5.2 with homogeneous Neumann boundary conditions. The weak form of Equations (5.27) and (5.28) can be obtained after standard derivation and reads, respectively:

$$\int_{\mathcal{B}} [[z - z_{loc}] \delta z + l_{mat}^2 \nabla_0 z \cdot \nabla_0 \delta z] dV = 0 \quad (5.34)$$

$$\int_{\varphi(\mathcal{B})} [[z - z_{loc}] \delta z + l_{spat}^2 \nabla z \cdot \nabla \delta z] dv = 0 \quad (5.35)$$

where δz is a test function.

5.4 Aspects of implementation within AceGen

5.4.1 Computational approach for isothermal models coupled with gradient averaging

As it was discussed in Chapter 4 the numerical problem is solved using Newton-Raphson procedure in the finite element method. Moreover, due to automatic consistent linearization, a monolithic solution scheme is used to solve coupled problems.

The analyzed model involves two interpolated fields: displacements and nonlocal variable, thus, the vector of nodal unknowns for a finite element is written

$$\mathbf{p} = [\mathbf{u}_I, \mathbf{z}_I] \quad (5.36)$$

where \mathbf{u}_I is a vector including nodal displacements and \mathbf{z}_I – nodal nonlocal variables. The interpolation defined in Equation (4.5) is used

$$\mathbf{d}_{el} = \mathbf{N}_I \cdot \mathbf{p} = [\mathbf{N}_{u,I}, \mathbf{N}_{z,I}] \cdot [\mathbf{u}_I, \mathbf{z}_I] \quad (5.37)$$

but now the interpolation for both unknown fields might be performed with different shape functions i.e. $\mathbf{N}_{u,I} \neq \mathbf{N}_{z,I}$, for instance quadratic for displacements and linear for the nonlocal variable, as it will be discussed later.

Consistently with the computational strategy presented in Section 4.3 the residual vector is computed on the basis of potentials related to governing equations. For the balance of linear momentum (5.30) the potential is the Helmholtz free energy functional from Equation (5.5) (for detailed explanation see [Korelc, 2009]) whereas for averaging equations (5.27) and (5.28) the following potential forms are proposed, respectively:

$$\Pi_z = \frac{1}{2} \left[[z - z_{loc}]^2 + l_{mat}^2 \nabla_0 z \cdot \nabla_0 z \right] \quad (5.38)$$

$$\Pi_z = \frac{1}{2} \left[[z - z_{loc}]^2 + l_{spat}^2 \nabla z \cdot \nabla z \right] \quad (5.39)$$

The above functionals are assumed in such a form that equation $\delta\Pi_z = 0$ is equivalent to the weak form of averaging equations (5.34) and (5.35). The local variable z_{loc} is equal to, depending on the model, history parameter κ^d defined in Equation (5.25) (elasto-plasticity with degradation) or strain measure governing damage $\bar{\varepsilon}$ from Equations (5.19) or (5.20) (elasto-plasticity with damage).

Now, on the basis of potentials (5.5) and (5.38) or (5.39) and the numerical integration discussed in Section 4.3, the Gauss point contribution to the residual vector is computed as follows

$$\mathbf{R}_G = [\mathbf{R}_{u,G}, \mathbf{R}_{z,G}] \quad (5.40)$$

where the first part $\mathbf{R}_{u,G}$ is related to the balance of linear momentum and the second $\mathbf{R}_{z,G}$ to the averaging equation:

$$\mathbf{R}_{u,G} = \frac{\partial \psi^e}{\partial \mathbf{u}_I}, \quad \mathbf{R}_{z,G} = \frac{\partial \Pi_z}{\partial \mathbf{z}_I} \quad (5.41)$$

Finally, the Gauss point contribution to the consistent tangent matrix is derived with Equation (4.9) and for the analyzed problem it is a non-symmetric matrix consisting of four parts

$$\mathbf{K}_G = \frac{\partial \mathbf{R}_G}{\partial \mathbf{p}} = \begin{bmatrix} \frac{\partial \mathbf{R}_{u,G}}{\partial \mathbf{u}_I} & \frac{\partial \mathbf{R}_{u,G}}{\partial \mathbf{z}_I} \\ \frac{\partial \mathbf{R}_{z,G}}{\partial \mathbf{u}_I} & \frac{\partial \mathbf{R}_{z,G}}{\partial \mathbf{z}_I} \end{bmatrix} = \begin{bmatrix} \mathbf{K}_{uu} & \mathbf{K}_{uz} \\ \mathbf{K}_{zu} & \mathbf{K}_{zz} \end{bmatrix} \quad (5.42)$$

Apart from sub-matrix \mathbf{K}_{zu} , which is zero if material averaging is used, all others parts of the tangent matrix are non-zero.

5.4.2 Finite element types

In this work the implementation and the numerical analysis of the presented models are performed in three-dimensional space. The finite elements under consideration are based on hexahedral topology including 8 or 20 nodes. Particularly, the following ones are taken into account, cf. Figure 5.3:

- elements H1 - standard eight-noded hexahedron with linear interpolation of the displacements and nonlocal variable fields,
- elements H2S - 20-noded Serendipity hexahedron with quadratic interpolation of displacements and linear interpolation of the nonlocal variable field,
- elements H1+ F -bar - eight-noded hexahedron with linear interpolation of the unknown fields with F -bar modification, which is explained below.

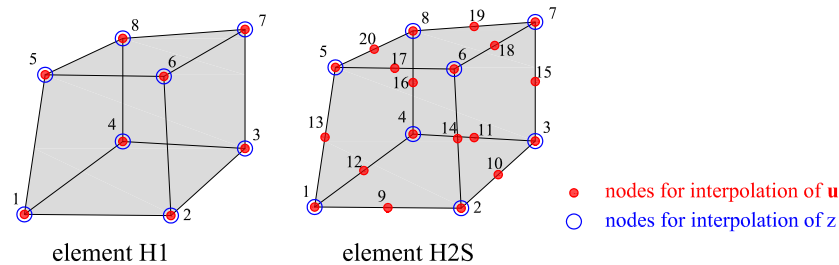


Figure 5.3: Topology of finite elements under consideration

If the linear interpolation of the displacement field is applied in the finite element method then a locking phenomenon can be observed which manifests itself in the spurious hardening in numerical simulations. Apart from the increase of the interpolation order (for example using elements H2S), there are a few methods to prevent standard elements from locking such as the enhanced assumed strain [Simo and Rifai, 1990], the selective integration or B -bar method [Hughes, 1980]. In this work the large strain counterpart of the last method called the F -bar approach is applied according to [de Souza Neto et al., 2008]. The approach involves the replacement of the deformation gradient \mathbf{F} with its modified counterpart $\bar{\mathbf{F}}$. The formulation is based on a multiplicative split of the deformation gradient into its volumetric and isochoric parts

$$\mathbf{F} = \mathbf{F}^{iso} \mathbf{F}^{vol} \quad (5.43)$$

To calculate $\bar{\mathbf{F}}$ for a Gauss point the volumetric part of the deformation gradient is taken from the centroid of the element whereas the isochoric part is calculated at the proper integration point. The modified deformation gradient $\bar{\mathbf{F}}$ is used for all computations and is saved in the history data to be used in the next time step. The implementation of *F-bar* modification is presented in Box 1.

Given:

Current deformation gradient at given integration point $\mathbf{F} = \mathbf{I} + \frac{\partial \mathbf{u}}{\partial \mathbf{X}}$

Do:

1. Compute current deformation gradient at centroid of element \mathbf{F}_0
2. Compute modified deformation gradient $\bar{\mathbf{F}} = \sqrt[3]{\frac{\det(\mathbf{F})}{\det(\mathbf{F}_0)}} \mathbf{F}$
3. Replace deformation gradient \mathbf{F} with $\bar{\mathbf{F}}$

Box 1. *F-bar* modification for finite element [de Souza Neto et al., 2008]

5.5 Algorithms for isothermal models solved in AceGen

5.5.1 Solution of finite elasto-plasticity

The majority of analyzed models in the dissertation include the plastic behaviour. Therefore, now the solution algorithm for the isothermal finite elasto-plasticity at the level of an integration point is presented which will be used later for the more complex models, e.g. coupled with gradient damage or thermal effects.

Let us consider a time interval $[t_n, t_{n+1}]$. The solution at t_n is known, particularly, the deformation gradient \mathbf{F}_n , the elastic left Cauchy-Green deformation tensor \mathbf{b}_n^e and the measure of accumulated plastic flow γ_n . The nodal displacements are computed and hence known at time t_{n+1} . Thus, from a computational point of view, the nonlinear material behaviour is treated as configuration driven [Auricchio and Taylor, 1999]. For the sake of brevity, all quantities related to the current time step t_{n+1} are written without indices.

Firstly, the trial stress state is determined to verify if the plastic regime is entered. Following [Simo and Hughes, 1998] the relative deformation gradient is computed

$$\mathbf{f} = \mathbf{F}\mathbf{F}_n^{-1} \quad (5.44)$$

where \mathbf{F}_n is taken from the history and the current value of the deformation gradient is calculated on a basis of interpolated current displacement function $\mathbf{F} = \mathbf{I} + \frac{\partial \mathbf{u}}{\partial \mathbf{X}}$.

Assuming that the relative deformation gradient is elastic the trial elastic left Cauchy-Green tensor is calculated

$$\mathbf{b}_{tr}^e = \mathbf{f}\mathbf{b}_n^e\mathbf{f}^T \quad (5.45)$$

and the corresponding effective trial Kirchhoff stress tensor is derived from the hyper-elastic constitutive relation (5.7a). Now the yield function (5.9) is computed using the trial Kirchhoff stress tensor and the value of the accumulated plastic strain measure from the previous time step. If the yield function has a negative value then the step

is indeed elastic: trial values are the sought solution. On the other hand if the yield criterion is not satisfied, the nonlinear equations including the return map equations and the yield condition must be solved [Auricchio and Taylor, 1999]. They are written in residual form as:

$$\begin{cases} \mathbf{R}_{be} = \mathbf{b}^e - \exp[-2[\gamma - \gamma_n]\mathbf{N}^p(\boldsymbol{\tau}(\mathbf{b}^e))]\mathbf{b}_{tr}^e = \mathbf{0} \\ R_y = F^p(\boldsymbol{\tau}(\mathbf{b}^e), \gamma) = 0 \end{cases} \quad (5.46)$$

The system (5.46) consists of seven scalar equations (due to the symmetry of \mathbf{b}^e), with seven unknowns: six components of \mathbf{b}^e and γ . To find the solution of system (5.46) the Newton-Raphson procedure is applied. Aspects of the solution of finite elasto-plasticity using matrix exponential are included in [Korelc and Stupkiewicz, 2014].

It should also be added here, that in the numerical procedure not exactly the values of components of the elastic left Cauchy-Green tensor \mathbf{b}^e are computed but components of auxiliary tensor \mathbf{b}^{e*} , which fulfill the relation: $\mathbf{b}^e = \mathbf{f}\mathbf{b}^{e*}\mathbf{f}^T$. The reason for this manipulation is to obtain finally not only the values of the current tensor \mathbf{b}^e components, but also the functional dependence between the displacements and the deformation tensor \mathbf{b}^e , which can otherwise be lost in the iterative procedure of Newton-Raphson.

To avoid the differentiation of all steps of the inner Newton-Raphson iterative procedure, the definition of the automatic differentiation exception should be used to prescribe the derivatives of the internal variables with respect to the independent solution vector. The detailed explanation of this crucial aspect of algorithm is included in [Korelc, 2009] and [Korelc, 2008].

The summarized algorithm for the finite elasto-plasticity material model is presented in Box 2.

5.5.2 Solution of nonlocal finite elasto-plasticity with damage

Gradient damage and plasticity in the model presented in Section 5.1.3 are indirectly coupled, thus the code at the level of an individual Gauss point can be divided into three parts including the implementation of:

- the plasticity problem in the effective stress space
- the damage state in the real stress space
- the residual vector including the equilibrium and averaging equations, and the consistent tangent matrix

Firstly, the plastic problem is solved in the effective stress space using algorithm from Section 5.5.1 (the Kirchhoff stress tensor $\boldsymbol{\tau}$ in this algorithm is regarded now as effective tensor $\hat{\boldsymbol{\tau}}$) and the final value of tensor \mathbf{b}^e and γ are determined. The next step is the verification of damage condition (5.21a) which takes into account the nonlocal deformation measure z instead of $\tilde{\varepsilon}$. If the averaged measure exceeds the previous value of the damage history parameter κ_n^d , then damage increases in relation to the previous time step, and a new value of the history parameter is equal to nonlocal strain measure $\kappa^d = z$ which is interpolated from nodal degrees of freedom \mathbf{z}_I . Otherwise, there is no damage growth and the history parameter does not change its value. The damage

variable ω^d is computed from Equation (5.16) using the current value of the history parameter κ^d and is used for the calculation of degraded free energy function (5.15).

Given at element level:

- Current vector of nodal displacements $\mathbf{p} = \mathbf{u}_I$
- Isoparametric interpolation
- Integration point variables at the end of previous step, i.e.: deformation gradient \mathbf{F}_n , elastic left Cauchy-Green tensor \mathbf{b}_n^e , plastic strain measure γ_n ,

Compute at integration point:

1. Current deformation gradient $\mathbf{F} = \mathbf{I} + \frac{\partial \mathbf{u}}{\partial \mathbf{X}}$
2. For F-bar element – go to Box 1
3. Relative deformation gradient $\mathbf{f} = \mathbf{F}\mathbf{F}_n^{-1}$
4. Trial elastic left Cauchy-Green tensor $\mathbf{b}_{tr}^e = \mathbf{f}\mathbf{b}_n^e\mathbf{f}^T$
5. Trial elastic free energy potential $\psi^e(\mathbf{b}_{tr}^e)$ (5.5)
6. Trial Kirchhoff stress tensor $\boldsymbol{\tau}_{tr} = 2\frac{\partial \psi^e}{\partial \mathbf{b}_{tr}^e}\mathbf{b}_{tr}^e$
7. Yield function for trial stress $F^p(\boldsymbol{\tau}_{tr}, \gamma_n)$ (5.9)
8. Yield condition:
If $F^p < 0$ then state is admissible $\rightarrow \mathbf{b}^e = \mathbf{b}_{tr}^e, \gamma = \gamma_n$
Else state is inadmissible \rightarrow Compute \mathbf{b}^e and γ from:

$$\begin{cases} \mathbf{R}_{be} = \mathbf{b}^e - \exp[-2[\gamma - \gamma_n]\mathbf{N}(\boldsymbol{\tau}(\mathbf{b}^e))]\mathbf{b}_{tr}^e = \mathbf{0} \\ R_y = F^p(\boldsymbol{\tau}(\mathbf{b}^e), \gamma) = 0 \end{cases}$$
 and set AD exceptions for dependence between internal variables and nodal unknowns [Korelc, 2009]
9. Elastic free energy potential $\psi^e(\mathbf{b}^e)$ (5.5)
10. Gauss point contributions to residual vector $\mathbf{R}_{u,G}$ (5.41a)
and tangent matrix $\mathbf{K}_G = \frac{\partial \mathbf{R}_{u,G}}{\partial \mathbf{p}}$ related to balance of linear momentum

Box 2. Solution algorithm for finite elasto-plasticity

5.5.3 Solution of nonlocal finite elasto-plasticity with degradation

The algorithm for the solution of elasto-plasticity coupled with gradient degradation discussed in Section 5.1.4 is presented in Box 3. In fact, the main difference between this algorithm and the numerical treatment of elasto-plasticity from Box 2 is the computation of yield function F_p which now takes into account the nonlocal variable.

5.6 Numerical simulations

5.6.1 Nonlocal finite elasto-plasticity with damage

In order to assess the performance of the material models described above, the selected results of numerical simulations are presented¹. All tests have been performed using the finite element environment AceFEM [Korelc, 2011]. Due to the complexity of the examined model only selected aspects have been analyzed. Firstly, test results related to different finite element types discussed in Section 5.4.2 are presented, secondly a comparison of spatial and material averaging for the elastic-gradient-damage model is performed (thus plasticity is not entered in this case). Next, simulations for the different nonlocal strain measures for gradient-damage plasticity are included and finally the influence of the applied yield function (HMH or BDP) is tested.

Given at element level:

- Current vector of nodal displacements and nonlocal variables $\mathbf{p} = [\mathbf{u}_I, \mathbf{z}_I]$
- Isoparametric interpolation
- Integration point variables at the end of previous step, i.e.: deformation gradient \mathbf{F}_n , elastic left Cauchy-Green tensor \mathbf{b}_n^e , plastic strain measure γ_n , damage history parameter κ_n^d

Compute at each integration point:

1. Solution of plasticity in effective stress space using steps 1-8 from Box 2
2. Damage loading function $F^d(z, \kappa^d)$, where $z = \bar{\varepsilon}$
3. Damage condition:
If $F^d < 0$ then there is no damage growth $\rightarrow \kappa^d = \kappa_n^d$
Else damage grows $\rightarrow \kappa^d = z$
4. Damage variable $\omega^d(\kappa^d)$ (5.16)
5. Elastic free energy potential $\psi^{e,d} = (1 - \omega^d)\psi^e$
6. Local strain measure $\tilde{\varepsilon}$ (5.19) or (5.20)
7. Potential for averaging equation Π_z (5.38) or (5.39)
8. Gauss point contributions to residual vector $\mathbf{R}_G = [\mathbf{R}_{u,G}, \mathbf{R}_{z,G}]$ and tangent matrix \mathbf{K}_G

Box 3. Solution algorithm for large strain gradient-enhanced elasto-plasticity with damage

Two specimens are analyzed in this section: a bar with variable cross-section along the length (VCSB) and a perforated plate (PP) - both specimens are in tension. The dimensions and the boundary conditions of the samples are presented in Figures 5.4 and 5.6, whereas the applied discretizations in Figures 5.5 and 5.7.

¹ The results presented in this section (apart from subsection *Yield criterion vs damage growth*) were published in paper [Wcisło et al., 2013]

Given at element level:

- Current vector of nodal displacements and nonlocal variables $\mathbf{p} = [\mathbf{u}_I, \mathbf{z}_I]$
- Isoparametric interpolation
- Integration point variables at the end of previous step, i.e.: deformation gradient \mathbf{F}_n , elastic left Cauchy-Green tensor \mathbf{b}_n^e , plastic strain measure γ_n ,

Compute at integration point:

1. Calculate trial state using steps 1-7 from Box 2.
2. Yield function for trial stress $F_p(\boldsymbol{\tau}_{tr}, \gamma_n, z)$ where $z = \bar{\kappa}^p$
3. Yield condition:
If $F^p < 0$: state is admissible $\rightarrow \mathbf{b}^e = \mathbf{b}_{tr}^e, \gamma = \gamma_n$
Else: state is inadmissible \rightarrow Compute \mathbf{b}^e and γ from:

$$\begin{cases} \mathbf{R}_{be} = \mathbf{b}^e - \exp[-2[\gamma - \gamma_n]\mathbf{N}(\boldsymbol{\tau}(\mathbf{b}^e))]\mathbf{b}_{tr}^e = \mathbf{0} \\ R_y = F_p(\boldsymbol{\tau}(\mathbf{b}^e), \gamma, z) = 0 \end{cases}$$
 and set AD exceptions for dependence between internal variables and nodal unknowns [Korelc, 2009]
4. Potentials ψ^e and Π_z
5. Gauss point contributions to residual vector $\mathbf{R}_G = [\mathbf{R}_{u,G}, \mathbf{R}_{z,G}]$ and tangent matrix \mathbf{K}_G

Box 4. Solution algorithm for large strain gradient-enhanced elasto-plasticity with degradation

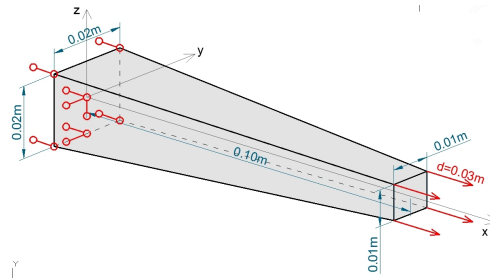


Figure 5.4: Geometry and boundary conditions for VCSB

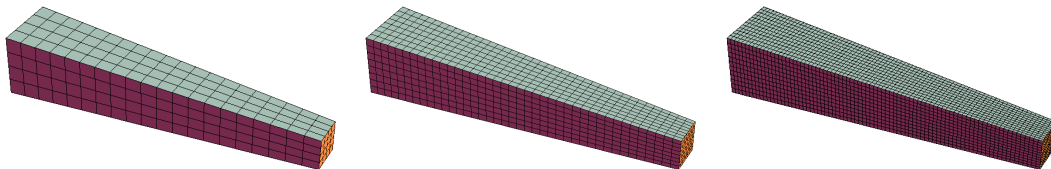


Figure 5.5: Discretizations of VCSB: 20x4x4 (coarse mesh), 40x8x8 (medium mesh) and 80x12x12 (fine mesh)

The material model parameters which are applied for this simulations are presented in Table 5.1. If other values are considered then it is stated in the test description.

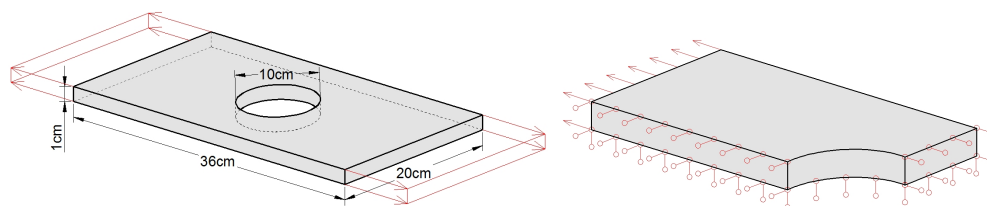


Figure 5.6: Geometry and boundary conditions for PP

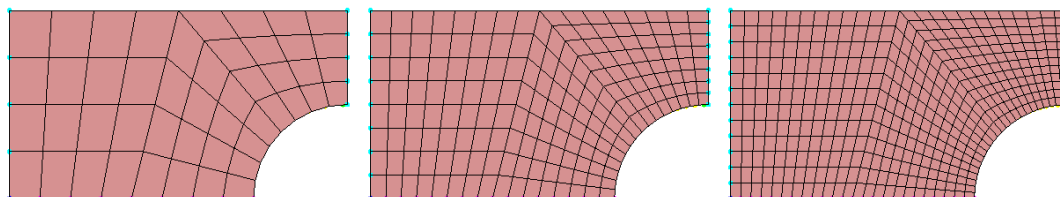


Figure 5.7: Discretizations of PP: 48, 192 and 432 elements

Property	Symbol	Value	Unit
Young modulus	E	200e9	N/m ²
Poisson ratio	ν	0.3	-
Damage threshold	κ_0^d	0.04	-
Damage evolution law parameter	α^d	0.95	-
Damage evolution law parameter	β^d	5	-
Internal length scale for material averaging	l_{mat}	0.01	m
Internal length scale for spatial averaging	l_{spat}	0.01	m
Initial yield threshold	σ_{y0}	333e6	N/m ²
Material constant for BDP yield function	α_p	0.116	-
Hardening modulus	H_i	20e9	N/m ²

Table 5.1: Summary of material properties used for numerical simulations

Tests for different elements

The first group of simulations are performed for different types of the finite elements.

The first simulation is performed for the material model of elasto-plasticity and the VCSB specimen. The diagram presenting the sum of reactions on the supported end of the sample versus the displacement imposed at the other end is shown in Figure 5.8. It can be observed that the diagrams for elements H1 differ significantly from the other diagrams and they depend on the adopted discretization. The reason for that behaviour is the locking phenomenon which causes a stiffer sample response. The results for elements H1+ \bar{F} and elements H2S coincide in the pre-peak regime. For each diagram softening of the material can be observed which is caused by the geometrical effects - necking. This phenomenon occurs although plasticity with hardening is applied. In the post-peak regime the results differ for each mesh which motivates regularization.

The second test is performed using PP and elasto-plastic model coupled with gradi-

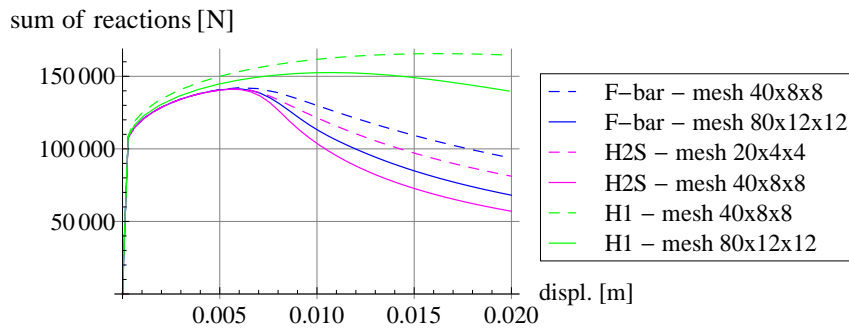


Figure 5.8: Sum of reactions vs displacements for different elements (elasto-plasticity, VCSB)

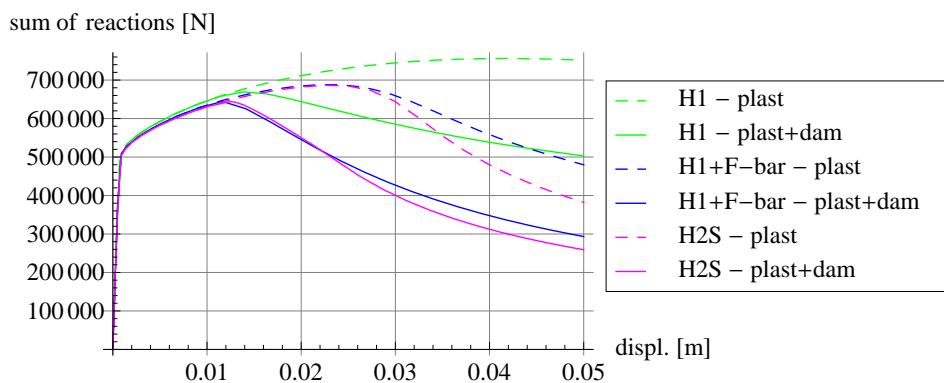


Figure 5.9: Sum of reactions vs stretch ratio (elasto-gradient-damage-plasticity, PP)

ent damage. In this test the damage threshold is assumed to be equal to $\kappa_0^d = 0.003$ and material averaging is applied with internal length $l_{mat} = 0.02$.

The graph presenting the sum of reactions vs enforced displacement is presented in Figure 5.9. It can be noticed that the behaviour of the elasto-plastic material (dashed lines) is similar to the previous test: the results for elements H1+*F-bar* and H2S are similar whereas the model simulated with elements H1 exhibits a larger stiffness. Also in this test, in spite of plasticity with hardening, necking can be observed. If the model coupled with gradient damage is taken into account, then the results for H1+*F-bar* and H2S coincide up to beginning of the necking process (for $u \approx 0.024$ m). It can be noticed that although the gradient averaging is applied in the model it does not prevent the numerical results from the mesh-sensitivity for the softening caused by geometrical effects.

The deformed meshes with the plastic strain measure distribution at the end of the elongation for the three considered types of finite elements are presented in Figure 5.10. It can be observed that the deformation obtained for elements H1 differs significantly from the other results: the localization zone is wider and covers more rows of the elements.

Taking the observation from these simulations into account the following computations are performed for elements H1+*F-bar*.

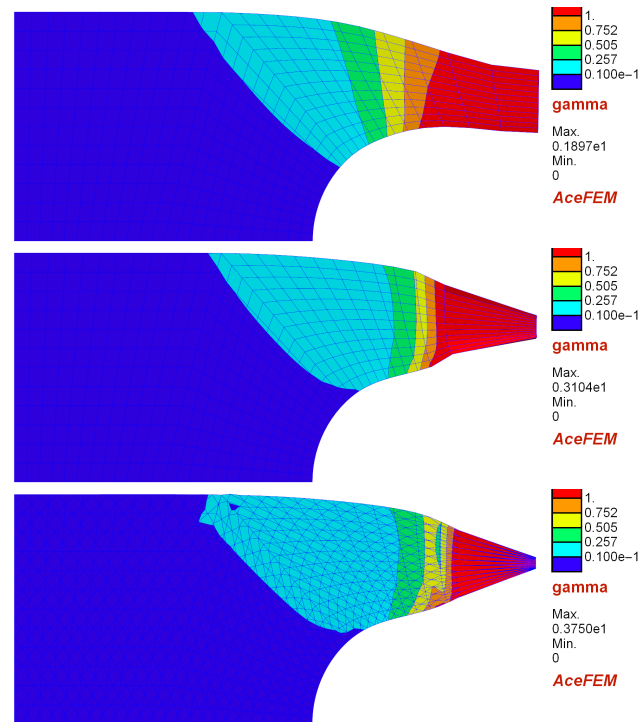


Figure 5.10: Deformed mesh with plastic strain measure distribution at the end of elongation process for elements H1 (upper), $H1+F\text{-bar}$ (middle), H2S (lower) for gradient-enhanced elasto-plasticity with damage (fine mesh)

Spatial vs material averaging

As it was mentioned, gradient averaging applied to large strains can be performed in the undeformed or in the current configuration. To investigate the behaviour of models with these two kinds of averaging the following numerical tests are performed.

Firstly, the VCSB example is analyzed. The application of the sample whose cross-section is variable implies that the cross-section where damage occurs at first is prescribed - it is the narrowest end of the bar. The internal length parameter is assumed to be constant $l = 0.01$ m during the deformation process and has the same value for both material and spatial averaging. This group of tests is performed for the elasticity-gradient-damage model.

Figure 5.11 depicts the sum of reactions versus the enforced displacements. Although the simulations are performed with identical material parameters, the response for the two types of averaging differs significantly. Firstly, it can be observed that the post-peak branch for the model with spatial averaging descends more rapidly than for material averaging. Secondly, the application of spatial averaging does not result in mesh-insensitivity: for each discretization the diagram is different. The results for material averaging for all analyzed discretizations are close, and the diagrams for the second and the third mesh almost coincide.

It is shown in Figures 5.12 and 5.14 how the specimen deforms and how the first component of the Green strain tensor E_{xx} and damage variable ω are distributed. Moreover, in Figure 5.13 the evolution of E_{xx} along the bar length is depicted.

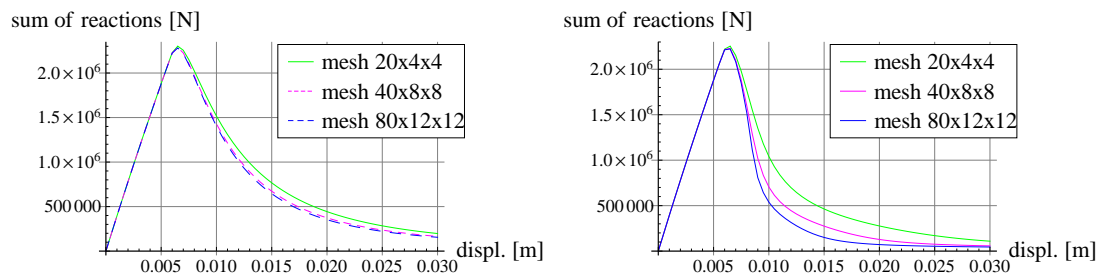


Figure 5.11: Displacement vs reaction sum for material and spatial averaging and different discretizations

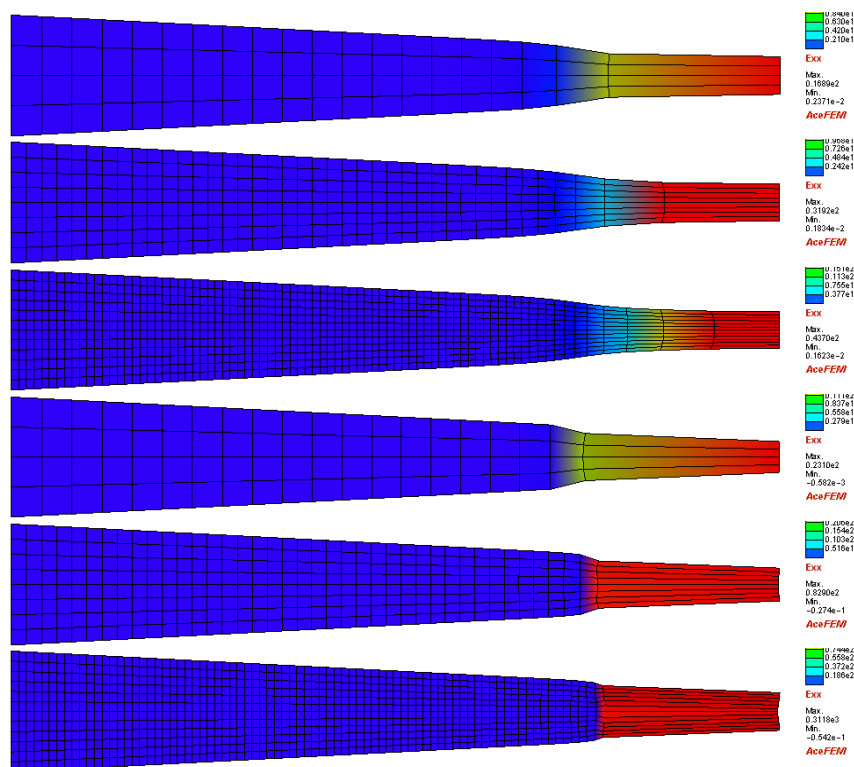


Figure 5.12: Deformed meshes at the end of tension test with E_{xx} distribution for material averaging (upper three pictures) and spatial averaging (lower three pictures) - elasticity-gradient-damage, VCSB

It can be observed that for spatial averaging the deformation and the strain distribution depend on the finite element discretization, whereas for material averaging the response is similar for different meshes. It can be noticed in Figure 5.13 that as the enforced displacement increases the strain localization zone gets narrower for spatial averaging. For large enough deformation, strains concentrate in one row of elements for all analyzed discretizations. Although in the considered description the gradient regularization is applied, it does not fully preserve the numerical simulations from the pathological mesh-sensitivity.

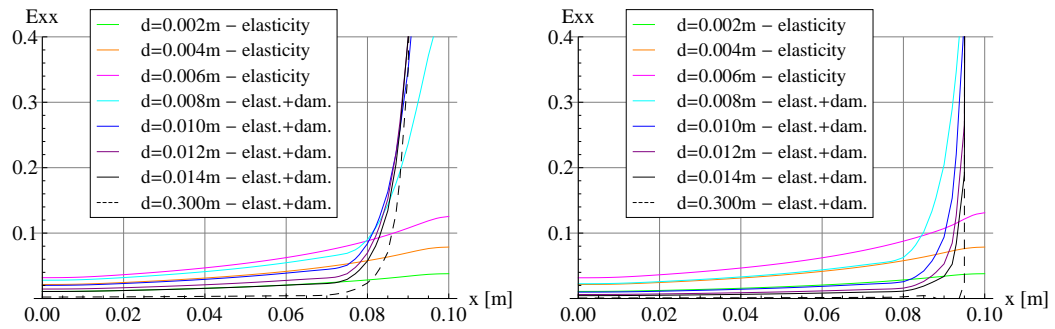


Figure 5.13: Evolution of the first component of Green strain tensor E_{xx} for material (on the left) and spatial (on the right) averaging - medium mesh (elasticity-gradient-damage, VCSB)

It can be noticed in Figure 5.14 that the damage zone is similar for all discretizations for spatial averaging although the deformation differs significantly. The phenomenon is caused by irreversibility of the state of material damage. The damage area which arises at the beginning of the loading process does not become smaller even if further deformation concentrates in the gradually smaller band and the rest of the sample is unloaded.

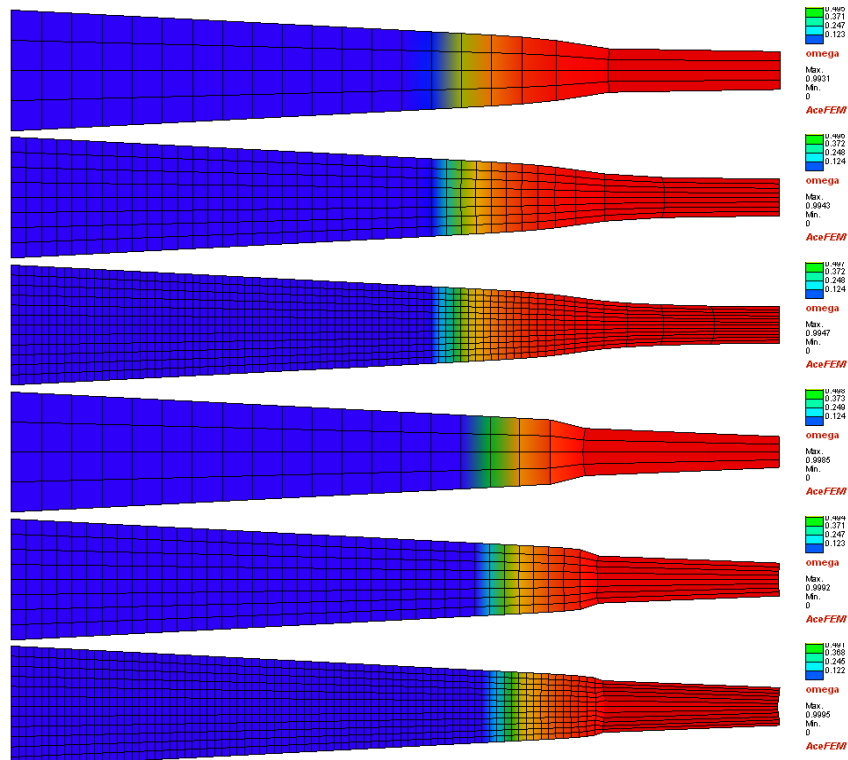


Figure 5.14: Deformed meshes at the end of tension test with damage variable ω_d distribution for material averaging (upper three pictures) and spatial averaging (lower three pictures)

The phenomenon of mesh-sensitivity observed for spatial averaging was noticed in the paper of [Steinmann, 1999], however without detailed explanation. To investigate the reason for such behaviour the evolution of material or spatial length scale parameters for the two kinds of averaging is studied (Figure 5.15). The relation between parameters presented in Figure 5.15 is expressed through Equation (5.29). In the first diagram we can observe the evolution of the material internal length along the bar for the medium mesh whereas the spatial one is fixed. The value of the length parameter decreases in the damage zone with increasing loading. On the other hand, if the material internal length is fixed, the value of the spatial one grows at the end of the bar with the smaller cross-sectional area. It can also be observed that for spatial averaging the corresponding material length scale at the narrowest end of the bar decreases to the value less than 0.001 m whereas the size of element for the medium mesh is equal to 0.0025 m. Numerical experiments reveal that for the assumed material parameters and the VCSB specimen (mesh 40x8x8) the application of the constant internal length for material averaging less than 0.002 m results in the localization of strains in one row of elements.

For the deformation process performed for spatial averaging it can be observed that the zone where the strains grow gradually narrows and finally reduces to one row of elements when the corresponding material internal length is small enough.

To conclude, the averaging performed with the constant spatial internal scale and fixed mesh in the deformed configuration causes the effect that for strains large enough the gradient enhancement does not preserve the solution from mesh sensitivity. To remove the dependence on the discretization for spatial averaging an adaptative mesh refinement can be considered.

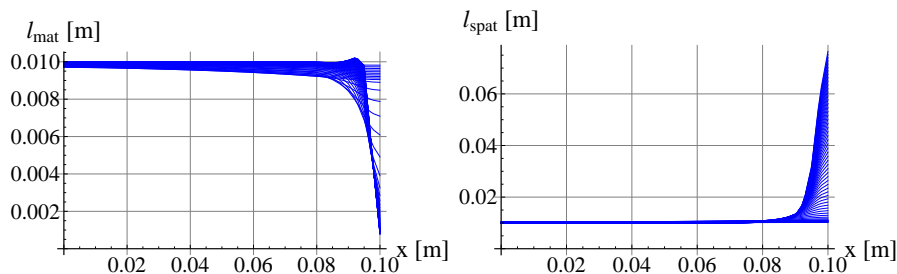


Figure 5.15: Evolution of material internal length whereas spatial is fixed and conversely, mesh 40x8x8

Tests for different strain measures

In the following simulations the dependence of the results on the adopted strain measure which governs the damage evolution is investigated. Two measures introduced in Section 5.1.3 are taken into account:

$$\tilde{\varepsilon}_1 = \det(\mathbf{F}) - 1, \quad \tilde{\varepsilon}_2 = \sqrt{(e_1^+)^2 + (e_2^+)^2 + (e_3^+)^2}$$

Firstly, the simulations for VCSB are performed for the coarse and the medium mesh, and the elastic-damage model with material averaging. In order to initiate the

damage process at the same moment in the two considered cases, the damage threshold is assumed different for each measure: $\kappa_{0,\tilde{\varepsilon}_1}^d = 0.04$ and $\kappa_{0,\tilde{\varepsilon}_2}^d = 0.085$.

In Figure 5.16 the sum of reactions vs enforced displacements diagram is depicted. It can be observed that the results significantly differ for the two measures. If we assume the same damage evolution from Equation (5.24) with identical material parameters as in Table 5.1), then the model with $\tilde{\varepsilon}_1$ exhibits much stronger softening whereas for $\tilde{\varepsilon}_2$ the sum of reactions is degraded to a smaller extent. To verify if the difference is a result of the adopted parameters of the damage evolution law, the tests for $\tilde{\varepsilon}_2$ and a higher value of parameter $\beta^d = 20$ are performed. It turns out that although the sum of reactions reaches values smaller than previously, the diagram behaves in a different way: the loss of stiffness is very rapid in the first phase of the damage process and later it is more gentle, whereas for $\tilde{\varepsilon}_1$ the diagram descends rather uniformly. In the post-peak regime the snap-back would probably be observed if the arc-length control was applied instead of the enforcing displacement.

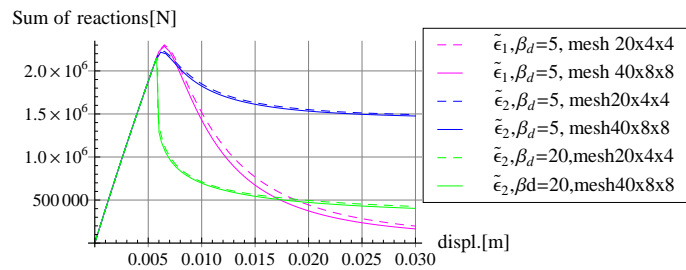


Figure 5.16: Sum of reactions for elasticity-gradient-damage model with different deformation measures - VCSB

When analysing the deformed mesh with the nonlocal variable distribution (Figure 5.17), the difference in the sample shape at the end of the deformation process can be noticed. For each test the deformation of the finite element mesh is different. Moreover, for $\tilde{\varepsilon}_1$ the nonlocal variable is almost twice larger than for $\tilde{\varepsilon}_2$.

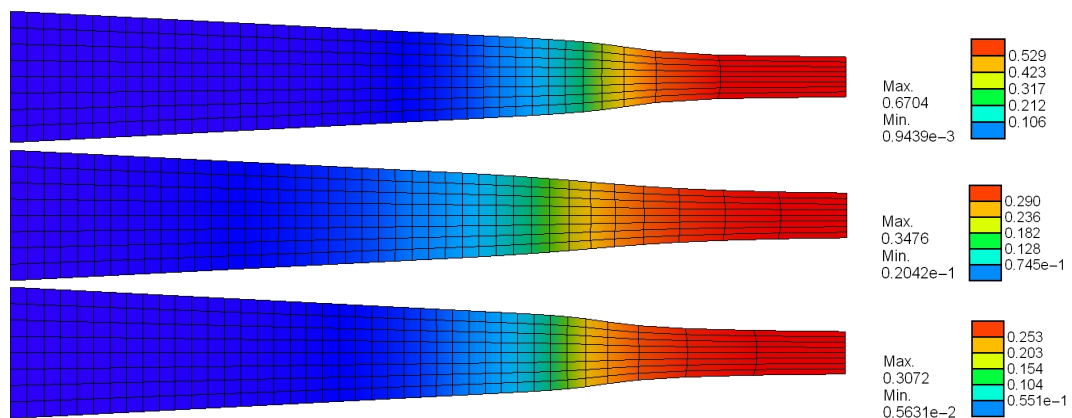


Figure 5.17: Deformed mesh and nonlocal variable distribution for: $\tilde{\varepsilon}_1$ and $\beta^d = 5$ (upper), $\tilde{\varepsilon}_2$ and $\beta^d = 5$ (middle), $\tilde{\varepsilon}_2$ and $\beta^d = 20$ (lower)

The second test is performed for the PP specimen with the same material parameters as previously apart from the internal length which is assumed to be $l = 0.02$ m. The sum of reactions vs displacement diagram (Figure 5.18) is similar to the response of VCSB: for the different measures governing damage the diagram presents the various responses of the sample.

On the other hand if the material model including plasticity coupled with gradient damage is considered (Figure 5.19) then the diagrams for the models with different strain measures are very close (notice however that we assumed $\kappa_{0,\tilde{\epsilon}_1}^d = 0.003$ and $\kappa_{0,\tilde{\epsilon}_2}^d = 0.007$).

Taking into account these results it can be concluded that the strain measure applied to the model is of high significance for elasticity with damage and should be carefully selected for a specific material to be analyzed. For the material model coupled with plasticity the choice of $\tilde{\epsilon}$ does not influence the results strongly.

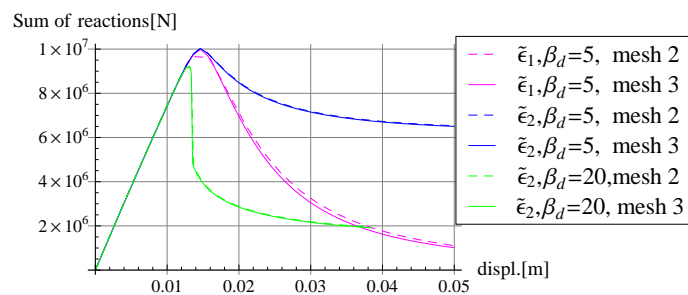


Figure 5.18: Sum of reactions for elasticity with gradient damage with different deformation measures - PP

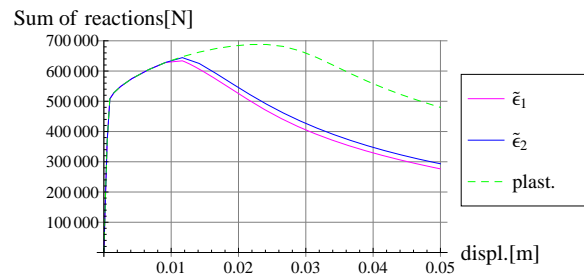


Figure 5.19: Sum of reactions for elasticity-gradient-damage-plasticity model with different deformation measures - PP

Yield criterion vs damage growth

In this section the results of VCSB elongation test for constitutive models including HMM and BDP yield functions are presented. The material parameters adopted for the simulations are introduced in Table 5.1 and the strain measure which governs damage is taken as in Equation (5.19).

Firstly, the elasto-plastic behaviour is investigated for VCSB simulated with medium and fine meshes. In Figure 5.20 the sum of reactions vs stretch ratio is presented. It can be observed that for the both constitutive laws the geometrical softening occurs and the

results are mesh-dependent in the post peak regime. The response of the material modelled with the HMH yield function exhibits higher stiffness than for the BDP function. Now the coupled elasticity-gradient-damage-plasticity model is analyzed. In the simu-

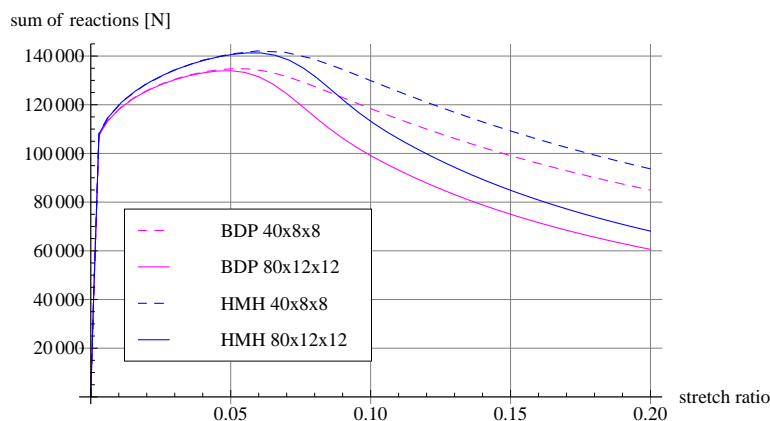


Figure 5.20: Sum of reactions vs load multiplier for elasto-plasticity with HMH and BDP yield criteria

lations different values of the damage thresholds are assumed for the HMH and BDP models: $\kappa_{0,HMH}^d = 0.0025$ and $\kappa_{0,BDP}^d = 0.02$. For such parameters the onset of the damage process is observed at the same stretch ratio. In Figure 5.21 the load-displacement diagrams are presented. The incorporation of damage into the constitutive model causes an earlier loss of stability and decreased stiffness of the response. The analysis of the change of nonlocal variable at the narrowest end of bar during deformation, presented in Figure 5.22, gives the information when the damage process is active during elongation. It can be observed that for the HMH model the damage process starts when the stretch ratio is about 0.025 and the value of the nonlocal variable reaches threshold $\kappa_{0,HMH}^d$. Successively, it stops when the stretch ratio is equal to 0.075 and the nonlocal variable has its maximum value. For the BDP plasticity the damage occurs for the stretch ratio equal to 0.025 and degrades the stiffness of the material until the end of the elongation process. The regime of the damage growth during deformation is denoted with a gray background in the diagrams in Figure 5.21. It is worth reminding that the HMH yield function represents volume preserving plasticity thus the application of strain measure from Equation (5.19) causes a growth of damage only in a certain limited part of the elongation whereas for BDP the reduction of stiffness is observed in the whole plastic process.

Finally, the results for different values of the internal length scales are presented in Figures 5.23 and 5.24. In the former one the diagrams of load-displacement relation are included. As it is expected the higher value of the internal length scale is the later the loss of stability occurs and the more ductile response is observed. In the latter figure the evolution of the nonlocal variable along x axis is presented. For the model which incorporates the BDP yield criterion the nonlocal variable reaches much higher values and is more concentrated than for HMH.

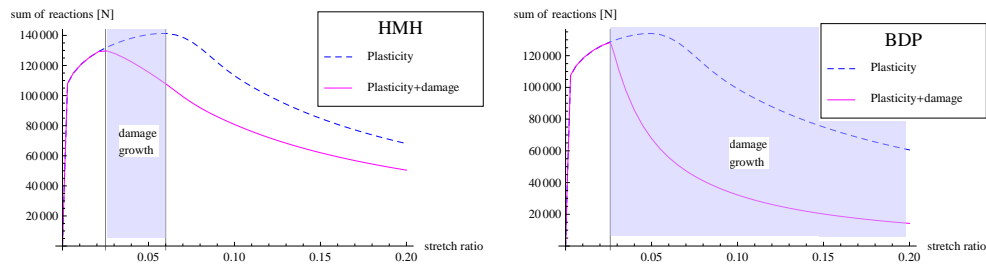


Figure 5.21: Sum of reactions vs stretch ratio for HMH and BDP yield criteria (results for fine mesh)

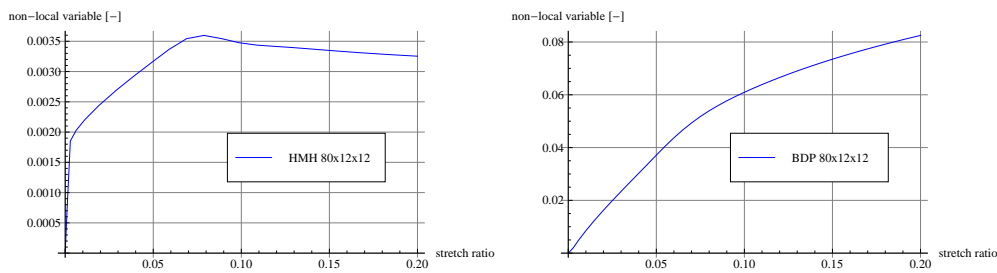


Figure 5.22: Value of nonlocal variable z at the narrowest end of bar vs stretch ratio (results for fine mesh)

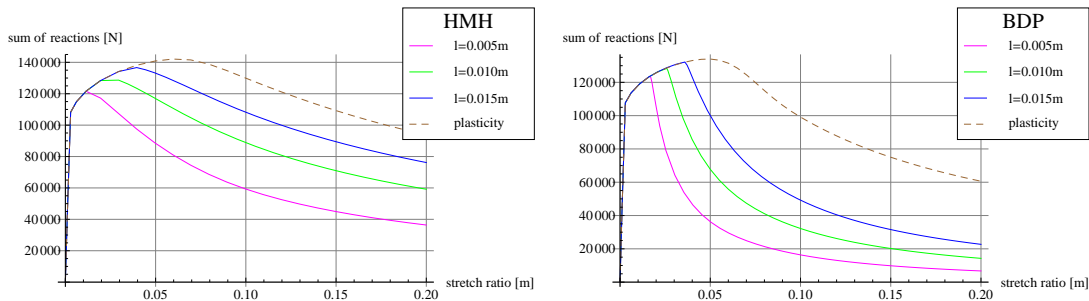


Figure 5.23: Sum of reactions vs stretch ratio for HMH and BDP yield criteria and different values of internal length parameter l

5.6.2 Nonlocal finite elasto-plasticity with degradation²

Now the second gradient-enhanced model is numerically tested. For the verification of material behaviour the simulations of an elongated plate under plane strain conditions are performed.

The tested specimen is a plate of dimensions: $L = 0.20$ m, $W = 0.10$ m, $H = 0.0025$ m which has a square imperfection in the centre ($L_{imp} = 0.005$ m), see Figure 5.25. Due to the symmetry of the specimen only one quarter of the plate is considered. The

²Results presented in this section was published by Mathematical Sciences Publishers in [Pamin et al., 2017]

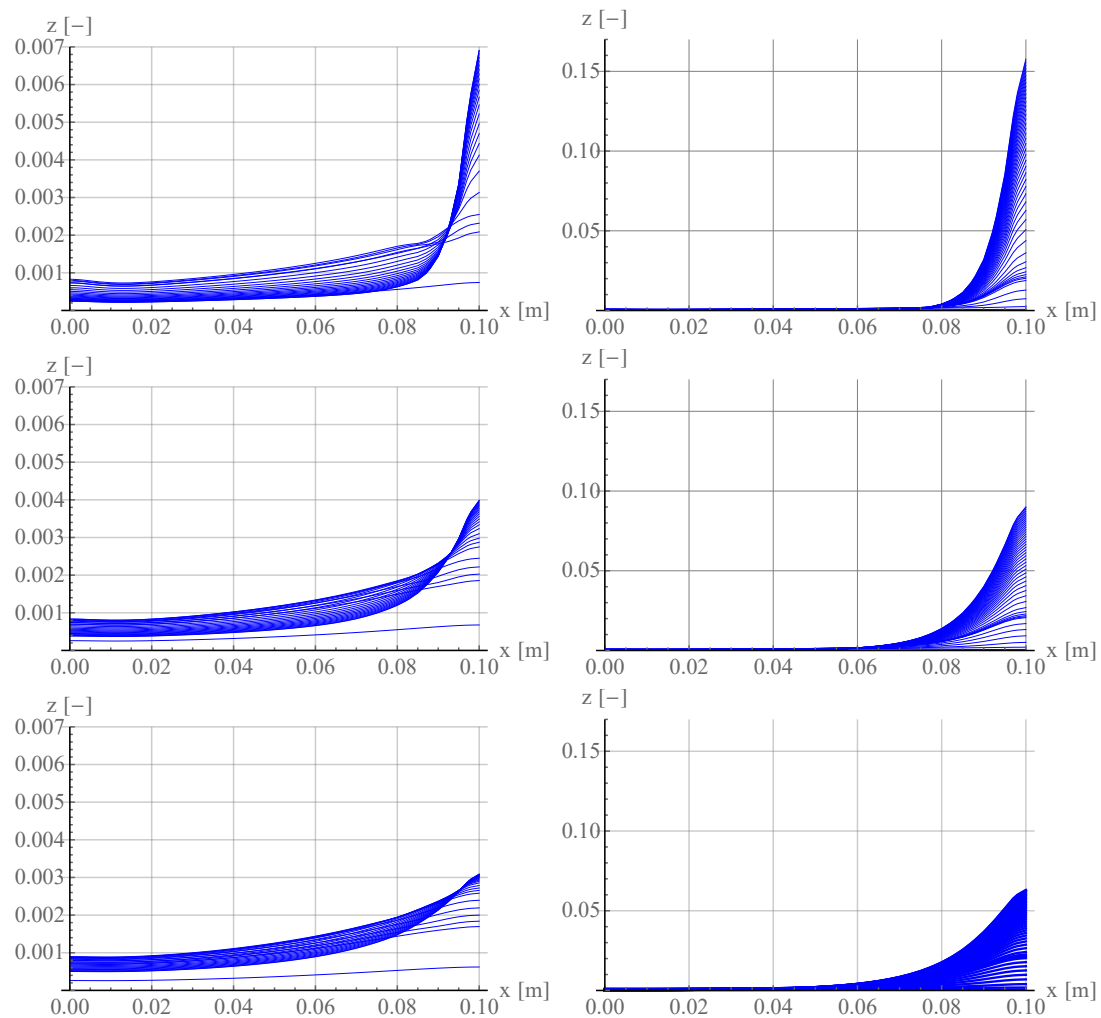


Figure 5.24: Nonlocal variable evolution for HMH (left column) and BDP (right column) yield criteria for different values of internal length scale: $l = 0.005$ m (upper), $l = 0.01$ m (middle) and $l = 0.015$ m (lower)

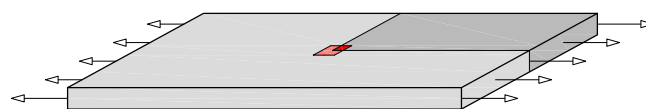


Figure 5.25: Plate in tension (implemented part coloured dark grey)

imperfection is assumed as the decrease of the initial yield stress to $\sigma_{y0,imp} = 0.8\sigma_{y0}$. The material parameters used in the simulations are presented in Table 5.2. Two non-zero values of the internal length parameter are assumed. The first one $l = 0.0025$ m is equal to the plate thickness and the dimension of the imperfection in the implemented quarter of the plate.

Plain strain conditions are applied (displacements at all nodes in the thickness direction are restrained) and the remaining mechanical boundary conditions are assumed in such a way that the deformation in the width direction is allowed. The enforced max-

Property	Symbol	Value	Unit
Bulk modulus	K	$164.2e9$	N/m ²
Shear modulus	G	$80.19e9$	N/m ²
Initial yield stress	σ_{y0}	$0.45e9$	N/m ²
Residual yield stress	$\sigma_{y\infty}$	$0.6e9$	N/m ²
Hardening modulus	H_i	$129e6$	N/m ²
Saturation coefficient	δ	16.93	–
Ductility	β	1	–
Internal length	l	0,0.0025,0.005	m

Table 5.2: Material parameters

imum displacement in the length-direction is equal to $u_{max} = 0.04$ m and is achieved after 1 s in adaptive steps.

The numerical model is generated using hexahedral elements and three finite element discretizations are used: 800 (mesh 1), 3200 (mesh 2) and 12800 (mesh 3) elements, see Figure 5.26.

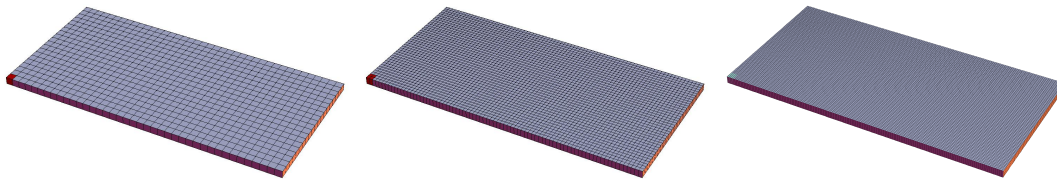


Figure 5.26: Finite element discretizations of plate in tension with imperfection (one quarter)

To investigate the influence of finite elements on the simulation of shear banding standard elements H1 and elements H1+ F -bar are tested. The discussion on two- and three-dimensional F -bar elements for the simulations of plane strain is included in Appendix A.

In the first test the response of the sample is obtained using standard hexahedral elements with linear interpolation of both fields (displacements and nonlocal variable) and no modification preventing the locking phenomenon is used.

In Figure 5.27 the sum of reactions vs load multiplier is presented. It can be observed that all results for the analyzed meshes coincide to a certain point in the post-peak regime. When the load multiplier reaches the value 0.48 the diagrams become distinct and, what is more, the value of the internal length scale does not influence the results strongly. The deformed meshes with the plastic strain measure distribution at the end of the deformation process are depicted in Figures 5.28 and 5.29. In the former figure the response of local model is shown ($l = 0$), whereas for the latter the internal length scale is equal to $l = 0.005$ m. It can be noticed that for mesh 1 and mesh 2 the localization has the form of necking rather than shear banding and can be described as a diffuse mode, whereas the response for mesh 3 can be specified rather as localized one. This is also consistent with the force-displacement diagrams in the post-peak regime and small influence of the internal length on the results. Also the differences in the

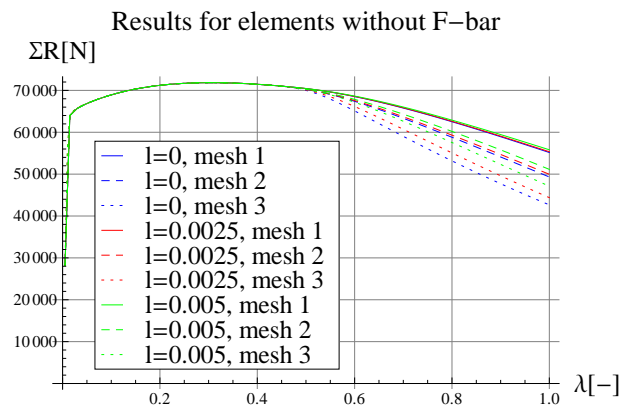


Figure 5.27: Sum of reactions vs displacement multiplier for nonlocal elasto-plasticity with degradation

deformations and the plastic strain distributions for the two values of internal length $l = 0$ and $l = 0.005$ m for both discretizations are minor. As expected, the higher value of l is adopted the smoother distribution of plastic strain is observed. To conclude, it can be observed that the results for the three applied discretizations differ and they are not mesh-convergent. In this case the volumetric locking causes equivocal response because each mesh predicts a different deformation mode.

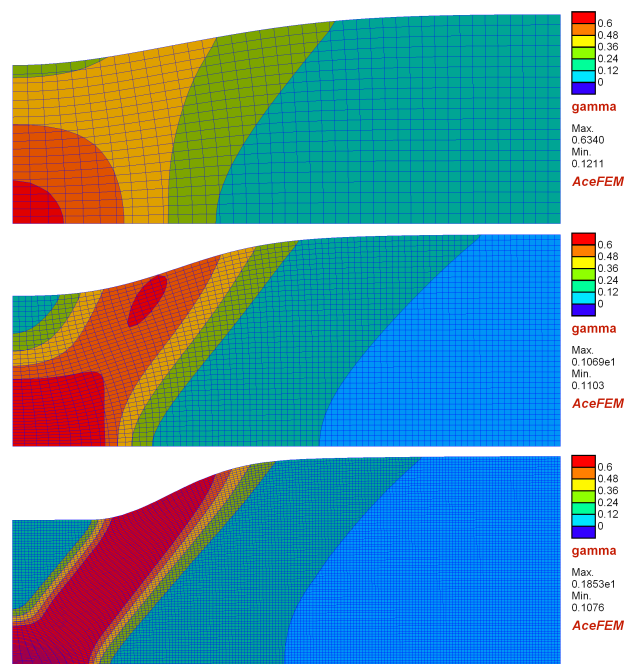


Figure 5.28: Deformed mesh with plastic strain measure γ distribution for mesh 1 (upper), mesh 2 (middle) and mesh 3 (lower) (local elasto-plasticity with degradation, elements without F -bar)

The next simulations are performed for the F -bar finite elements. In Figure 5.30 the load-displacement relation is depicted for the nonlocal model with different values of the internal length scale. Similarly to the previous test the curves overlap up to the

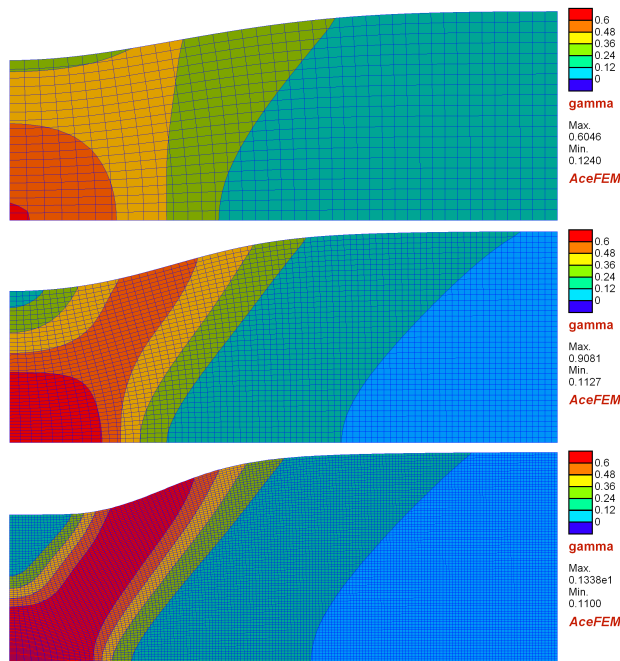


Figure 5.29: Deformed mesh with plastic strain measure γ distribution for mesh 1 (upper), mesh 2 (middle) and mesh 3 (lower) (nonlocal elasto-plasticity with degradation, $l = 0.005$ m, elements without F -bar)

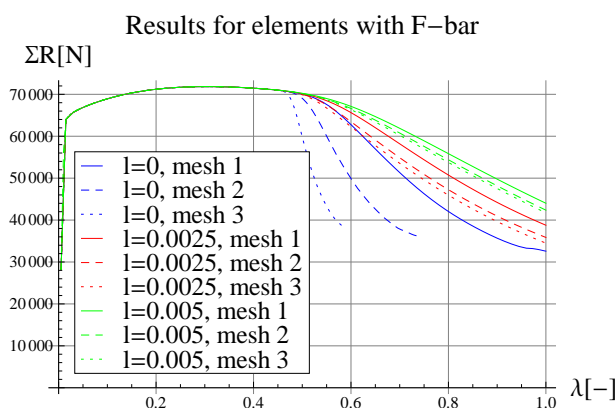


Figure 5.30: Sum of reactions vs displacement multiplier for nonlocal elasto-plasticity with degradation

value of the displacement multiplier equal to $\lambda = 0.48$ and become distinct till the end of the elongation process. However, in this case the internal length has a strong influence on the mesh-sensitivity, for the higher adopted value the diagrams for mesh 2 and mesh 3 are very close, and the diagrams suggest a localized mode of the deformation, which can be confirmed in Figures 5.31 and 5.32 where shear bands are observed. It can be noticed that for $l = 0$ the strains localize in two rows of elements. The application of the gradient enhancement (see Figure 5.32) prevents the results from this pathological mesh-dependence and has a regularizing effect. To sum up, it is interesting that the choice of the type of finite element has such strong influence on the results which differ

not only quantitatively but qualitatively as well.

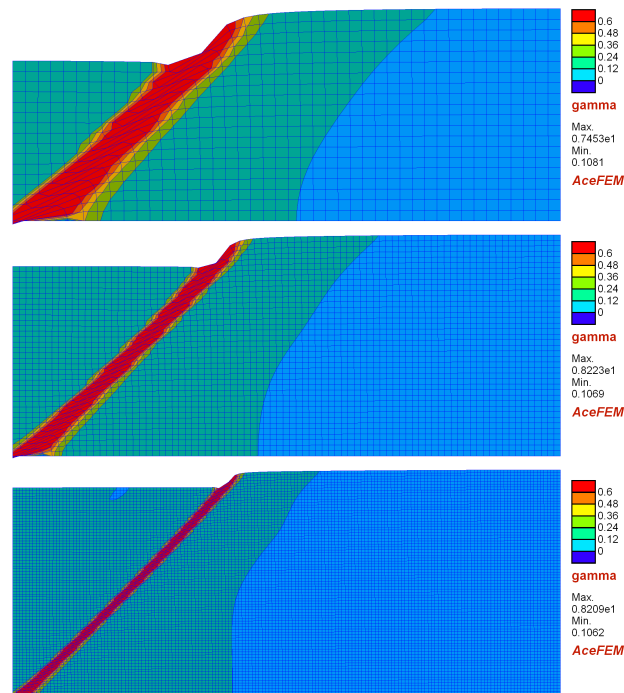


Figure 5.31: Deformed mesh with plastic strain measure γ distribution for mesh 1 (upper), mesh 2 (middle) and mesh 3 (lower) (local elasto-plasticity with degradation, F -bar elements)

Next, the results obtained using the finite elements with and without F -bar modification are compared in Figure 5.33 for the zero internal length scale. The stiffer response of the material simulated with F -bar elements is observed in the post peak regime. For the uniform deformation of the sample before the peak the F -bar modification of finite elements does not affect the results.

The application of F -bar elements causes a softer response of the material model and admits the jump into a localized shear band mode, while the standard finite elements seem to prevent localization and favour the diffuse deformation for sparser meshes. To make the matters worse, the plane strain tests (like 3D ones) are by rule more sensitive to volumetric locking, but in our test the boundary conditions are imposed in that way that globally the plate can extend with the volume preserved. Thus, in this case, it seems that the influence of the isochoric constraint manifests itself rather at the level of shear band formation.

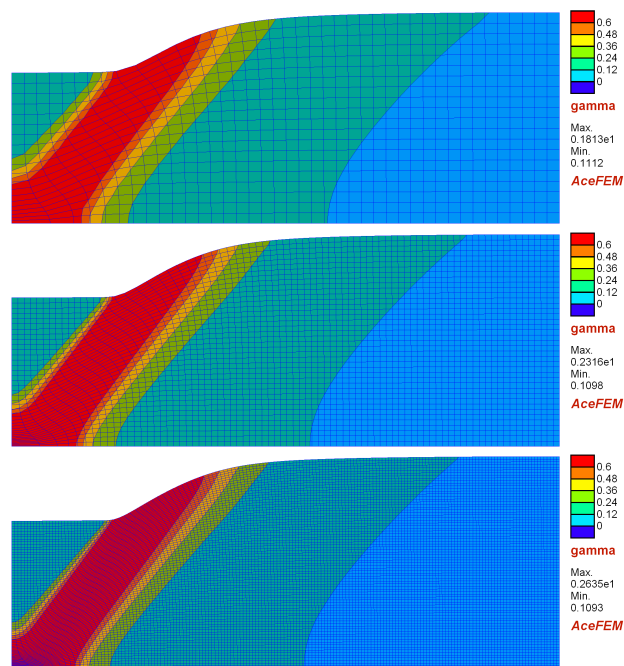


Figure 5.32: Deformed mesh with plastic strain measure γ distribution for mesh 1 (upper), mesh 2 (middle) and mesh 3 (lower) (nonlocal elasto-plasticity with degradation, $l = 0.005$ m, F -bar elements)

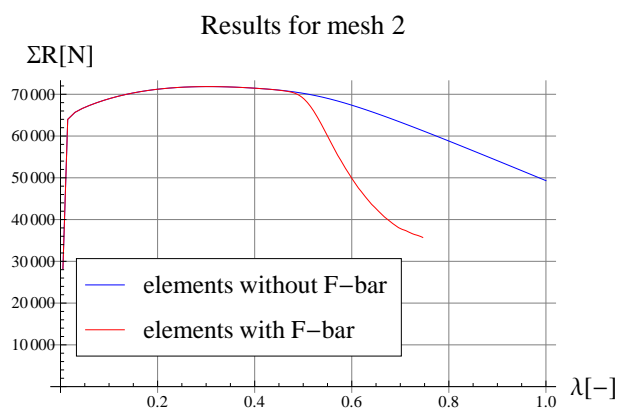


Figure 5.33: Sum of reactions vs displacement multiplier for local elasto-plasticity with degradation

Local thermomechanical model

6.1 General remarks

In this chapter the interest is paid to the development of constitutive descriptions which are able to reproduce the material behaviour in non-isothermal conditions. Unquestionably, the coupling between mechanical and thermal fields in a material is complex and reciprocal. On the one hand, temperature can influence the mechanical response through

- thermal expansion
- dependence of material parameters on it

and, on the other hand, mechanical deformation affects the temperature field in the following ways

- geometry change of a sample influences heat flux (this phenomenon is obviously considered only in the description taking into account geometrical nonlinearities)
- dissipative processes such as plastic deformation can cause heat generation and increase temperature of the material

It is worth mentioning that in the book [Holzapfel, 2000] materials in elastic range are divided into two groups: entropic and energetic. The former group includes amorphous polymers whose internal energy does not change with deformation and the Gough-Joule effect is observed, see [Gough, 1805] and [Joule, 1859]. In simple words, a polymer sample warms up on stretching and, moreover, under constant tensile force it shrinks when heated and expands upon cooling. For the latter group, the energetic materials, the entropy is constant during deformation whereas the internal energy changes. This class of materials includes solids like metals, ceramics or crystals (materials with regular atomic structure).

In this dissertation the attention is focused only on energetic materials, thus thermo-elastic coupling related to the Gough-Joule effect is neglected. Nonetheless, the simulations of entropic materials within symbolic-numerical computation tool *Ace* were also

investigated recently by the author and the results are presented in [Wcisło and Pamin, 2014].

The study of thermo-inelasticity in thermodynamic context is included in among others [Maugin, 1992], [Ristinmaa et al., 2007] and [Egner, 2012]. The description of the large strain thermo-plastic model which is analysed in the thesis is based mainly on [Simo and Miehe, 1992], [Wriggers et al., 1992].

This chapter is limited to the analysis of local models, i.e. no gradient enhancement is incorporated. However, as will be discussed in the following sections, the heat conduction can also introduce regularization into the description and this aspect of strain localization modelling is investigated.

6.2 Description of thermo-elasto-plastic model

6.2.1 Kinematics for non-isothermal problem

When thermomechanical coupling is taken into account the motion of the body is not only a function of a particle and time but it also depends on absolute temperature denoted in the thesis with T

$$\mathbf{x} = \varphi(\mathbf{X}, t, T) \quad (6.1)$$

Consistently, the deformation gradient (2.6) depends also on the temperature and covers, apart from elastic and plastic contributions, the effect of thermal expansion.

To separate these three kinds of deformation the constitutive model is derived using the multiplicative decomposition of the deformation gradient into its thermal, elastic and plastic parts as follows

$$\mathbf{F} = \mathbf{F}^\theta \mathbf{F}^e \mathbf{F}^p \quad (6.2)$$

which is illustrated in Fig. 6.1. The decomposition of the deformation gradient for thermomechanics was discussed in [Stojanović et al., 1964], [Lu and Pister, 1975], [Lubarda, 2004] and [Wcisło and Pamin, 2017].

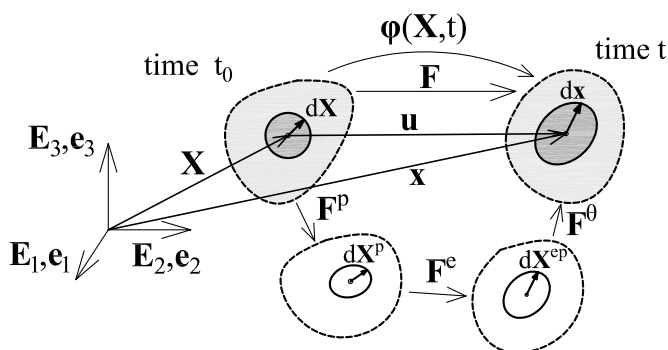


Figure 6.1: Decomposition of deformation gradient for thermo-plasticity

Note that the deformation gradient defined in (6.2) can be equivalently formulated in the following forms, cf. [Ristinmaa et al., 2007] and [Holzapfel, 2000],

$$\mathbf{F} = \mathbf{F}^r \mathbf{F}^p = \mathbf{F}^\theta \mathbf{F}^m, \quad \mathbf{F}^r = \mathbf{F}^\theta \mathbf{F}^e, \quad \mathbf{F}^m = \mathbf{F}^e \mathbf{F}^p \quad (6.3)$$

where \mathbf{F}^r denotes the reversible deformation and \mathbf{F}^m the mechanical one.

The thermal part of the deformation gradient is assumed to be purely volumetric, thus it can be represented in the following way

$$\mathbf{F}^\theta = [J^\theta]^{1/3} \mathbf{I}, \quad J^\theta = \det(\mathbf{F}^\theta) \quad (6.4)$$

where \mathbf{I} is the second order identity tensor and the volumetric deformation caused by the temperature change is determined by

$$J^\theta = e^{3\alpha_T[T-T_0]} \quad (6.5)$$

In Equation (6.5) quantity T_0 denotes the reference temperature (for stress- and strain-free state) and α_T is the coefficient of linear thermal expansion.

On the basis of decomposition (6.2) and assumption (6.5) the mechanical part of the deformation gradient can be derived straightforwardly as

$$\mathbf{F}^m = [\mathbf{F}^\theta]^{-1} \mathbf{F} = e^{-\alpha_T[T-T_0]} \mathbf{F} \quad (6.6)$$

Alternative decompositions of the deformation gradient can also be considered, for instance $\mathbf{F} = \mathbf{F}^e \mathbf{F}^\theta \mathbf{F}^p$ used by [Wriggers et al., 1992]. However, as long as the thermal part of the deformation gradient is a spherical tensor this split is equivalent to the one written in Equation (6.2). The application of decomposition (6.2) implies that the mechanical part of the deformation gradient can easily be separated and the algorithm for isothermal elasto-plasticity presented in Section 5.5.1 can be adopted. It should be noted that in this approach the assumption of volume preserving plasticity is disregarded, contrary to the thermo-plastic models presented in papers of [Wriggers et al., 1992] or [Simo and Miehe, 1992].

6.2.2 Free energy functional for thermomechanical problem

The Helmholtz free energy potential presented in Equation (5.4) is now enriched with thermal contribution ψ^θ

$$\psi(\mathbf{b}^e, \gamma, T) = \psi^e(\mathbf{b}^e) + \psi^p(\gamma) + \psi^\theta(T) \quad (6.7)$$

The elastic part of the free energy functional ψ^e is equivalent to the potential defined for the isothermal description (5.5). The plastic potential ψ^p , including isotropic strain hardening, is defined in Equation (5.6), however it is now assumed that the material parameters describing the plastic behaviour, i.e. σ_{y0} , H_i , $\sigma_{y\infty}$ and δ , can depend on temperature. Actually, the material parameters for elasticity, in particular Young modulus $E = \frac{9KG}{3K+G}$, can also be assumed as temperature-dependent. However, it is shown in the Appendix C that it does not influence the response of material significantly in the considered range of temperature increase (i.e. no external heat sources causing significant heating of samples are applied) and therefore it is neglected in the tests for local and nonlocal thermo-elasto-plasticity.

The specific form of the purely thermal part is assumed following [Simo and Miehe, 1992]

$$\psi^\theta(T) = c \left[[T - T_0] - T \ln \frac{T}{T_0} \right] \quad (6.8)$$

where c denotes the heat capacity at constant deformation, which can be derived as, see e.g. [Simo and Miehe, 1992],

$$c = -T \frac{\partial^2 \psi}{\partial T^2} \quad (6.9)$$

For the adopted form of free energy function (6.8) its value is constant.

On the basis of the second law of thermodynamics the following state functions can be derived: the Kirchhoff stress tensor and hardening function using Equation (5.7) as well as entropy

$$\eta = -\frac{\partial \psi}{\partial T} \quad (6.10)$$

6.2.3 Description of thermo-plasticity

The yield function distinguishing between the elastic and plastic regimes considered in this work has the following form

$$F^p(\boldsymbol{\tau}, \gamma, T) = f(\boldsymbol{\tau}) - \sqrt{2/3} \sigma_y(\gamma, T) \leq 0 \quad (6.11)$$

where yield strength $\sigma_y(\gamma, T)$ takes into account isotropic strain hardening (linear and saturation type) and thermal softening in accordance with the formula

$$\sigma_y(\gamma, T) = \left[\sigma_{y0} + \sqrt{2/3} H_i \gamma + [\sigma_{y\infty} - \sigma_{y0}] \left[1 - e^{-\sqrt{2/3} \delta \gamma} \right] \right] [1 - H_T [T - T_0]] \quad (6.12)$$

Here, the simplest approach to thermal softening is adopted, cf. [Wriggers et al., 1992], i.e. linear relation between temperature and total yield strength with thermal softening modulus H_T . Note that this can also be understood as linear degradation of the following material parameters: σ_{y0} , H_i , $\sigma_{y\infty}$ with increasing temperature. In fact, other options for thermal softening can be considered, for example an arctangent function discussed and tested in [Wcisło, 2016].

For the thermomechanical model the stress measure $f(\boldsymbol{\tau})$ governing the plastic process is the HMH yield function. The associated flow rule and the Kuhn-Tucker conditions are the same as for the isothermal description, see Equations (5.13) and (5.14).

6.2.4 Constitutive model for heat conduction

The constitutive assumption for heat conduction is the classical Fourier law for isotropic materials which is formulated here for the Kirchhoff heat flux vector \mathbf{q}

$$\mathbf{q} = -k \nabla T \quad (6.13)$$

where k is the heat conduction coefficient which, for simplicity, is assumed to be constant. The Kirchhoff heat flux is defined in the current configuration, however, it is referred to the area in the undeformed state (it is the Cauchy heat flux multiplied by J). Thus, ∇T is a spatial gradient whereas the coefficient k is specified in the reference configuration.

6.2.5 Energy balance equation

The energy balance condition, which is the second governing equation next to the linear momentum balance discussed in Section 5.3, is expressed in the following temperature form

$$c\dot{T} = J\operatorname{div}(-\mathbf{q}/J) + \mathcal{R} \quad (6.14)$$

The above form is derived from the basic formulation of conservation of energy in many publications, e.g. [Simo and Miehe, 1992]. In Equation (6.14) quantity \mathcal{R} is a heat source density which in the presented model includes heating due to plastic dissipation adopted in the simplified form, cf. [Wriggers et al., 1992],

$$\mathcal{R} = \sqrt{\frac{2}{3}}\chi\sigma_y\dot{\gamma} \quad (6.15)$$

Parameter χ in Equation (6.15) denotes a dissipation heat factor which is assumed to be constant, cf. [Taylor and Quinney, 1934], however, its value can be computed explicitly on the basis of mechanical dissipation as it is discussed in e.g. [Ristinmaa et al., 2007] and [Bartels et al., 2015].

Equation (6.14) is completed with proper boundary conditions:

$$\begin{aligned} T &= \hat{T} & \text{on} & \partial\mathcal{B}_T \\ \mathbf{q} \cdot \mathbf{n} &= \hat{q} & \text{on} & \varphi(\partial\mathcal{B}_q) \end{aligned} \quad (6.16)$$

where

$$\partial\mathcal{B}_T \cup \partial\mathcal{B}_q = \partial\mathcal{B} \quad \text{and} \quad \partial\mathcal{B}_T \cap \partial\mathcal{B}_q = \emptyset \quad (6.17)$$

Note that similarly to the linear momentum balance presented in Section 5.3, the essential boundary conditions for temperature are referred to the initial undeformed configuration whereas the natural boundary conditions for the heat flux are described in the current configuration.

The weak form of energy balance equation (6.14) is obtained using the standard procedure (multiplication by test function δT , integration over body \mathcal{B} , applying divergence theorem and Neumann boundary conditions,) and backward Euler scheme for time integration. The following integral equation valid for a current time is obtained

$$\int_{\mathcal{B}} \left[\delta T \frac{c}{\Delta t} [T - T_n] + \nabla \delta T k \nabla T - \delta T \mathcal{R} \right] dV + \int_{\varphi(\partial\mathcal{B}_q)} \delta T \hat{q} da = 0 \quad (6.18)$$

where T_n is the value of temperature at the previous time and Δt is the time increment.

6.3 Implementation of local thermomechanical model

Consistently with the computational approach discussed in Section 4.3 the vector of element unknowns for the thermomechanical problem is defined firstly

$$\mathbf{p} = [\mathbf{u}_I, \mathbf{T}_I] \quad (6.19)$$

which includes nodal displacements \mathbf{u}_I and nodal temperatures \mathbf{T}_I . The unknown fields are interpolated using shape functions $\mathbf{N}_{I,u}$ and $\mathbf{N}_{I,T}$

$$\mathbf{d}_{el} = [\mathbf{N}_{I,u}, \mathbf{N}_{I,T}] \cdot [\mathbf{u}_I, \mathbf{T}_I] \quad (6.20)$$

The order of the interpolation in multi-field problems is discussed in many publications. Usually it is suggested to use quadratic functions for displacements and linear for temperature. On the other hand, in paper [Simone et al., 2003], which concerns implicit gradient-enhanced continuum damage models, it is substantiated that linear interpolation of both fields (displacement vector and nonlocal variable) can be used. The provided reasoning can also be applied to the case of thermomechanical coupling, and therefore linear interpolation of temperature and displacements is admissible. In this work the linear shape functions for both fields are used for numerical testing of thermomechanical problems due to lower costs of computations accompanying acceptable quality of the results.

Now, the potentials for the problem are defined. For the balance of linear momentum this is the elastic free energy functional $\psi^e(\mathbf{b}^e)$ from Equation (5.5), as for the isothermal case, and for the energy balance equation (6.14) the following form is proposed

$$\Pi_{en} = \frac{1}{2} \frac{c}{\Delta t} [T - T_n]^2 + \frac{1}{2} k \nabla T \cdot \nabla T - \mathcal{R} T \quad (6.21)$$

it is derived on the basis of the weak form (6.18) in such a way that the variation of Π_{en} is zero. The potential presented in Equation (6.21) is valid provided that quantities k , c and \mathcal{R} are independent of temperature. However, it can be observed that \mathcal{R} which includes plastic heating in accordance with Equation (6.15) does not satisfy this requirement. To solve this problem without changing potential (6.21) an AD exception can be applied to compute of the residual vector. Thereby, the generation of additional terms not present in the original balance equation is avoided and the generated code is numerically efficient.

Now, on the basis of potentials (5.5) and (6.21) the residual vector consisting of two parts can be defined. The first part \mathbf{R}_u is related to the balance of linear momentum and the second \mathbf{R}_{en} to the balance of energy. Introducing the numerical integration, the Gauss point contribution to the residual vector is computed as follows

$$\mathbf{R}_G = [\mathbf{R}_{u,G}, \mathbf{R}_{en,G}], \quad (6.22)$$

where

$$\mathbf{R}_{u,G} = \frac{\partial \psi}{\partial \mathbf{u}_I}, \quad \mathbf{R}_{en,G} = \frac{\partial \Pi_{en}}{\partial \mathbf{T}_I} \Big|_{\frac{D\mathcal{R}}{D\mathbf{T}_I} = \mathbf{0}} \quad (6.23)$$

and condition $\frac{D\mathcal{R}}{D\mathbf{T}_I} = \mathbf{0}$ is the aforementioned AD exception.

It should also be explained how thermal expansion is taken into account in the balance of linear momentum. Potential (6.7) does not include a part responsible for this phenomenon directly, cf. e.g. [Simo and Miehe, 1992]. However, computation of the mechanical part of the deformation gradient from Equation (6.6) results in the dependence of \mathbf{F}^e and \mathbf{b}^e on temperature which is taken into account automatically in the AD process.

Finally, the Gauss point contribution to the tangent matrix \mathbf{K}_G is calculated using relation

$$\mathbf{K}_G = \frac{\partial \mathbf{R}_G}{\partial \mathbf{p}} = \begin{bmatrix} \frac{\partial \mathbf{R}_{u,G}}{\partial \mathbf{u}_I} & \frac{\partial \mathbf{R}_{u,G}}{\partial \mathbf{T}_I} \\ \frac{\partial \mathbf{R}_{en,G}}{\partial \mathbf{u}_I} & \frac{\partial \mathbf{R}_{en,G}}{\partial \mathbf{T}_I} \end{bmatrix} = \begin{bmatrix} \mathbf{K}_{uu} & \mathbf{K}_{uT} \\ \mathbf{K}_{Tu} & \mathbf{K}_{TT} \end{bmatrix} \quad (6.24)$$

For the thermomechanical coupling the element tangent matrix is non-symmetric and can be entirely filled.

The specific solution algorithm for thermo-elasto-plasticity is outlined in Box 5.

Given at element level:

- Current vector of nodal displacements and temperatures $\mathbf{p} = [\mathbf{u}_I, \mathbf{T}_I]$
- Isoparametric interpolation
- Integration point variables at the end of previous step, i.e.: deformation gradient \mathbf{F}_n and its mechanical part \mathbf{F}_n^m elastic left Cauchy-Green tensor \mathbf{b}_n^e , plastic strain measure γ_n , temperature T_n

Compute at each integration point:

1. Current deformation gradient $\mathbf{F} = \mathbf{I} + \frac{\partial \mathbf{u}}{\partial \mathbf{X}}$
2. For F-bar element – go to Box 1
3. Thermal deformation gradient $\mathbf{F}^\theta = e^{\alpha_T(T-T_0)}\mathbf{I}$
4. Mechanical deformation gradient $\mathbf{F}^m = (\mathbf{F}^\theta)^{-1}\mathbf{F}$
5. Relative mechanical deformation gradient: $\mathbf{f} = \mathbf{F}^m(\mathbf{F}_n^m)^{-1}$
6. Final values of \mathbf{b}^e and γ using solution algorithm for isothermal elasto-plasticity according to steps 4-8 from Box 2
7. Elastic free energy function ψ^e (5.5)
8. Heat source \mathcal{R} (6.15)
9. Potential for energy balance Π_{en} (6.21)
10. Gauss point contribution to element residual vector and tangent matrix (6.22) and (6.24)

Box 5. Finite element algorithm for thermo-plasticity at large strains

6.4 Numerical simulations

6.4.1 Simulation of circular bar necking¹

Firstly, the numerical test of a circular bar in tension is investigated. The dimensions of the circular bar are: total length $L = 0.064$ m and radius of cross-section $R = 0.008$ m. The adopted material parameters are presented in Table 6.1. Due to symmetry of the specimen only one eighth of the sample is discretized and examined in *AceFEM* package. The adopted finite element meshes are presented in Figure 6.2. The discretizations are refined near the center of the bar.

The mechanical boundary conditions are assumed in such a way that the symmetry is guaranteed and free transverse deformation is allowed. The enforced displacement is equal to $u_{max} = 0.009$ m and is achieved at time $t_{max} = 9$ s in adaptive steps. On the surface of the bar convective boundary conditions are adopted with parameters presented in Table 6.2. Their implementation within *Ace* package is not trivial and is shortly presented in the Appendix B.

¹This subsection was published in paper: [Wcisło and Pamin, 2017], Copyright ©2016 John Wiley & Sons, Ltd.

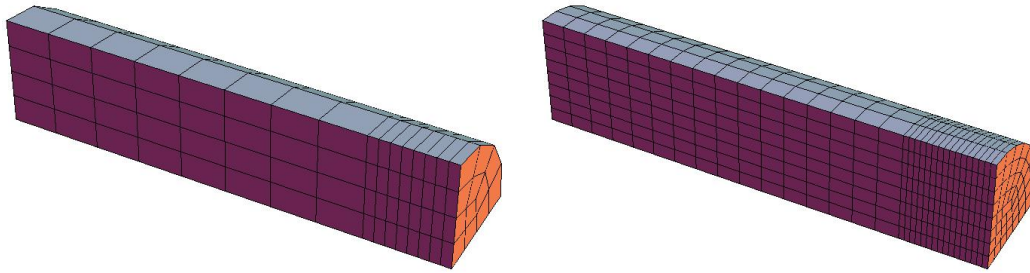


Figure 6.2: Finite element discretizations of one eighth of circular bar : mesh 1 and mesh 2

Property	Symbol	Value	Unit
Bulk modulus	K	$164.2e9$	N/m^2
Shear modulus	G	$80.19e9$	N/m^2
Initial yield stress	σ_{y0}	$0.45e9$	N/m^2
Residual yield stress	$\sigma_{y\infty}$	$0.6e9$	N/m^2
Hardening modulus	H_i	$129e6$	N/m^2
Saturation coefficient	δ	16.93	–
Density	ρ	$7.8e3$	kg/m^3
Conductivity	k	0, 100, 400	$\text{J}/(\text{s K m})$
Heat capacity	c	460	$\text{J}/(\text{kg K})$
Thermal expansion coefficient	α_T	$12e-6$	$1/\text{K}$
Thermal softening modulus	H_T	0.002	$1/\text{K}$
Dissipation heat factor	χ	0.9	–
Reference temperature	T_0	273.15	K

Table 6.1: Material parameters

Property	Symbol	Value	Unit
Temperature of surrounding	T_∞	273.15	K
Convection coefficient	h_{conv}	100	$\text{W}/(\text{m}^2\text{K})$

Table 6.2: Parameters for convection

It can be noticed that the analyzed bar is prismatic and no imperfection is assumed. The only source of disturbance in the specimen is convection over the external surface, which causes non-uniform cooling of the sample and finally determines the location of the neck in the center of the bar.

The elongation of the bar is tested for different values of the heat conduction coefficient (including the adiabatic case $k = 0$) to investigate its influence on the strain localization. The results are also compared to those obtained with the isothermal model. Due to the fact that in the isothermal analysis convection does not determine the location of the neck, the sample with small imperfection in the center of the bar is then considered (it is a reduction of the initial yield stress $\sigma_{y0,imp} = 0.99\sigma_{y0}$ in the volume of one element of mesh 1). The diagram presenting the sum of reactions vs the displacement multiplier

is depicted in Figure 6.3.

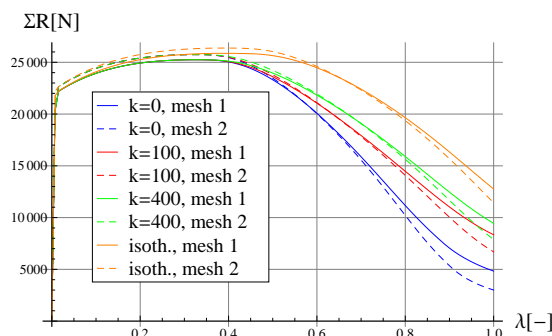


Figure 6.3: Sum of reactions ΣR vs enforced displacement multiplier λ for circular bar in tension, for different values of heat conduction coefficient and discretizations

It can be observed that the results obtained for the isothermal and the adiabatic cases are the limit diagrams and the rest of the outcomes related to the processes with heat conduction are the intermediate cases. Furthermore, the higher the value of k is assumed the more ductile the diagram in the post-peak regime is. This observation confirms that the heat conduction induces regularization effects. We can also notice that just after the peak the diagrams for mesh 1 and mesh 2 for each value of k and the isothermal case are very close up to a certain point and become distinct close to the end of the deformation process. This observation leads to the conclusion that the presented results are not mesh-dependent and the difference in diagrams at the end of the process is a consequence of too coarse mesh in the active deformation zone (lack of the adaptive mesh refinement).

In Figure 6.4 the deformed meshes with the distribution of the plastic strain measure γ for different values of the heat conduction coefficient are presented. It can be observed that there are slight differences between deformations of the localization zone: for a higher value of k the left row of elements in the necking region is less elongated. However, in all analyzed cases the plastic process at the end of the deformation is active only in this row of elements. To assess the width of the active zone (i.e. zone with positive axial displacements) through the whole process the diagrams presented in Figure 6.5 have been prepared. The width is measured along the bar axis in two ways: in the reference and in the deformed configuration. It can be observed that before the peak the whole bar is plastified and later an increasing part of the sample exhibits unloading. It can also be observed that during the elongation process the width of the active zone does not change abruptly and this behaviour is similar for each analyzed case. Finally, for each variant of heat conduction and the isothermal case the localization zone narrows down to the width of one finite element, and this results in the final mesh sensitivity which could be mitigated by the application of the discretization refinement in the necking zone.

Lastly, the influence of heat conduction on the temperature of the bar is examined. The diagrams in Figure 6.6 depict the evolution of temperature on the specimen surface in the center and at the end of the bar. It can be noticed that not only the value of temperature in the active zone (point A) strongly depends on heat conduction but also

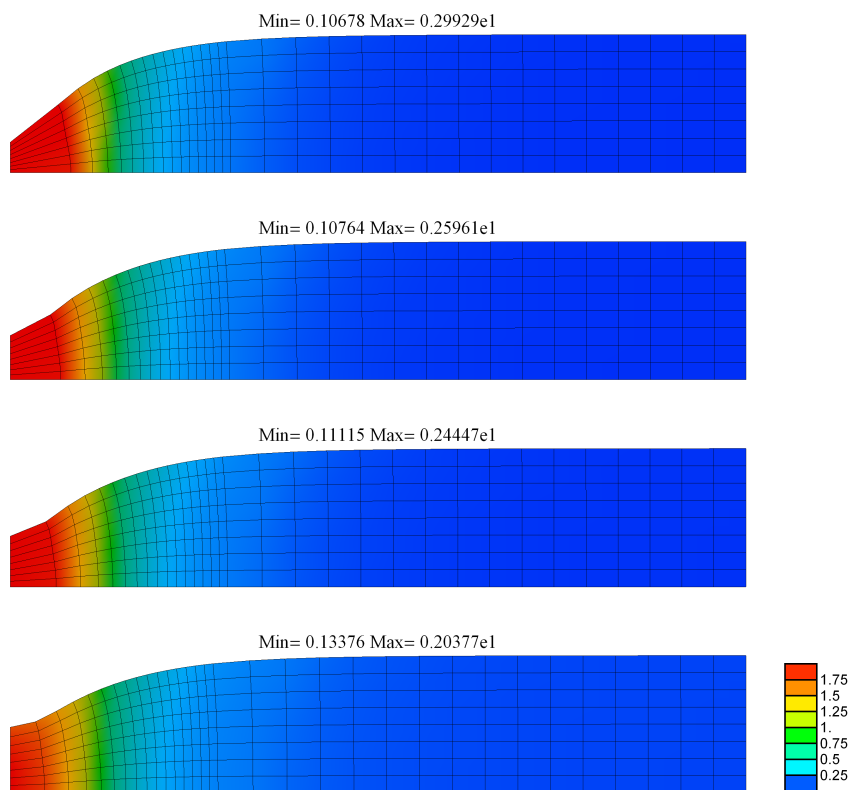


Figure 6.4: Deformed mesh with distribution of plastic strain measure γ for $k = 0$, $k = 100 \text{ J}/(\text{sKm})$, $k = 400 \text{ J}/(\text{sKm})$ and isothermal model

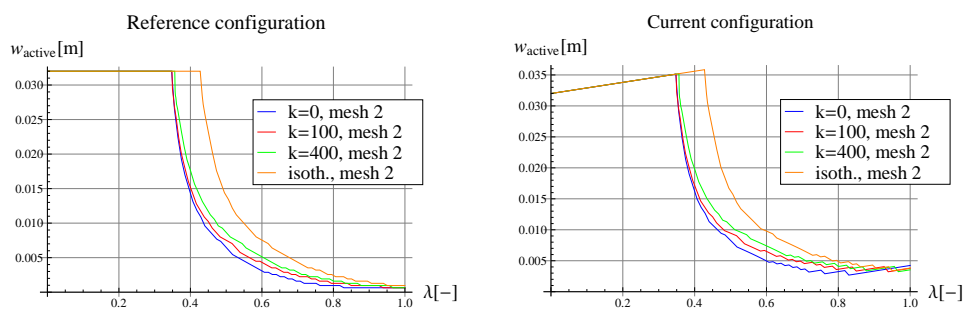


Figure 6.5: Width of zone with positive increments of axial displacement w_{active} vs load multiplier λ . On the left: width of active zone is measured along longitudinal axis in reference configuration, on the right: in current configuration

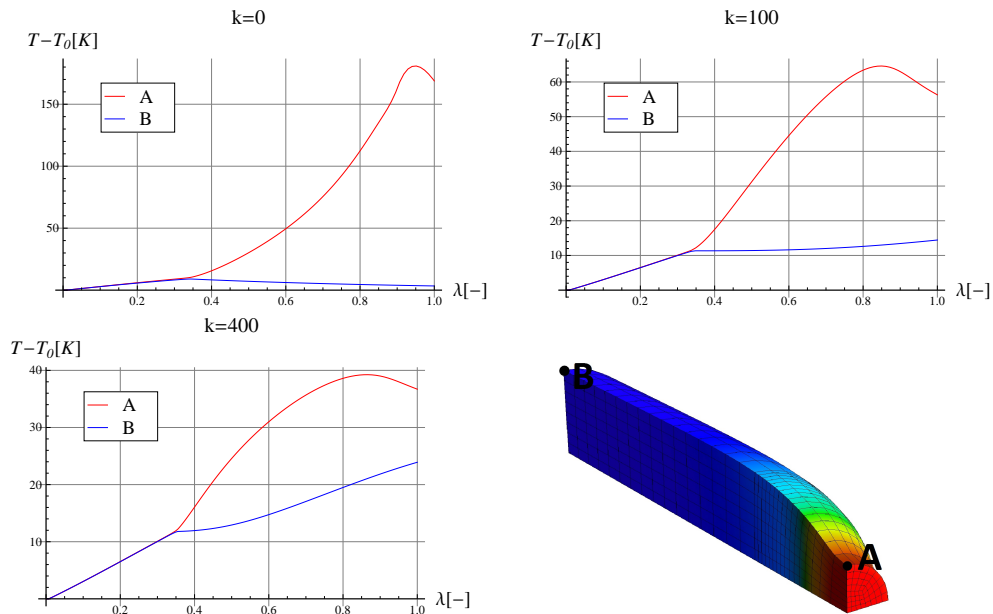


Figure 6.6: Relative temperature $T - T_0$ at points A and B vs displacement multiplier λ for different values of heat conduction coefficient k

the state of material at the end of the bar (point B) which, depending on the value of k , can be heated or even cooled. The influence of convection is also observed in the decreasing diagrams for point A at the end of the elongation process.

6.4.2 Simulation of plate in tension – influence of heat conductivity²

Next, the simulation of a plate in tension is performed. The specimen has the same dimensions as the plate presented in Section 5.6.2 and has a square imperfection in the centre ($L_{imp} = 0.005\text{m}$). The imperfection is assumed as a decrease of the initial yield stress to $\sigma_{y0,imp} = 0.8\sigma_{y0}$ and an increase of thermal softening coefficient to $H_{T,imp} = 1.05H_T$, cf. [LeMonds and Needleman, 1986]. The imperfection in this test is increased for a better computational performance since when a small defect, e.g. 1%, is used, as in the previous simulation, some difficulties with convergence occur at the point of rapid softening in the post peak regime. All material parameters adopted in the simulations are given in Table 6.1 apart from the thermal softening modulus which is now equal to $H_T = 0.02 \text{ K}^{-1}$.

The plain strain conditions are assumed (displacements at all nodes in the thickness direction are restrained) and due to symmetry of the specimen only one quarter of the plate is considered. The remaining mechanical boundary conditions are assumed in such a way that the deformation in the width direction is allowed. The enforced maximum displacement in the length-direction is equal to $u_{max} = 0.04 \text{ m}$ and is achieved after 1 s in adaptive steps. The whole sample is insulated, i.e. homogeneous Neumann boundary conditions for the thermal field are adopted.

The finite element meshes are presented in Figure 6.7. Three discretizations of

²This subsection was published in paper: [Wcisło and Pamin, 2017], Copyright ©2016 John Wiley & Sons, Ltd.

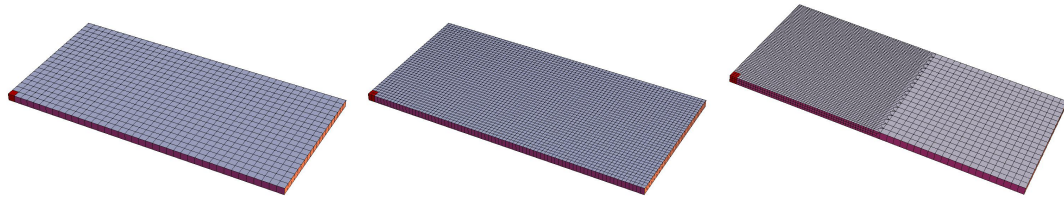


Figure 6.7: Finite element discretizations of plate in tension (mesh 1, mesh 2, and mesh 3, respectively)

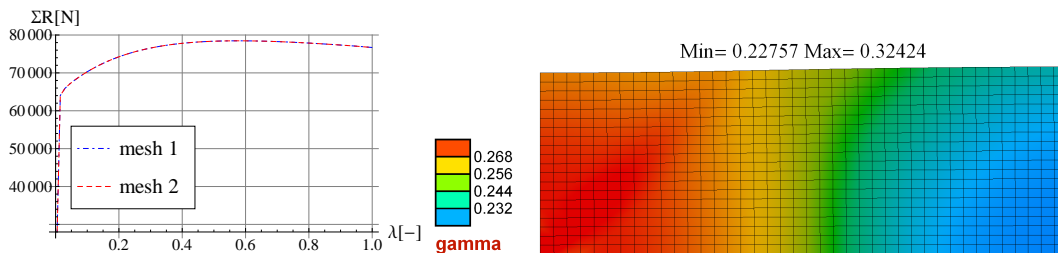


Figure 6.8: Results for isothermal elongation of plate in plane strain (mesh 1): sum of reactions ΣR vs displacement multiplier λ and deformed mesh with plastic strain distribution at the end of elongation

the specimen are considered: coarse (called mesh 1), medium (called mesh 2) and fine (called mesh 3), which consist of 800, 3200 and 11480 elements, respectively.

If the simulation is performed using the isothermal model then softening due to geometrical effects occurs. It can be observed that the force-displacement diagram in Figure 6.8 exhibits a peak and a descending branch. The deformation of the plate at the end of the simulated process is presented in Figure 6.8 and at this stage of elongation the sample begins to neck. The results for elongation of a plate in plane strain regime (elasto-plastic isothermal model) in the form of diffuse necking are also presented in e.g. [Okazawa, 2009] or [Mikkelsen, 1997].

However, if the thermomechanical coupling involving thermal softening is considered then strain localization is observed at the end of elongation in the form of a shear band (see Figure 6.9). Depending on the value of the heat conduction coefficient the widths of the band differ significantly. The differences are also noticed in the diagram presenting the sum of reactions versus the load multiplier in Figure 6.10. Due to high distortion of the finite element mesh in the localization band the majority of computations stop before the maximum displacement reaches value u_{max} . Due to this reason the results in the diagrams are presented for the enforced displacement factor smaller than $\lambda = 0.55$. The outcomes are presented in four diagrams: the first one refers to the finest mesh and different values of the heat conduction coefficient. The sample responses differ significantly for each value of k which indeed exhibits a regularizing effect. The rest of diagrams in Figure 6.10 are prepared to investigate the mesh sensitivity of the results for different values of the conductivity. It can be observed that the higher the value of the heat conduction coefficient is, the closer the results for each discretization are to one another.

To investigate the mesh-sensitivity more precisely and to analyse the width of the

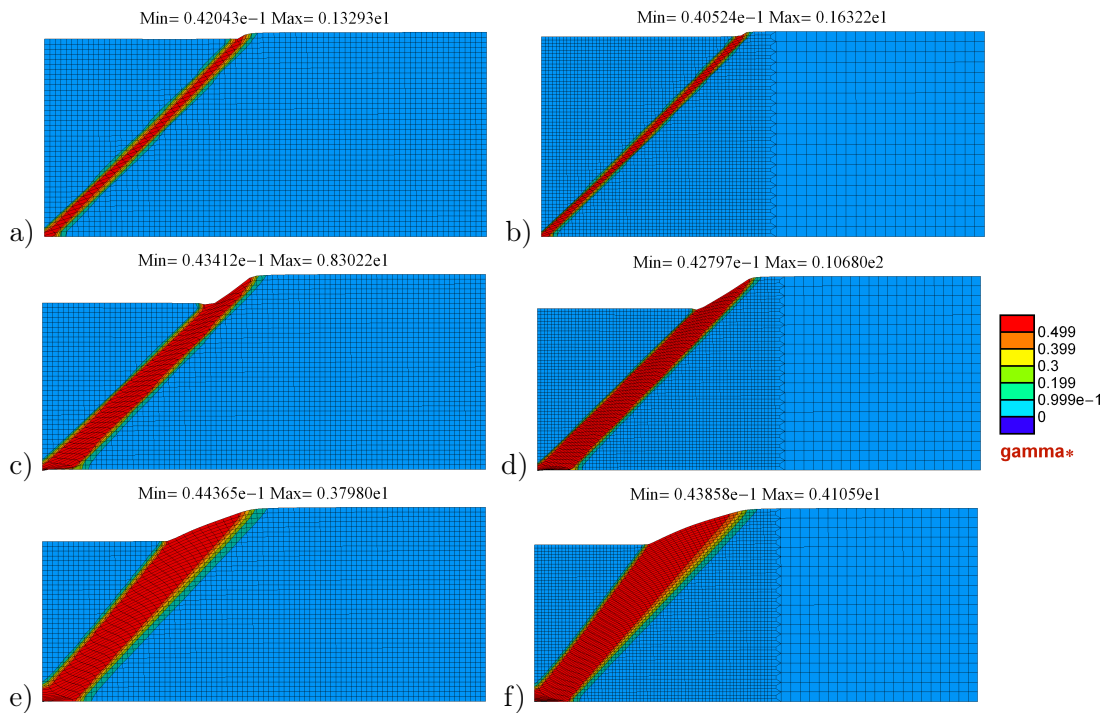


Figure 6.9: Deformed mesh with distribution of γ for $k = 0$, $k = 100 \text{ J}/(\text{sKm})$, $k = 400 \text{ J}/(\text{sKm})$ at the end of elongation process

active zone (i.e. the zone with a positive increment of the plastic strain measure) during elongation, the diagrams in Figure 6.11 have been prepared. The width of the localization zone is measured along a line perpendicular to the band (see line AB drawn in Figure 6.11) in the reference configuration. The first diagram presents the results obtained for the adiabatic case ($k = 0$) and different meshes. It can be observed that the plastic strains localize in bands of different widths for each discretization, which confirms the pathological dependence of the results on the density of the finite element mesh. What is more, the shear band arises abruptly (for mesh 1 and mesh 2 it forms when the enforced displacement multiplier reaches the value $\lambda \approx 0.175$) and does not change up to the end of computations. The second diagram is related to the response of the plate when heat conduction is taken into account ($k = 400 \text{ J}/(\text{sKm})$). If the results for mesh 1 and mesh 2 are analyzed it can be noticed that the formation of the shear bands occurs later than for the adiabatic case (here $\lambda \approx 0.20$). Moreover, the band widths are larger comparing to the bands formed without heat conduction. The widths of the active zones for mesh 2 and mesh 3 are very close to each other and this can be interpreted in such a way that the heat conduction exhibits regularization properties and influences the width of the localization band as already demonstrated in Fig. 6.9.

All calculations are performed using personal computer *Lenovo ThinkPad T430* equipped with *Intel core i7 vPro* processor and 8 GB of RAM memory. For a better assessment of the numerical tool example information for the elongated plate simulated with mesh 2 ($k = 400 \text{ J}/(\text{sKm})$) is presented: number of nodes – 6642, number of degrees of freedom – 19926, total number of iterations – 1520, duration of computations – 8500s.

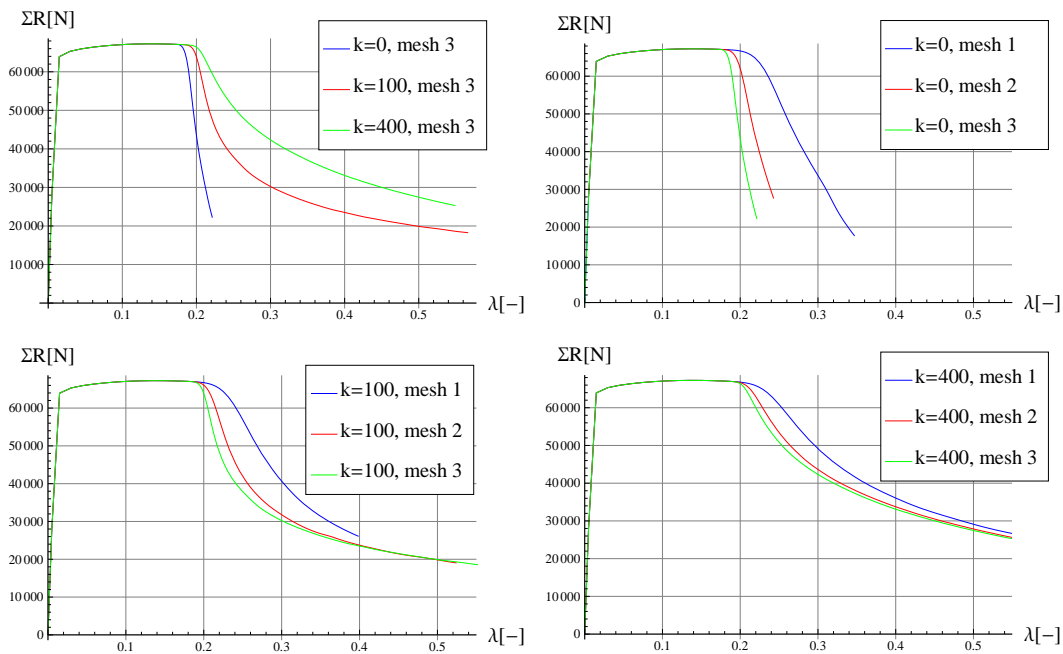


Figure 6.10: Sum of reactions ΣR vs displacement multiplier λ for plate in tension for different values of heat conduction coefficient k and different discretizations

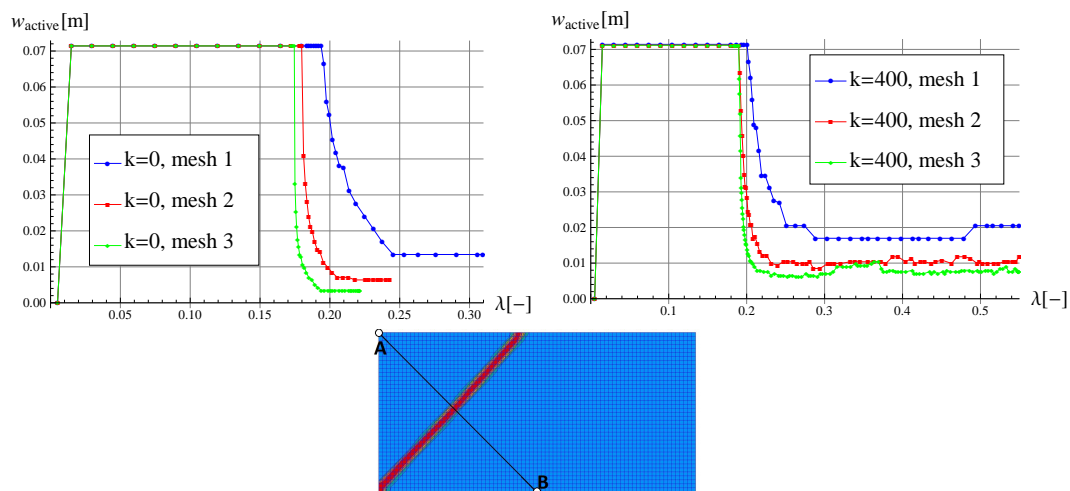


Figure 6.11: Width of active plastic zone w_{active} measured along line A-B in reference configuration vs displacement multiplier λ (mesh 2)

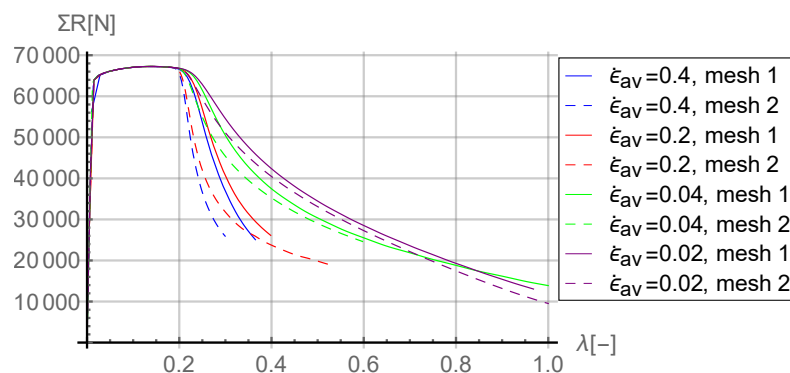


Figure 6.12: Sum of reactions vs enforced displacement multiplier for different duration of deformation process

6.4.3 Simulation of plate in tension – influence of rate of deformation process

As it was discussed in the previous section, heat conduction influences the localization behaviour, however, its regularizing properties depend on time in contrast to standard gradient-enhanced models. In fact, even for a large value of the heat conduction coefficient assumed for a material, the process can be treated as nearly adiabatic for deformation occurring in a very short time.

To investigate the influence of the rate of the deformation process the following experiment is simulated. The rectangular plate with the same material parameters and boundary conditions as in Section 6.4.2 is elongated in different periods of time, in particular, $t = 0.5\text{ s}$, $t = 1\text{ s}$ (results from Section 6.4.2), $t = 5\text{ s}$ and $t = 10\text{ s}$ which correspond to the following averaged strain rates: $\dot{\epsilon}_{av} = 0.4\text{ s}^{-1}$, $\dot{\epsilon}_{av} = 0.2\text{ s}^{-1}$, $\dot{\epsilon}_{av} = 0.04\text{ s}^{-1}$, $\dot{\epsilon}_{av} = 0.02\text{ s}^{-1}$, respectively. The heat conduction coefficient is now equal to $k = 100\text{ J}/(\text{sKm})$, thus, the medium value among those analyzed in the previous Section is chosen. Two discretizations of the plate are considered: mesh 1 and mesh 2, see Figure 6.7.

The load-displacement diagram for the analyzed case is presented in Figure 6.12. It can be observed that the results strongly depend on the rate of the deformation process. For faster processes, i.e. $\dot{\epsilon}_{av} = 0.4\text{ s}^{-1}$ and $\dot{\epsilon}_{av} = 0.2\text{ s}^{-1}$, the post-peak branches descend abruptly and computations stop much before the enforced displacement multiplier reaches the final value $\lambda = 1$. Moreover, the results for mesh 1 and mesh 2 differ significantly. On the other hand, for slower processes, i.e. $\dot{\epsilon}_{av} = 0.04\text{ s}^{-1}$ and $\dot{\epsilon}_{av} = 0.02\text{ s}^{-1}$, the response of the material is more ductile and almost mesh-independent.

The deformed meshes at the end of the elongation for the fastest and the slowest processes are shown in Figure 6.13. In the upper picture the shear band covers only two rows of elements, thus, it involves the possibly smallest volume of localization. In the lower picture the shear band is wide and the form of the final deformation can be classified as necking.

Equation (6.14) with the backward Euler scheme for time differentiation of temper-

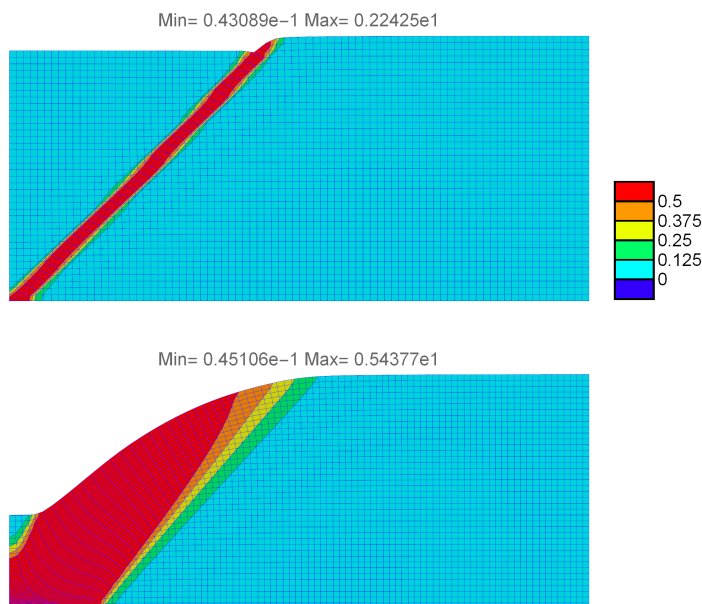


Figure 6.13: Deformed mesh 2 with plastic strain measure distribution for $t = 0.5$ s (upper) and $t = 10$ s (lower) at the end of elongation process

ature is now rewritten

$$\mathcal{R} = c \frac{T - T_n}{\Delta t} + J \operatorname{div}(\mathbf{q}/J) \quad (6.25)$$

When analyzing the energy balance equation it can be concluded that the increasing rate of deformation causes faster heat generation during the plastic process. That heat is balanced by the capacity and conduction parts, see Equation (6.25). If the heat capacity term does not change the conduction term must increase as well.

Next, a comparison of the following two cases is performed:

- elongation of the plate with averaged rate of deformation $\dot{\epsilon}_{av} = 0.2 \text{ s}^{-1}$ and the heat conduction coefficient equal to $k = 400 \text{ J}/(\text{sKm})$
- elongation of the same specimen with $\dot{\epsilon}_{av} = 0.05 \text{ s}^{-1}$ assuming conductivity $k = 100 \text{ J}/(\text{sKm})$

Thus, two processes are considered: in the first one the elongation of the plate is faster and a large value of the heat conduction coefficient is assumed, and in the second case both the coefficient and the averaged rate of deformation are divided by 4 (this results in a slower process with smaller conductivity). The relation between the sum of reactions and the enforced displacement multiplier for the analyzed cases is presented in Figure 6.14. It can be noticed that the diagrams coincide. Thus, the process performed faster but with higher conductivity gives the same response as slower deformation with smaller value of the heat conduction coefficient. It can be noted that in the performed analysis the value of the heat capacity c is assumed to be constant. In fact, its changes also influence the stabilizing effect introduced by conductivity.

To conclude this discussion, it is clear that heat conduction possesses the regularization property which is admittedly time-dependent. The response of the material is

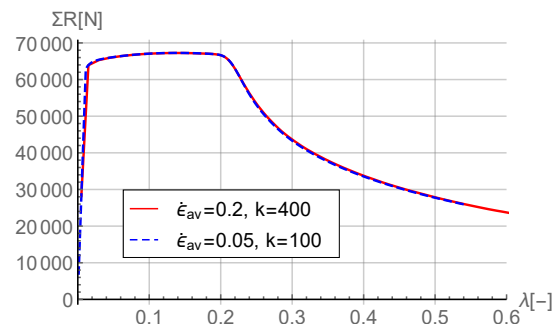


Figure 6.14: Sum of reactions vs load multiplier for different values of conductivity k and durations of elongation process (results for mesh 2)

properly regularized by the conductivity only if the deformation process is sufficiently slow.

It should be mentioned that the effect of the time-dependent regularization can be introduced into a material model through viscous terms, see e.g. [Sluys, 1992], for example into plasticity constitutive equations. For a viscoplastic material the faster the process of the deformation is the more regularized response is obtained. Here, the effect of time-dependence is opposite: with the increasing rate of deformation heat conductivity ceases to stabilize strain localization.

Nonlocal thermomechanical models

7.1 Introduction

In the previous chapter the thermo-elasto-plasticity model is described, implemented and tested using the finite element method. In that model, temperature influences the yield strength introducing another softening source, next to the geometrical effects. The only regularization used in the model is heat conduction whose properties are tested using numerical experiments and compared to the results obtained for adiabatic case ($k=0$). Now, description with additional gradient regularization is considered. In particular, two models are taken into account in this dissertation.

Firstly, a thermomechanical model involving averaged temperature which governs thermal softening is proposed. In this model the attention is focused on the regularization of thermal softening but using an approach alternative to heat conduction. The application of the presented method is indispensable in two cases: when the internal length results from the nonlocality and not from the thermomechanical coupling (in result the predicted shear band width related to heat conduction can be wrong), and when adiabatic conditions or small conduction are assumed.

Secondly, a thermo-elasto-plasticity model with gradient degradation is considered. In this case, the material and thermal softening simultaneously reduce the yield strength, but now a nonlocal variable governs mechanical degradation.

The common feature of both models is the way of incorporation of nonlocality into the description – the implicit gradient averaging discussed in Section 5.2. Due to that fact the implementation of the two models has a very similar framework.

In both cases, the internal adiabatic conditions are first assumed to investigate the regularizing properties of gradient averaging. Subsequently, the simultaneous application of the gradient enhancement and heat conduction in the models is analyzed, which can simulate an evolving shear band.

7.2 Description of nonlocal models

7.2.1 Model with temperature averaging

In this section¹ a nonlocal approach to the coupled thermo-plasticity description is considered. The inspiration for the introduced gradient averaging comes from [Eringen, 1967] who postulated that the material description can be enhanced using higher order gradients of not only the mechanical fields but also temperature. In the presented local model softening is caused by temperature increase thus the regularization of this field seems to be advisable.

The concept is to incorporate higher order temperature gradients into the constitutive description of a material with thermal softening, i.e. to apply a nonlocal variable z which is identified with the averaged field of relative temperature $T - T_0$. The nonlocal variable z will now govern the change of the yield stress in the following way

$$\sigma_y(\gamma, z) = (\sigma_{y0} + H_i\gamma + (\sigma_{y\infty} - \sigma_{y0})(1 - e^{-\delta\gamma}))(1 - H_T z) \quad (7.1)$$

We assume that the averaging of temperature increment affects only the plastic process and has only indirect influence on the thermal energy balance. Nevertheless, the influence of higher order temperature gradients on the energy balance or thermal conduction is an issue to be considered, see [Aifantis, 1992, Müller and Ruggeri, 1993, Forest and Aifantis, 2010].

The variable z can be determined using an additional partial differential equation imposing so-called implicit averaging presented in Section 5.2 which now has the form

$$z - l^2 \nabla_0^2 z = T - T_0 \quad (7.2)$$

with homogeneous Neumann boundary conditions and internal length scale l specified in reference configuration. In the following analysis both material and spatial averaging is tested, however, only the results for material averaging are presented in the work (thus gradients are calculated with respect to the Lagrange coordinates and the internal length scale is related to the undeformed configuration). For the presented numerical simulations the differences in results between those two kinds of averaging are small and coarse meshes give better results for the material averaging than for the spatial one.

7.2.2 Thermomechanical extension of nonlocal elasto-plasticity with degradation

The isothermal description of the finite strain elasto-plasticity accounting for degradation presented in Section 5.1.4 with gradient enhancement discussed in Section 5.2 is now extended to full thermomechanical coupling².

¹The model described in this section was published in paper [Weisło and Pamin, 2017], Copyright ©2016 John Wiley & Sons, Ltd.

²This model was presented in paper [Pamin et al., 2017] published by Mathematical Sciences Publishers

Alternatively, the model can be described on a basis of thermo-elasto-plasticity model introduced in Section 6.2 – for that model an additional source of softening, i.e. degradation of yield strength, with appropriate gradient averaging is now taken into account. Thus, the yield function which now includes thermal and material softening has the following form

$$F^p(\boldsymbol{\tau}, \gamma, T) = f(\boldsymbol{\tau}) - \sqrt{2/3}\sigma_y(\gamma, T)[1 - \omega^p(\bar{\kappa}^p)] \leq 0 \quad (7.3)$$

where yield strength $\sigma_y(\gamma, T)$ representing both strain hardening and thermal softening has the form written in Equation (6.12) and repeated below

$$\sigma_y(\gamma, T) = \left[\sigma_{y0} + \sqrt{2/3}H_i\gamma + [\sigma_{y\infty} - \sigma_{y0}] \left[1 - e^{-\sqrt{2/3}\delta\gamma} \right] \right] [1 - H_T[T - T_0]]$$

where damage-like variable ω^p is computed using Equation (5.24) for the nonlocal value of history parameter κ^p . According to Section 5.1.4 it is assumed that $\kappa^p = \sqrt{2/3}\gamma$.

7.3 Implementation of nonlocal thermomechanical models

For the gradient-dependent thermomechanical problem the vector of element unknowns includes displacements, temperature and nonlocal variable

$$\mathbf{p} = [\mathbf{u}_I, \mathbf{T}_I, \mathbf{z}_I] \quad (7.4)$$

Accordingly, three governing equations are required, all of them are discussed in the previous sections: the balance of linear momentum and averaging equation in Section 5.3 and energy balance in temperature form in Section 6.2.5.

Now, the vector of Gauss point contribution to the residual vector is defined as follows

$$\mathbf{R}_G = [\mathbf{R}_{u,G}, \mathbf{R}_{en,G}, \mathbf{R}_{z,G}] \quad (7.5)$$

where:

$$\mathbf{R}_{u,G} = \frac{\partial \psi^e}{\partial \mathbf{u}_I}, \quad \mathbf{R}_{en,G} = \frac{\partial \Pi_{en}}{\partial \mathbf{T}_I}, \quad \mathbf{R}_{z,G} = \frac{\partial \Pi_z}{\partial \mathbf{z}_I}$$

and the Gauss point contribution to the tangent matrix consists of nine submatrices

$$\mathbf{K}_G = \begin{pmatrix} \frac{\partial \mathbf{R}_{u,G}}{\partial \mathbf{u}_I} & \frac{\partial \mathbf{R}_{u,G}}{\partial \mathbf{T}_I} & \frac{\partial \mathbf{R}_{u,G}}{\partial \mathbf{z}_I} \\ \frac{\partial \mathbf{R}_{en,G}}{\partial \mathbf{u}_I} & \frac{\partial \mathbf{R}_{en,G}}{\partial \mathbf{T}_I} & \frac{\partial \mathbf{R}_{en,G}}{\partial \mathbf{z}_I} \\ \frac{\partial \mathbf{R}_{z,G}}{\partial \mathbf{u}_I} & \frac{\partial \mathbf{R}_{z,G}}{\partial \mathbf{T}_I} & \frac{\partial \mathbf{R}_{z,G}}{\partial \mathbf{z}_I} \end{pmatrix} = \begin{pmatrix} \mathbf{K}_{uu} & \mathbf{K}_{uT} & \mathbf{K}_{uz} \\ \mathbf{K}_{Tu} & \mathbf{K}_{TT} & \mathbf{K}_{Tz} \\ \mathbf{K}_{zu} & \mathbf{K}_{zT} & \mathbf{K}_{zz} \end{pmatrix}$$

which, in general, can all be non-zero. Thus, the problem is indeed highly nonlinear and the derivation of the tangent matrix analytically is practically infeasible.

7.4 Numerical simulations

7.4.1 Thermo-elasto-plasticity with temperature averaging

The thermomechanical model with gradient averaging of temperature is tested with the same benchmarks as the local description in Section 6.4, i.e. elongation of circular

bar and rectangular plate in plane strain conditions. Thus, first necking of the circular bar in tension is considered and secondly shear banding in the tensioned rectangular plate in plane strain conditions is analysed. All simulations are performed using F -bar elements.

Simulation of circular bar necking³

The configuration of the test is presented in Section 6.4.1. The elongation of the sample without heat conduction is considered ($k = 0$) and the influence of the adopted internal length scale on simulation results is investigated ($l \in \{0\text{m}, 0.002\text{m}, 0.004\text{m}, 0.008\text{m}\}$). In Figure 7.1 the sum of reactions versus enforced displacement multiplier is presented. For the increasing internal length scale the diagram descends slower in the post-peak regime. This confirms the regularizing effect of the applied averaging in the absence of heat conduction in the sample. Comparing the diagrams in Figure 6.3 with Figure 7.1 the response of the sample is similar for increasing heat conduction and increasing internal length scale.

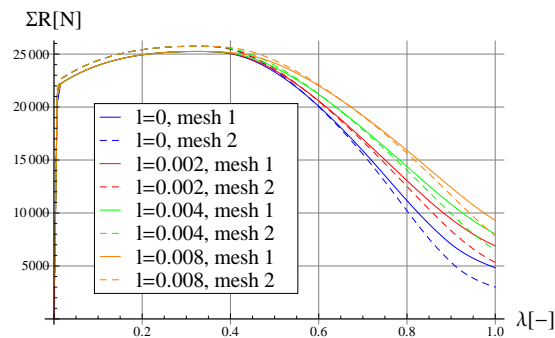


Figure 7.1: Sum of reactions ΣR vs enforced displacement multiplier λ for circular bar in tension for different of internal length scale and discretizations

The deformations of the sample at the end of elongation for the different values of the internal length scale differ slightly and are very similar to the deformation obtained with the local model, presented in Figure 6.4.

In Figure 7.2 the deformed fine mesh is presented with local and nonlocal relative temperature distributions at the end of the elongation. It can be observed that the second picture indeed presents smoothed temperature field depicted in the first picture. Cooling of the bar surface caused by convection does not influence significantly the nonlocal temperature field and the averaged temperature has smaller values in the necking zone than the local one, which can be noticed in the diagrams in Figure 7.3.

Analogously to the analysis of bar necking modelled with the local description the width of the active zone is also investigated. It turns out that the character of necking formation is the same as in the local model: the active zone narrows slowly depending on the adopted internal length scale and finally the plastic process takes place in one row of elements. The diagrams presenting the relation between the width of the plastic

³This subsection was published in paper: [Wcisło and Pamin, 2017], Copyright ©2016 John Wiley & Sons, Ltd.

zone and the displacement multiplier, obtained for the gradient model, are very close to those presented in Figure 6.5 and due to this fact they are not presented here.

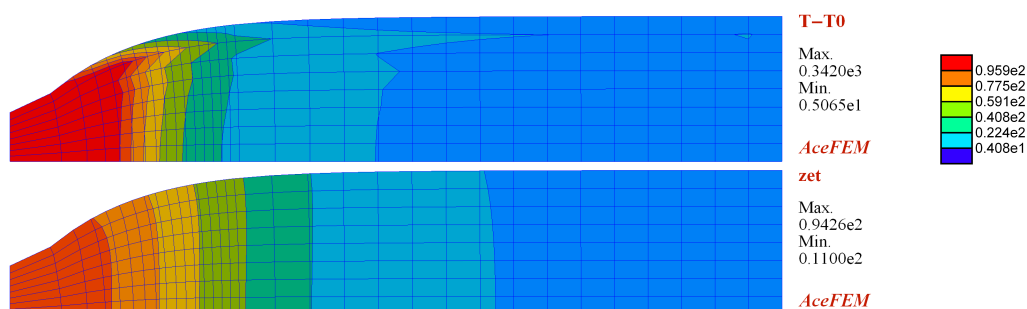


Figure 7.2: Deformed mesh with distribution of relative temperature (upper) and non-local variable (lower) at the end of deformation for $k = 0$ and $l = 0.004$ m

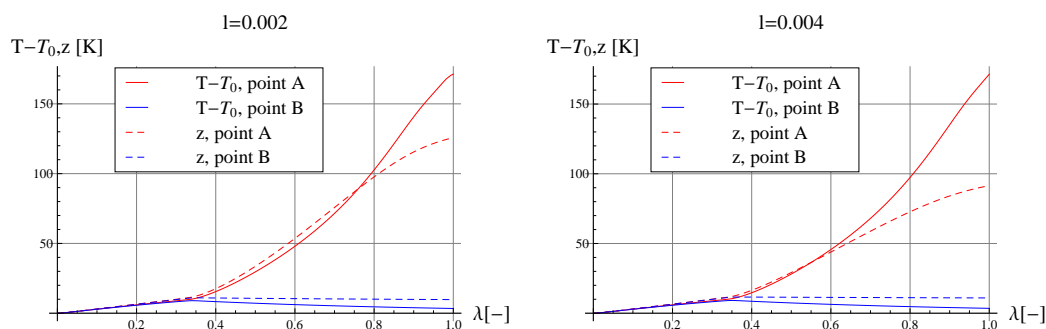


Figure 7.3: Evolution of local and nonlocal relative temperature at points A and B (see Figure 6.6) for different values of internal length scales

Simulation of plate in tension⁴

The test is defined in Section 6.4.2. The adiabatic case is first analyzed ($k = 0$) for different values of the internal length scale $l \in \{0 \text{ m}, 0.0025 \text{ m}, 0.005 \text{ m}, 0.01 \text{ m}\}$.

In Figure 7.4 the relation between the sum of reactions and the enforced displacement multiplier is presented. In this simulation the internal length scale significantly influences the ductile behaviour of the sample. Furthermore, the larger the internal length is assumed the smaller mesh-dependence of the results is observed.

In Figure 7.5 the deformed meshes with the distribution of the local or nonlocal relative temperature are presented. The width of the localization band strongly depends on the assumed value of the internal length scale and this parameter also strongly influences the distribution of the averaged relative temperature field. For a better investigation of the shear band formation the diagram of the width of the active zone is depicted in Figure 7.6. Depending on the adopted internal length the widths of shear bands differ. What is more, the internal length scale influences the onset of localization and the moment of band formation.

⁴This subsection was published in paper: [Wcisło and Pamin, 2017], Copyright ©2016 John Wiley & Sons, Ltd.

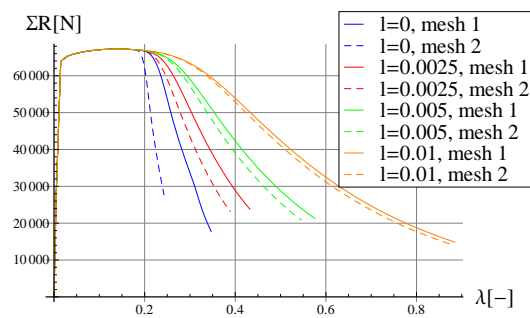


Figure 7.4: Sum of reactions vs enforced displacement multiplier for plate in tension (plain strain) for different values of internal length scales and discretizations

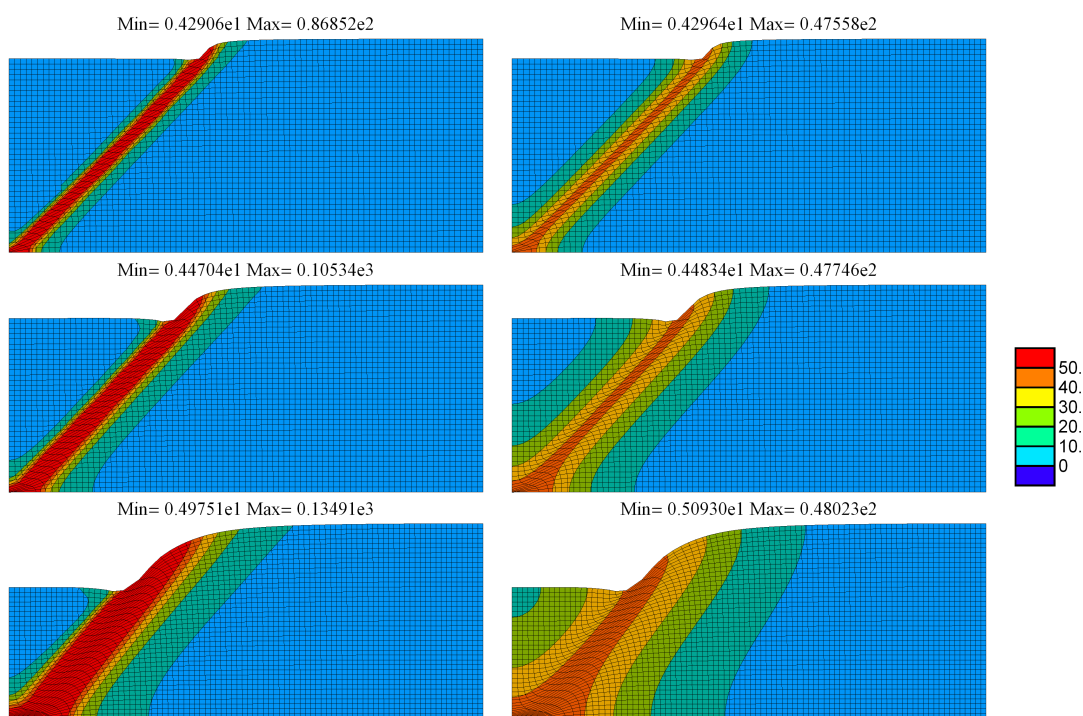


Figure 7.5: Deformed mesh with distribution of local and nonlocal relative temperature (mesh 2) for $l = 0.0025$ m (upper), $l = 0.005$ m (middle) and $l = 0.01$ m (lower) at the end of elongation process

Finally, the interaction of the two investigated length scales governing the behaviour of the thermo-plastic material is examined. The heat conductivity is assumed to be $k = 100$ J/(sKm) which for the local model gives deformation as in Figure 6.9c and the internal length scale for temperature averaging is now equal to $l = 0.0025$ m which in the adiabatic case is related to the response presented in the first drawing in Figure 7.5. The simulations for this data set are performed using three meshes and the results are presented in Figures 7.7 and 7.8. In the diagram presenting the sum of reactions versus the enforced displacement multiplier the results for the current test are compared to the outcomes of the simulations with only one active internal scale: either k or l . It can

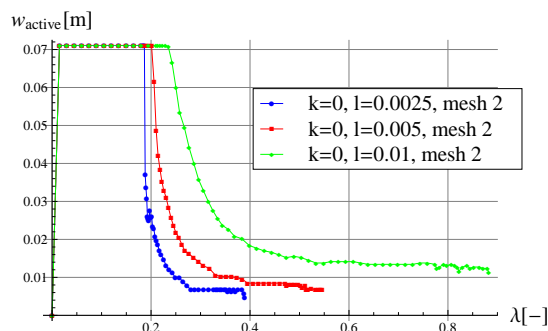


Figure 7.6: Width of active plastic zone w_{active} measured along line A-B (see Figure 6.11) in reference configuration vs displacement multiplier λ (mesh 2)

be noticed that although the application of one regularization (either heat conduction or spatial temperature gradients) leads to strongly localized diagonal shear band, the introduction of two scales changes strongly the sample response. Firstly, the ductility of the material is significantly greater and, secondly, the post-peak diagram does not descend monotonically – changing rate of softening is observed during elongation. However, the diagrams obtained for mesh 2 and mesh 3 are very close to each other. Thus the adopted internal length scales efficiently prevent the results from mesh-sensitivity.

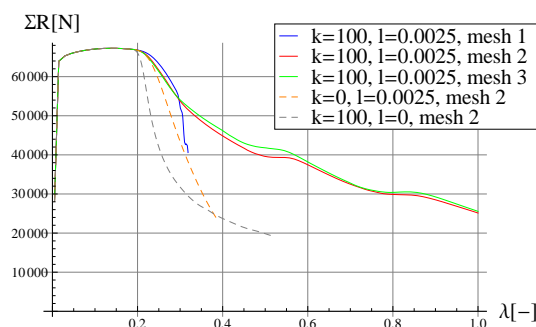


Figure 7.7: Sum of reactions vs enforced displacement multiplier for plate in tension for $k = 100 \text{ J}/(\text{sKm})$, $l = 0.0025 \text{ m}$ and different discretizations

Due to the non-zero thermal conductivity heat flows from the initial localization band in which temperature significantly rises with the plastic dissipation. This flow in combination with temperature averaging causes the expansion of the band and its translation which can be observed in Figures 7.8 and 7.9.

It should be mentioned here that the phenomena of instabilities which propagate through the sample can be observed in experiments, for example in metals: Lüders bands caused by rehardening phenomena or Portevin-Le Chatelier bands which are a result of negative strain-rate sensitivity (see e.g. [de Borst, 2001]). However, the mechanical modelling of those phenomena is performed in the dynamic context. Moreover, the static analysis of shear band saturation in one-dimensional simple cases for static elasticity with non-convex energy and two-dimensional elasto-plasticity at small strain is performed in [Bigoni, 2012]. The author emphasizes the difficulty of three-dimensional

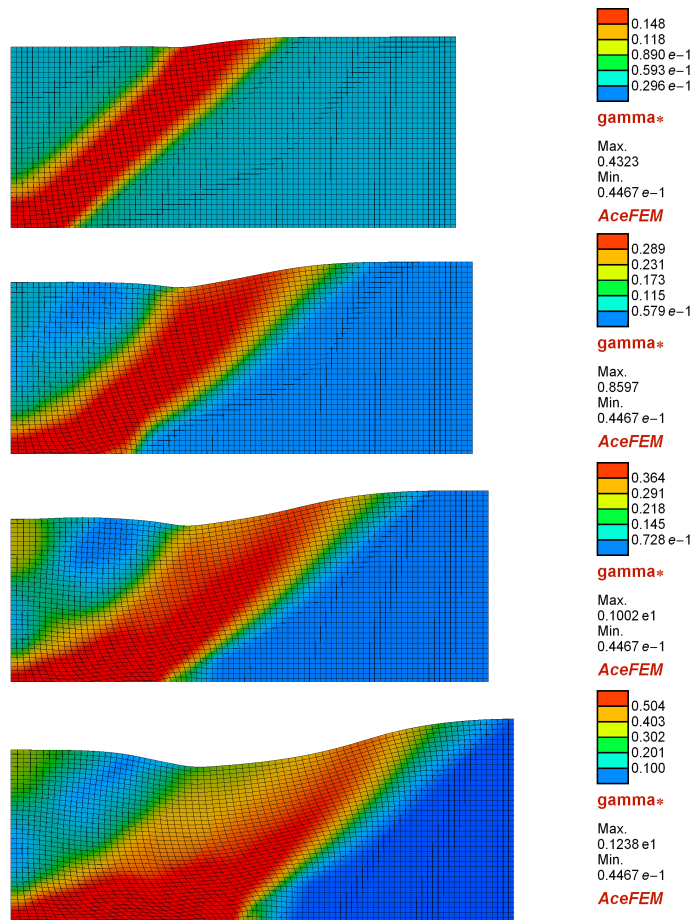


Figure 7.8: Deformed mesh with distribution of plastic strain measure at different stages of elongation process (mesh 2)

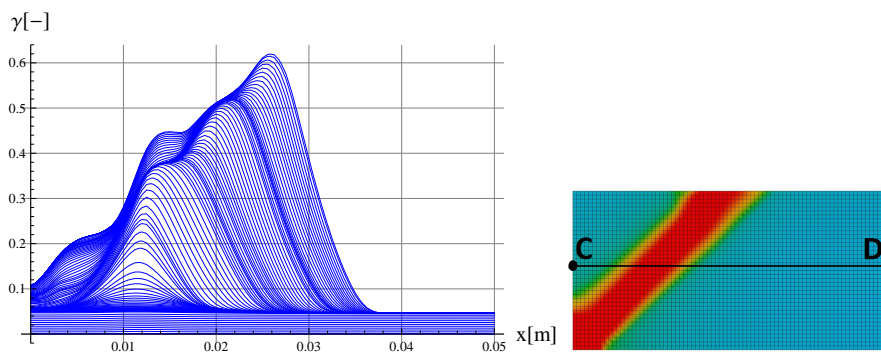


Figure 7.9: Evolution of plastic strain measure γ along line CD in reference configuration

elasto-plastic analysis of localization including large deformations.

7.4.2 Nonlocal thermo-elasto-plasticity with degradation

In this Section the gradient-enhanced thermo-elasto-plastic model with degradation of the yield strength is tested using a benchmark of the elongated rectangular plate in

plane strain conditions presented in Section 6.4.2 with material properties introduced in Table 6.1.

Firstly, the finite elements without F -bar are used for simulations. Due to the fact that in the isothermal case the diffuse mode was obtained and this deformation pattern (with very small differences) is also observed for the thermomechanical coupling with different values of conductivity k and internal length l listed in Table 6.1, the results for one value of the internal length $l = 0.005$ m are only discussed.

Secondly, the F -bar elements are tested. Here more cases are studied: at the beginning the influence of heat conduction is tested for the model with zero internal length scale, next the effect of the internal parameter for the adiabatic case is examined, and finally the simulations are performed with two regularization effects (heat conduction and gradient averaging) included simultaneously.

For this coupled thermomechanical model the whole sample is insulated, i.e. homogeneous Neumann boundary conditions are adopted on the whole surface.

Finite elements without F-bar

The results obtained for the finite elements without F -bar are presented in Figures 7.10 and 7.11. The former presents the load-displacement paths for the nonlocal model with the internal length equal to $l = 0.005$ m for three cases: isothermal, adiabatic $k = 0$ and heat conduction $k = 100$ J/(sKm). The differences between these diagrams are minor but the outcome for mesh 1 is stiffer than for the finer mesh. For the coarse mesh the diagrams for the adiabatic case and heat conduction coincide (red and green solid lines) thus the influence of heat conduction is negligible. Also for the finer mesh that difference is insignificant.

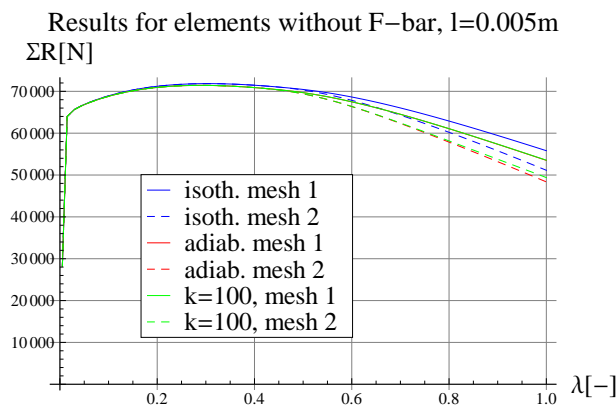


Figure 7.10: Sum of reactions vs displacement multiplier

In Figure 7.11 the deformed mesh with temperature distribution is presented. It can be observed that the presence of thermal softening does not influence the form of deformation and the differences in temperature are also small.

F -bar finite elements

Firstly, the results are compared for zero internal length and different values of heat conduction to confirm that conductivity has a regularizing effect in the absence of

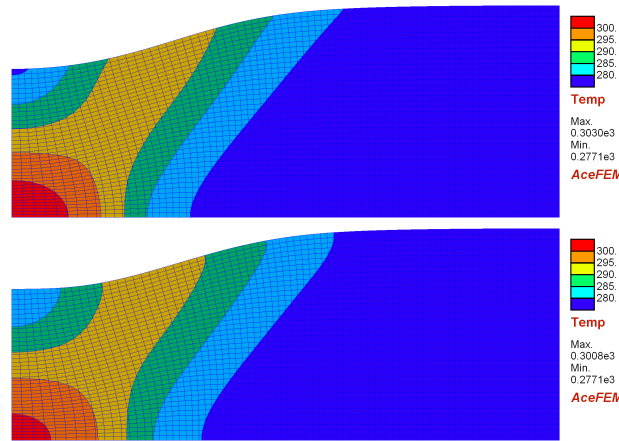


Figure 7.11: Deformed mesh with temperature distribution for $k = 0$ (upper) and $k = 100 \text{ J}/(\text{sKm})$ (lower) – elements without $F\text{-bar}$, $l = 0.005 \text{ m}$, mesh 2

another length scale. The diagrams showing the sum of reactions vs enforced load multiplier for the analyzed cases are presented in Figure 7.12. It can be observed that the diagrams for heat conduction for the coarse mesh are very close to the adiabatic case although some fluctuations are observed. Further, the response of the material with heat conduction is analyzed with the finer mesh. Just after the peak point the response is close to the adiabatic case, however, a convex curve is observed further.

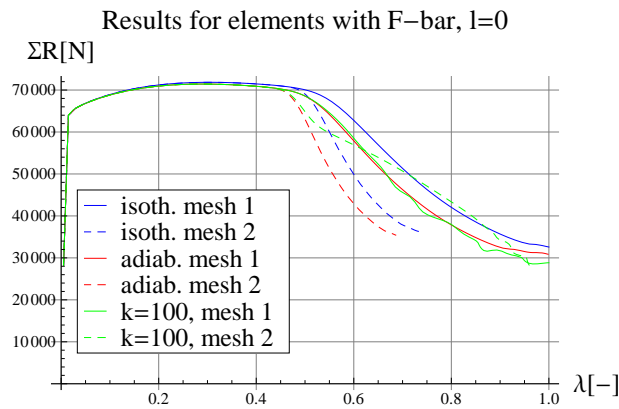


Figure 7.12: Sum of reactions vs displacement multiplier

In Figures 7.13 and 7.14 the deformed meshes with temperature distributions at the end of the elongation process are presented for the adiabatic case and heat conduction, respectively. As it was expected, in the first case in which no regularization is applied the deformation is strongly localized and mesh-dependent. The generated shear band is inclined 45 degrees with respect to the longitudinal axis. However, if heat conduction is taken into account, see Figure 7.14, the shear band is wider but also bent. The deformations for the two considered discretizations differ slightly but have the same character – curved shear band, narrowing in the middle of the modelled sample. When the evolution of the plastic strain measure is investigated along a line perpendicular to the initial shear band for mesh 2 it turns out that the shear band moves slightly, see

Figure 7.15. In the first diagram we can observe a stationary shear band whereas for the case with heat conduction an evolving localization zone.

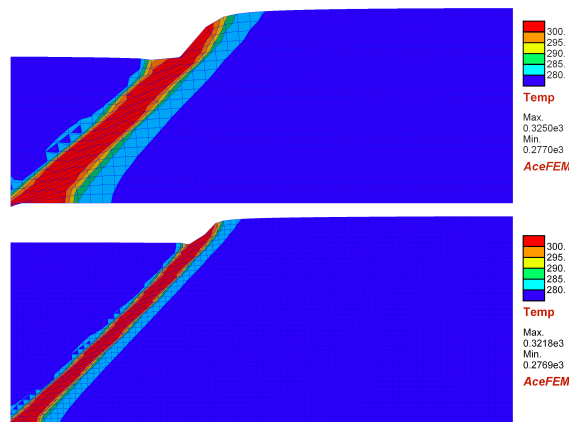


Figure 7.13: Deformed mesh with temperature distribution for mesh 1 (upper) and mesh 2 (lower) – F -bar elements, $k = 0$, $l = 0$

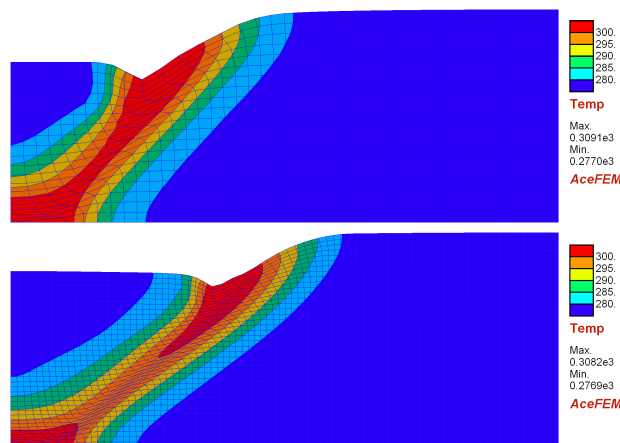


Figure 7.14: Deformed mesh with temperature distribution for mesh 1 (upper) and mesh 2 (lower) – F -bar elements, $k = 100 \text{ J}/(\text{sKm})$, $l = 0$

Now the influence of the internal length parameter is examined for the adiabatic case to verify the regularizing effect of the gradient averaging in the absence of heat conduction. In Figure 7.16 the load-displacement diagrams are presented for zero internal length scale and for $l = 0.005 \text{ m}$. The results for isothermal variant are also presented for comparison. It can be noticed that the addition of thermal softening indeed causes a less stiff response of the material, however its influence is stronger for the model without averaging. The diagrams related to the model with regularization are very close for each mesh and show higher ductility.

In Figure 7.17 the deformed meshes with temperature distribution are presented. The response of the sample is very similar to the isothermal deformation. The shear band has constant width and the solution does not depend on the adopted mesh.

When the results for the two regularizations (heat conduction and gradient averaging) are compared it can be stated that, although both of them influence the

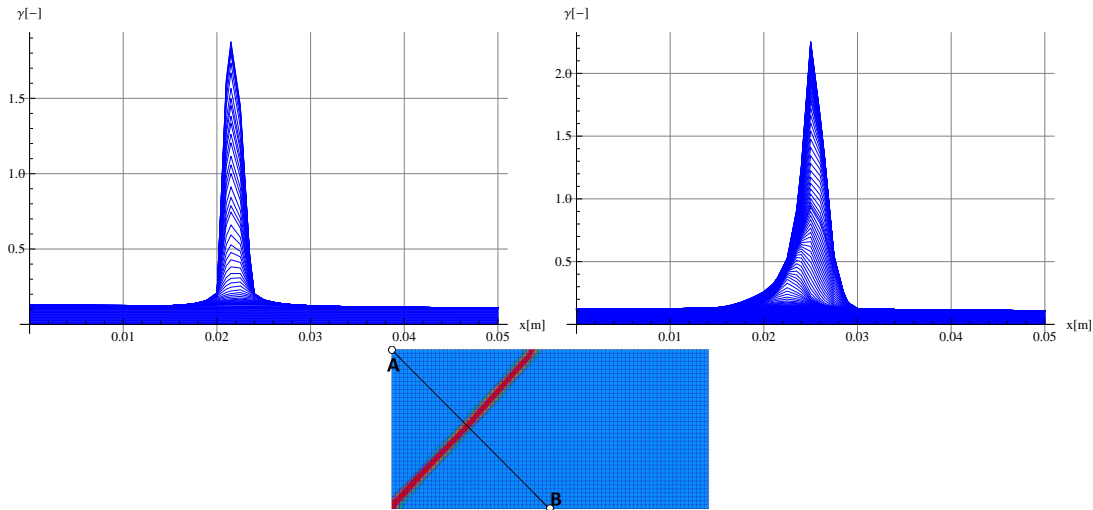


Figure 7.15: Evolution of plastic strain measure γ along line A-B in reference configuration for $k = 0$ (on the left) and $k = 100 \text{ J}/(\text{sKm})$ (on the right) – F -bar elements, $l = 0$

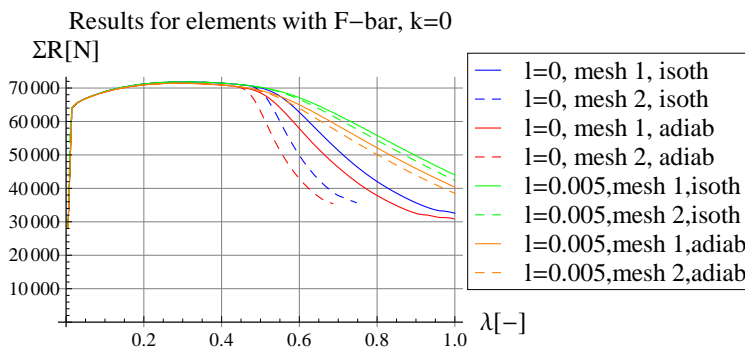


Figure 7.16: Sum of reactions vs displacement multiplier

discretization-dependence and increase the ductility of the response, there are differences in the shape of the localization zone – the internal parameter l visibly governs the width of the band whereas for heat conduction the band has not a regular form (exhibits variable width and curved shape).

Finally, the results of the test performed for heat conduction and gradient averaging active simultaneously are discussed. In Figure 7.18 the force-displacement diagram is presented in which the results for two regularizations acting together (red lines) are compared with the previous results involving only one internal length. It can be observed that the outcome is close to the response obtained for the model with gradient averaging. In this test the results for mesh 1 also exhibit fluctuations which are not noticed for the finer discretization. The material modelled with gradient averaging gives a slightly softer response for mesh 2 than the model with two non-zero scales (i.e. $l = 0.005 \text{ m}$ and $k = 100 \text{ J}/(\text{sKm})$). In Figure 7.19 the deformations of the sample for two discretizations are depicted. The results are very close for both meshes and it can be observed that the shear band width is governed by the internal length scale but it is also bent due to

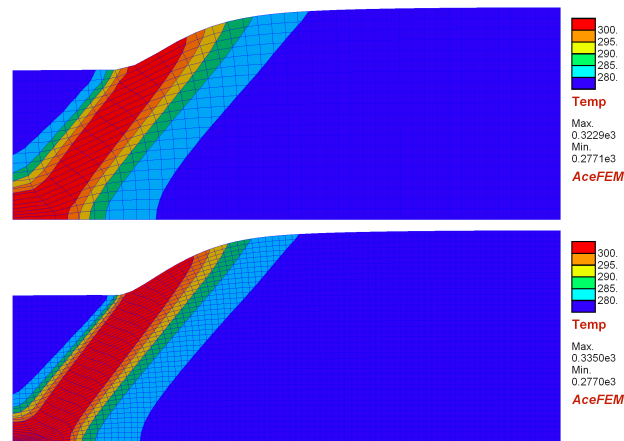


Figure 7.17: Deformed mesh with temperature distribution for mesh 1 (upper) and mesh 2 (lower) – F -bar elements, $k = 0$, $l = 0.005$ m

heat conduction. When the diagram presented in Figure 7.20 is analyzed, it turns out that the band also evolves.

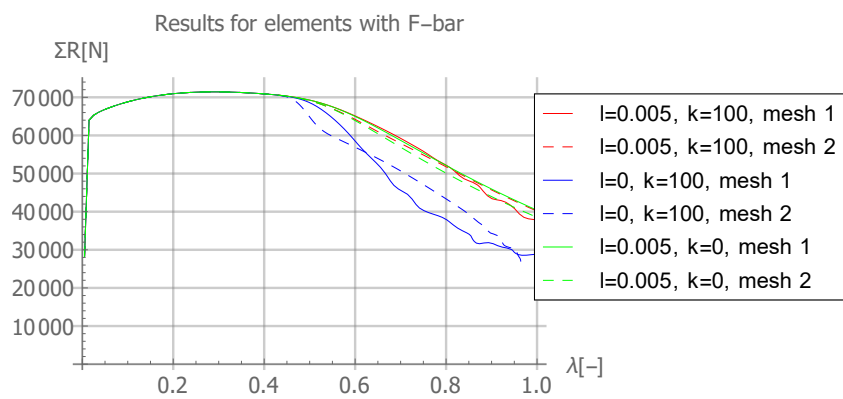


Figure 7.18: Sum of reactions vs displacement multiplier for $k = 100$ J/(sKm) and $l = 0.005$ m compared to results for models with one regularization

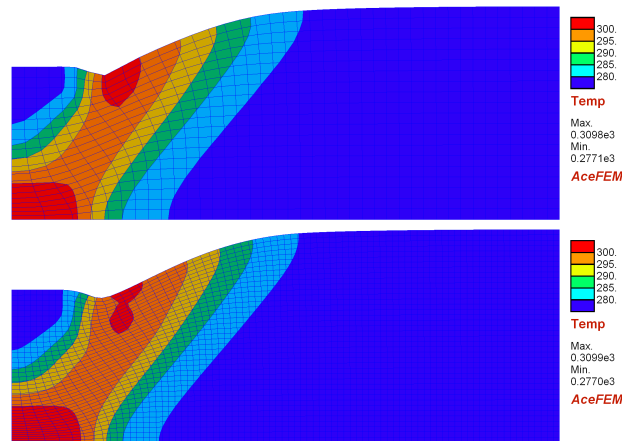


Figure 7.19: Deformed mesh with temperature distribution for mesh 1 (upper) and mesh 2 (lower) – F -bar elements, $k = 100 \text{ J}/(\text{sKm})$, $l = 0.005 \text{ m}$

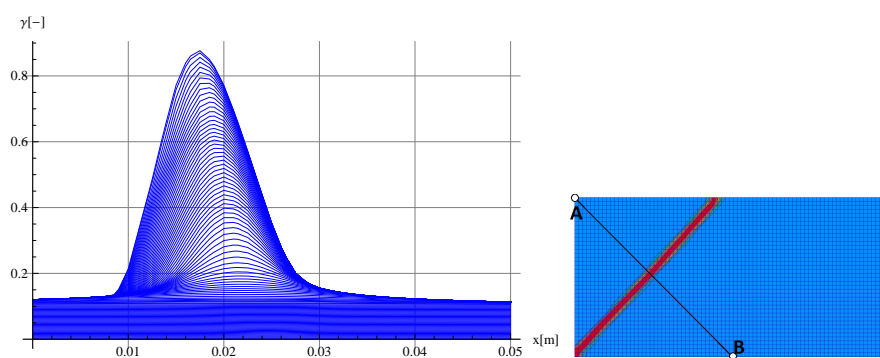


Figure 7.20: Evolution of plastic strain measure γ along line A-B in reference configuration for $k = 100 \text{ J}/(\text{sKm})$ and $l = 0.005 \text{ m}$ (F -bar elements)

Final remarks

8.1 Summary and conclusion

The dissertation deals with the development and numerical testing of inelastic large strain material models in isothermal and non-isothermal conditions with special attention paid to simulation of instabilities. The implicit gradient enhancement, which introduces an internal length scale, is applied for the analyzed descriptions in different variants.

After introductory chapters including fundamentals of large strain problem (Chapter 2), presentation of applied symbolic-numerical tools (Chapter 4) and discussion on types of instabilities (Chapter 3) the specific material models are described and numerically verified.

In Chapter 5 the isothermal models are analyzed. In particular, two nonlocal models are taken into account: elasto-plasticity coupled with damage and elasto-plasticity accounting for degradation of the yield strength. The former model is tested using elongated bar with rectangular variable cross-section and perforated plate in tension. The presented numerical results show that the standard eight-noded hexahedral elements cannot properly reproduce plasticity due to volumetric locking. The problem can be solved using elements with higher-order approximation or by a proper modification of standard elements, for example the *F-bar* approach. Both possibilities have been considered in this case and it turns out that both are able to simulate a plastic process successfully.

Since a comprehensive analysis of the configuration selection for gradient averaging seems to be missing in the literature (apart from the publication of [Steinmann, 1999]), this issue is examined in the work. The numerical results reveal that the averaging performed in the current configuration does not fully prevent the results from the pathological mesh sensitivity as opposed to material averaging. This situation is caused by the change of element size during localization whereas the internal length parameter is assumed to have a constant value in the current configuration during the whole deformation process. Thus, to properly reproduce strain localization with spatial averaging an adaptive mesh refinement should be implemented.

The problem of the choice of a deformation measure governing damage has also

been analyzed. Two different measures have been taken into account and tested using different specimens. It turns out that the selection of the deformation measure can strongly influence the results for the elastic model coupled with gradient damage. Consequently, the application of a proper measure which can correctly represent the behaviour of a real material is an important aspect of constitutive modelling. The investigation of the gradient-enhanced elasto-plasticity with damage for different yield functions (HMH and BDP) reveals that for the applied volumetric strain measure which governs damage the results are significantly different. For the HMH model the range of damage growth is limited, thus, the response of the sample is stiffer. It can be concluded that not only the strain measure should be consciously selected but the choice of the yield criterion is equally important. The latter model, gradient-enhanced elasto-plasticity with degradation, is tested for the rectangular plate with imperfection in plane strain conditions. In this case, for which shear bands are observed, the analysis is carried out for different meshes, finite elements and values of the internal length scale. Although the volume-preserving plasticity is implemented the results do not differ for the finite elements with and without F -bar modification in the plastic regime prior to strain localization. However, for the simulations with the finite elements without F -bar the response in the post peak range has a diffuse form, practically independent of the internal length scale, whereas the F -bar elements simulate strong localization of strains in a shear band. In the latter case the gradient averaging significantly influences the ductility of the material response and prevents the mesh-dependence. In this case, the choice of finite elements affects the results not only quantitatively but qualitatively (different modes of deformation, diffuse or localized, are observed). The incorporation of finite element modification to avoid volumetric locking influences strongly the post-peak behaviour of the material, and its absence can make the localized form of deformation impossible.

Chapter 6 deals with the local thermomechanical model. In this part of work the fully coupled finite thermo-plasticity has been presented and the numerical tests, focused mainly on the regularizing effect of heat conduction, have been performed. The simulations reveal that in the case of a circular bar, in which deformation localizes in a neck, the heat conduction does not change the deformation mode. However, it influences the ductility of the response. If a shear band which is formed in a plane strain plate in tension is analyzed, the regularizing properties of heat conduction are significant. Not only the reaction-displacement relation is influenced by the heat conductivity but also the width of localization band, and, from the numerical point of view, the mesh-independence of the results is noticed. The second aspect of regularization due to heat conduction, which should not be omitted, is the rate of the deformation process. The numerical simulations confirmed that the rate of elongation significantly influences the response of the material. For fast processes softer and mesh-dependent results are obtained, for which the shear band width depends on the adopted mesh. What is more, the increased value of the heat conduction coefficient gives a response close to the material with smaller conductivity but deformed slower.

Having the outcome for the local model and the influence of heat conduction on the results in mind, the thermo-plasticity with gradient-enhanced description has been examined in Chapter 7 using the same benchmarks (circular bar in tension and elong-

ated plate in plane strain regime). Firstly, a novel nonlocal model is presented which incorporates averaging of relative temperature that influences thermal softening. This model provides the length scale which determines the localization zone width and stabilizes the deformation behaviour in the post-peak regime. The first part of simulations have been performed assuming adiabatic conditions ($k = 0$) and different length scales governing the temperature averaging. The results of simulations reveal the expected stabilizing properties of the nonlocality, which in fact regularizes the behaviour of the softening material. In comparison with the local model with different values of the heat conduction coefficient, the global response of the samples appears to be similar, although the temperature distribution can differ significantly for those two models.

An interesting result is also obtained for the case when the heat conduction is incorporated in the nonlocal model. The simulation reveals an evolving shear band for which not only the width increases but also the extreme translates.

The second gradient-enhanced thermomechanical model discussed in the dissertation is thermo-elasto-plasticity coupled with gradient degradation. The response of the tensioned plate in plane strain regime modelled with the *F-bar* elements exhibits the localized form of deformation, strongly discretization-dependent in the absence of regularization. The application of gradient averaging of history variable governing the degradation of the yield strength (related to the plastic strain measure) influences the shear band width whereas the heat conduction produces an irregular and evolving localization zone (with a variable width and a curved shape). Thus, although both the heat conduction and gradient averaging have regularizing properties, they affect deformation in different manners. The simultaneous presence of heat conduction and gradient regularization results in a combination of these two effects.

In the end, the significance of the programming environment applied for the numerical treatment of the complex model is worth emphasizing again. The package AceGen, involving automatic differentiation, is a convenient tool which allows researchers to focus on the model development and on its examination instead of analytical derivation and programming. However, the symbolic-numerical approach requires one to develop proper algorithms which, in the case of efficient code, can involve potentials related to the governing equations. The application of such software to problems of continuum mechanics is relatively new, and due to that reason a lot of attention is paid to the approach and particular algorithms in the dissertation.

8.2 Prospects of future work

The research presented in the dissertation will be continued and there are a few directions that can be undertaken in the future:

- Analyses of other forms of gradient enhancement incorporated in material theories, for example models based on gradient plasticity. Moreover, there is also a possibility to introduce higher order gradients of thermal quantities in the energy balance equation or to analyse a non-Fourier constitutive relation for the heat flux.
- Consideration of exact contribution coming from dissipation in the energy balance

equation instead of the simplified Taylor-Quinney approach, see [Ristinmaa et al., 2007].

- Dropping the isotropy assumption which is an inadequate limitation for modelling of for instance composites.
- Extension of the thermomechanical description to the fully time-dependent problem with viscoplasticity and inertial effects taken into account. Also, visco-elastic model for polymers can be considered.
- Implementation of material models described with one joint potential functional related to both the balance of linear momentum and the conservation of energy, see e.g. [Yang et al., 2006].
- Investigation of ellipticity conditions for thermomechanical and gradient-enhanced material models.
- Development of additional numerical procedures for symbolic-numerical tools, in particular, programming of adaptive refinement of the discretization.

Appendix A

F-bar approach for plane strain problem

In this work all material models are implemented using three-dimensional finite elements. Such elements are the most general and due to that reason different configurations can be tested including plane strain (e.g. elongated plate in Section 5.6.1) or axisymmetric problems (e.g. elongated circular bar in Section 6.4.1). The former case is achieved by the restraint of displacements in the direction normal to the analysis plane (additional essential boundary conditions are defined).

As it was mentioned in Section 5.4.2, to prevent volumetric locking for large strain volume-preserving plasticity the *F-bar* technique [de Souza Neto et al., 2008] can be applied. However, it should be noted that this modification of the deformation gradient might cause spurious non-zero strains in the direction normal to analysis plane, even though the related displacements are constrained to be zero. If in a simulation the finite element does not deform uniformly and the determinant of the deformation gradient computed at the centroid of the element differs from the determinant of the deformation gradient at the analysed Gauss point, then the component \bar{F}_{33} is no longer equal to 1, as it should be for the plane strain state.

To investigate how strongly the non-zero strains influence the results for the plane strain problem simulated with three-dimensional *F-bar* elements (called further *F-bar 3D*) the results are compared to the response obtained for genuine 2D formulation using the appropriate *F-bar* element (called further *F-bar 2D*). For such element the modified deformation gradient at the analysed Gauss point has the form [de Souza Neto et al., 2008]

$$\bar{\mathbf{F}} = \begin{bmatrix} \bar{F}_{11} & \bar{F}_{12} & 0 \\ \bar{F}_{21} & \bar{F}_{22} & 0 \\ 0 & 0 & 1 \end{bmatrix} \quad (8.1)$$

For the in-plane deformation gradient component \mathbf{F}_p defined as follows

$$\mathbf{F}_p = \begin{bmatrix} F_{11} & F_{12} \\ F_{21} & F_{22} \end{bmatrix} \quad (8.2)$$

the individual coefficients of the deformation gradient are computed using the formula

$$\bar{F}_{ij} = \left(\frac{\det \mathbf{F}_{p0}}{\det \mathbf{F}_p} \right)^{1/2} F_{ij} \quad (8.3)$$

where \mathbf{F}_{p0} is computed at the centroid of the finite element.

The numerical tests are performed for the rectangular plate in tension with geometry and boundary conditions as in Section 5.6.1. Two discretizations are analyzed: mesh 1 and mesh 2, see Figure 6.7. The material model used for the simulations is ideal elasto-plasticity, see Section 5.1.2, with the following parameters: $K = 164.2e9 \text{ N/m}^2$, $G = 80.19e9 \text{ N/m}^2$ and $\sigma_{y0} = 0.45e9 \text{ N/m}^2$. The imperfection is obtained by the reduction of the initial yield strength by 1%.

The responses of the material simulated with *F-bar 2D* and *F-bar 3D* are depicted in Figure 8.1. The results are also compared with the results obtained for elements without the *F-bar* technique. It can be observed that for all models the diagrams at the beginning of the deformation process, when the deformation is uniform, are identical. For both two- and three-dimensional elements the lack of the modification preventing volumetric locking causes stiffer material response in the further part of the process. The results obtained with mesh 1 differ slightly for *F-bar 2D* and *F-bar 3D* (the three-

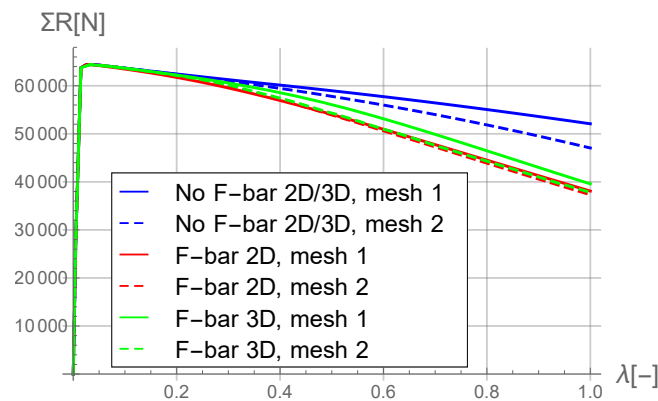


Figure 8.1: Sum of reactions vs enforced displacement multiplier for different finite elements and discretizations

dimensional model gives less softening), but for mesh 2 the results are very close to each other. The deformed mesh 2 for the *F-bar 2D* elements is presented in Figure 8.2, and is similar to the final configuration obtained for *F-bar 3D*. The deformation involves a wide shear band which, taking into account that no gradient enhancement is adopted in the analysed model, might be described as a diffuse form (necking).

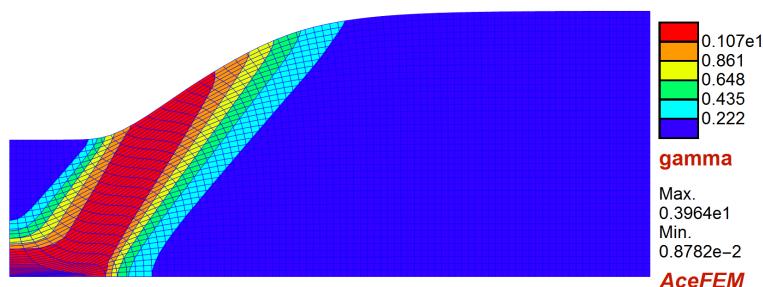


Figure 8.2: Deformed mesh 2 for *F-bar 2D* elements at the end of elongation process

To investigate the magnitude of the component $E_{33} = E_{zz}$ of the Lagrangian strain tensor for the *F-bar 3D* elements the evolution of its value along line crossing the

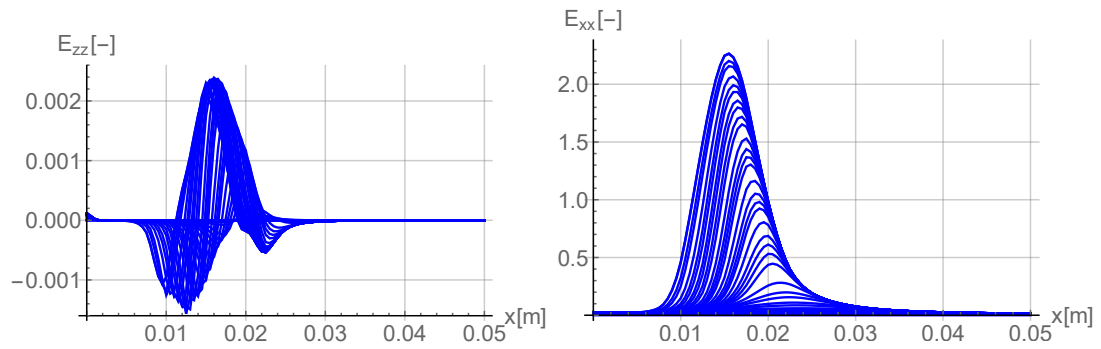


Figure 8.3: Evolution of components of Lagrangian strain tensor E_{zz} and E_{xx} along line crossing shear band and inclined 45 degrees with respect to longitudinal axis (see line A-B in Figure 6.11) for mesh 2

shear band and inclined 45 degrees in respect to longitudinal axis x in the reference configuration (see line A-B in Figure 6.11) is presented on the left in Figure 8.3. It can be observed that the component E_{zz} can be negative or positive and the largest absolute values are reached in the shear band. Comparing to component $E_{11} = E_{xx}$, see the right diagram in Figure 8.3, the maximum value of E_{zz} is only about 0.1% of the maximum value of E_{xx} .

To conclude, the application of the three-dimensional finite elements for the simulation of plane strain state gives correct results for the properly refined mesh.

Appendix B

Implementation of convective boundary condition¹

Let us assume convection on a part of the body surface denoted with $\partial\mathcal{B}_{q,conv}$, $\partial\mathcal{B}_{q,conv} \subset \partial\mathcal{B}_q$. Then the heat flux normal to the body surface can be computed using the equation

$$q_n = h_{conv}(T - T_\infty) \quad \text{on} \quad \varphi(\partial\mathcal{B}_{q,conv}) \quad (8.4)$$

where h_{conv} is the convection coefficient and T_∞ is the temperature of the surrounding medium.

The weak form of the energy balance equation involving convection has the form:

$$\int_{\mathcal{B}} \left(\delta T \frac{c}{\Delta t} (T - T_n) + \nabla \delta T k(T) \nabla T - \delta T \mathcal{R} \right) dV + \int_{\varphi(\partial\mathcal{B}_q - \partial\mathcal{B}_{q,conv})} \delta T \hat{q} da + \int_{\varphi(\partial\mathcal{B}_{q,conv})} \delta T h_{conv} (T - T_\infty) da = 0 \quad (8.5)$$

The contribution to the potential Π_{en} related to the convection, last integral in Equation (8.5), is defined as

$$\Pi_{conv} = \frac{1}{2} h_{conv} (T - T_\infty)^2 \quad (8.6)$$

The computation of Gauss point contribution to the residual vectors and tangent matrix due to convection is not performed directly in the thermomechanical three-dimensional finite element but is implemented through an additional surface finite elements. This approach simplifies the computation of the integral over a surface in the current configuration. For the three dimensional analysis with linear interpolation of both fields (elements H1/H1) the four noded 3D surface elements are used (elements S1). The mesh has to be generated in such a way that the nodes of the surface and of the three-dimensional elements coincide (S1 coincides with the side of H1 with convective BC), see Figure 8.4.

The Gauss point contributions to the residual vector and the element tangent matrix for the finite element S1 read

$$\mathbf{R}_G = w_G \cdot J_{xG} \frac{\partial \Pi_{conv}}{\partial \mathbf{p}} = [\mathbf{0}, \mathbf{R}_{conv,G}], \quad \mathbf{K}_G = \frac{\partial \mathbf{R}_G}{\partial \mathbf{p}} = \begin{pmatrix} \mathbf{0} & \mathbf{0} \\ \frac{\partial \mathbf{R}_{conv,G}}{\partial \mathbf{u}_I} & \frac{\partial \mathbf{R}_{conv,G}}{\partial \mathbf{T}_I} \end{pmatrix} \quad (8.7)$$

¹This section was published in paper [Wcislo and Pamin, 2017], Copyright ©2016 John Wiley & Sons, Ltd.

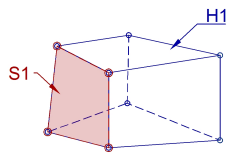


Figure 8.4: Surface element S1 for calculation of convection contribution

Appendix C

Temperature-dependent Young modulus for thermo-elasto-plasticity

In the thermo-elasto-plastic model analysed in Chapter 6 Young modulus is assumed to be temperature-independent. Now, this assumption is dropped and the simulation of the rectangular plate in tension in plane strain state analysed in Section 6.4.2 is repeated.

Let us assume that the hyperelastic response governed by the elastic free energy function written in Equation (5.5) depends on Young modulus and Poisson ratio instead of the bulk and shear moduli K and G , respectively. The relation between these sets of parameters is as follows

$$E = \frac{9KG}{3K + G}, \quad \nu = \frac{3K - 2G}{2[3K + G]} \quad (8.8)$$

The dependence between the increase of temperature and Young modulus is assumed, for simplicity, to be linear

$$E(T) = E_0 [1 - H_{TE} [T - T_0]] \quad (8.9)$$

where H_{TE} is a thermal softening modulus reducing E with temperature increase.

The numerical simulation is performed for the insulated plate in plane strain conditions presented in Section 6.4.2 with no external heat sources (the only source of temperature increase is the plastic heat dissipation). The material parameters are specified in Table 6.1 with the heat conduction coefficient equal to 100 J/(sKm). Parameters E_0 and ν are calculated using Equation (8.8) for the bulk and shear moduli from Table 6.1 (the corresponding initial value of Young modulus is $E = 207e9$ N/m² and Poisson ratio $\nu = 0.29$). Thermal softening parameter H_{TE} is equal to 10e-2 K⁻¹. The dependence of Young modulus on temperature for the adopted parameters is presented on the left in Figure 8.5. It can be observed that, for the adopted non-zero parameter H_{TE} , softening is so strong that the elastic stiffness is reduced to zero for temperature increase equal to 100 K. Obviously, this means that the model can be considered only in the limited range of temperatures.

The relation between the sum of reactions and the enforced displacement multiplier is presented on the right in Figure 8.5. It can be noticed that the diagrams for constant and temperature-dependent Young modulus coincide in the analysed example. It should also be mentioned, that the maximum value of the temperature increase is 47 K, thus it is in the admissible range.

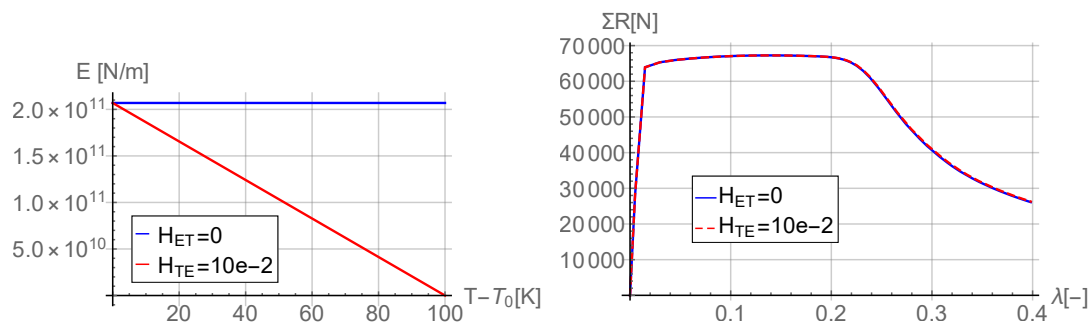


Figure 8.5: Young modulus vs temperature increase (on the left) and sum of reactions vs enforced load multiplier (on the right) for constant and temperature-dependent Young modulus (mesh 1)

In Figure 8.6 the deformed mesh with the distribution of Young modulus at the end of the deformation process is presented. It can be observed that indeed Young modulus decreases especially in the shear band. The highest reduction of the stiffness is in the imperfect finite element.

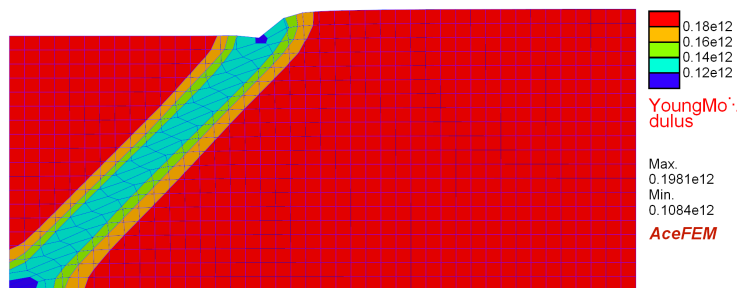


Figure 8.6: Deformed mesh with Young modulus distribution at the end of elongation process

To sum up, in the considered test of the elongated plate simulated with thermo-elasto-plasticity without external sources of heat the temperature-dependence of Young modulus does not influence the response of the whole sample significantly.

Bibliography

- [Abeyaratne and Knowles, 1999] Abeyaratne, R. and Knowles, J. K. (1999). On the stability of thermoelastic materials. *J. Elasticity*, 53:199–213. 25, 33
- [Aifantis, 1992] Aifantis, E. C. (1992). On the role of gradients in the localization of deformation and fracture. *Int. J. Engng Sci.*, 30:1279–1299. 92
- [Aifantis, 2014] Aifantis, E. C. (2014). Gradient material mechanics: Perspectives and prospects. *Acta Mechanica*, 225:999–1012. 28
- [Areias et al., 2003] Areias, P., César de Sá, J., and Conceição, C. (2003). A gradient model for finite strain elastoplasticity coupled with damage. *Finite Elements in Analysis and Design*, 39(13):1191–1235. 46
- [Asaro and Rice, 1977] Asaro, R. J. and Rice, J. R. (1977). Strain localization in ductile single crystals. *J. Mech. Phys. Solids*, 25:309–338. 43
- [Askes et al., 2002] Askes, H., Suiker, A. S. J., and Sluys, L. J. (2002). A classification of higher-order strain-gradient models - linear analysis. *Archive of Applied Mechanics*, 72(2-3):171–188. 28
- [Auricchio and Taylor, 1999] Auricchio, F. and Taylor, R. L. (1999). A return-map algorithm for general associative isotropic elasto-plastic materials in large deformation regimes. *Int. J. Plasticity*, 15:1359–1378. 52, 53
- [Bartels et al., 2015] Bartels, A., Bartel, T., Canadija, M., and Mosler, J. (2015). On the thermomechanical coupling in dissipative materials: A variational approach for generalized standard materials. *J. Mech. Phys. Solids*, (82):218–234. 77
- [Bažant and Pijaudier-Cabot, 1988] Bažant, Z. P. and Pijaudier-Cabot, G. (1988). Nonlocal continuum damage, localization instability and convergence. *ASME J. Appl. Mech.*, 55:287–293. 28
- [Belytschko and Lasry, 1989] Belytschko, T. and Lasry, D. (1989). A study of localization limiters for strain-softening in statics and dynamics. *Comput. & Struct.*, 33:707–715. 25
- [Benallal and Bigoni, 2004] Benallal, A. and Bigoni, D. (2004). Effects on temperature and thermo-mechanical couplings on material instabilities and strain localization of inelastic materials. *J. Mech. Phys. Solids*, 52:725–753. 25, 32, 33

- [Benallal and Marigo, 2007] Benallal, A. and Marigo, J.-J. (2007). Bifurcation and stability issues in gradient theories with softening. *Modell. Simul. Mater. Sci. Eng.*, 15(1):S283–S295. 25
- [Bigoni, 2012] Bigoni, D. (2012). *Nonlinear Solid Mechanics: Bifurcation Theory and Material Instability*. Cambridge University Press, Cambridge. 25, 97
- [Bobiński, 2006] Bobiński, J. (2006). *Implementation and application examples of non-linear concrete models with nonlocal softening*. Ph.D. dissertation, Gdansk University of Technology, Gdańsk. (in Polish). 28
- [Bonet and Wood, 2008] Bonet, J. and Wood, R. D. (2008). *Nonlinear continuum mechanics for finite element analysis*. Cambridge University Press, Cambridge, second edition. 19, 21, 23, 38, 126
- [Cottrell, 1964] Cottrell, A. (1964). *The Mechanical Properties of Matter*. John Wiley & Sons. 31
- [de Borst, 1991] de Borst, R. (1991). Simulation of strain localisation: A reappraisal of the Cosserat continuum. *Eng. Comput.*, 8:317–332. 28
- [de Borst, 2001] de Borst, R. (2001). Some recent issues in computational failure mechanics. *Int. J. Numer. Meth. Engng*, 52:63–95. 97
- [de Borst and Mühlhaus, 1992] de Borst, R. and Mühlhaus, H.-B. (1992). Gradient-dependent plasticity: Formulation and algorithmic aspects. *Int. J. Numer. Meth. Engng*, 35:521–539. 28
- [de Borst et al., 1993] de Borst, R., Sluys, L. J., Mühlhaus, H.-B., and Pamin, J. (1993). Fundamental issues in finite element analyses of localization of deformation. *Eng. Comput.*, 10:99–121. 25
- [de Souza Neto et al., 2008] de Souza Neto, E., Peric, D., and Owen, D. (2008). *Computational methods for plasticity. Theory and applications*. John Wiley & Sons, Ltd, Chichester, UK. 51, 52, 109
- [Dunwoody and Ogden, 2002] Dunwoody, J. and Ogden, R. W. (2002). On the thermodynamic stability of elastic heat-conducting solids subject to a deformation-temperature constraint. *Math. & Mech. of Solids*, 7:285–306. 25
- [Duszek et al., 1992] Duszek, M., Perzyna, P., and Stein, E. (1992). Adiabatic shear band localization in elastic-plastic damaged solids. *Int. J. Plasticity*, 8(4):361–384. 25
- [Egner, 2012] Egner, H. (2012). On the full coupling between thermo-plasticity and thermo-damage in thermodynamic modeling of dissipative materials. *Int. J. Solids Struct.*, 49(2):279–288. 74
- [Eringen, 1967] Eringen, A. C. (1967). *Mechanics of Continua*. J. Wiley & Sons, New York. 92

- [Forest and Aifantis, 2010] Forest, S. and Aifantis, E. (2010). Some links between recent gradient thermo-elasto-plasticity theories and the thermomechanics of generalized continua. *Int. J. Solids Struct.*, 47:3367–3376. 92
- [Forest and Lorentz, 2004] Forest, S. and Lorentz, E. (2004). Localization phenomena and regularization methods. In Besson, J., editor, *Local approach to fracture*, pages 311–370. Les Presses de l'École des Mines, Paris. 25, 26, 27
- [Geers, 2004] Geers, M. G. D. (2004). Finite strain logarithmic hyperelasto-plasticity with softening: a strongly non-local implicit gradient framework. *Comput. Methods Appl. Mech. Engrg.*, 193:3377–3401. 45, 46, 47, 128
- [Glema, 2004] Glema, A. (2004). Analysis of wave nature in plastic strain localization in solids. Technical Report Monograph 379, Poznań University of Technology, Poznań. (in Polish). 28
- [Gough, 1805] Gough, J. (1805). A description of a property of caoutchouc or indian rubber; with some reflections on the case of the elasticity of this substance. *Memoirs of the Literary and Philosophical Society of Manchester*, 1(7):288–295. 73
- [Gurtin et al., 2010] Gurtin, M. E., Fried, E., and Anand, L. (2010). *The mechanics and thermodynamics of continua*. Cambridge University Press, New York. 19, 126
- [Hill, 1958] Hill, R. (1958). A general theory of uniqueness and stability in elastic-plastic solids. *J. Mech. Phys. Solids*, 6:236–249. 25, 26, 126
- [Hill and Rice, 1972] Hill, R. and Rice, J. R. (1972). Constitutive analysis of elastic-plastic crystals at arbitrary strain. *J. Mech. Phys. Solids*, 20:401–413. 43
- [Holzapfel, 2000] Holzapfel, G. A. (2000). *Nonlinear Solid Mechanics. A Continuum Approach for Engineering*. John Wiley & Sons, Ltd, Chichester. 31, 73, 74, 130
- [Hughes, 1980] Hughes, T. J. R. (1980). Generalization of selective integration procedures to anisotropic and non-linear media. *Int. J. Numer. Meth. Engrg.*, 15:1413–1418. 51
- [Jirásek, 1998] Jirásek, M. (1998). Nonlocal models for damage and fracture: Comparison of approaches. *Int. J. Solids Struct.*, 35(31-32):4133–4145. 28
- [Jirásek, 2002] Jirásek, M. (2002). Objective modeling of strain localization. *Revue française de génie civil*, 6(6):1119–1132. 26
- [Joule, 1859] Joule, J. P. (1859). On some thermo-dynamic properties of solids. *Philosophical Transactions of the Royal Society of London*, A149(7):91–131. 73
- [Khen et al., 1998] Khen, R., Désoyer, T., and Dragon, A. (1998). Objective localization criterion and behaviour for finite deformation plasticity - a Lagrangian formulation. *Archive of Applied Mechanics*, 68:85–102. 29
- [Korelc, 2008] Korelc, J. (2008). Automation of the finite element method. In Wriggers, P., editor, *Nonlinear finite element methods*, pages 483–508. Springer-Verlag, Berlin Heidelberg. 40, 53

- [Korelc, 2009] Korelc, J. (2009). Automation of primal and sensitivity analysis of transient coupled problems. *Computational Mechanics*, 44:631–649. 50, 53, 54, 56
- [Korelc, 2011] Korelc, J. (2011). AceGen and AceFEM user manual. Technical report, University of Ljubljana. Available from: <http://symech.fgg.uni-lj.si>. 38, 39, 55, 127
- [Korelc and Stupkiewicz, 2014] Korelc, J. and Stupkiewicz, S. (2014). Closed-form matrix exponential and its application in finite-strain plasticity. *Int. J. Numer. Meth. Engng*, 13(98):960–987. 53
- [Kowalczyk-Gajewska, 2016] Kowalczyk-Gajewska, K. (2016). Discussion on ellipticity condition. *personal note*. 29, 127
- [Kroner and Teodosiu, 1974] Kroner, E. and Teodosiu, C. (1974). Lattice defect approach to plasticity and viscoplasticity. In Sawczuk, A., editor, *Problems of Plasticity*. Noordhoff, Leiden. 43
- [Lee, 1969] Lee, E. H. (1969). Elastic plastic deformation at finite strain. *ASME Trans. J. Appl. Mech.*, 36:1–6. 43
- [Lee and Liu, 1967] Lee, E. H. and Liu, D. T. (1967). Finite-strain elastic-plastic theory with application to plane-wave analysis. *J. Appl. Phys.*, 38:19–27. 43, 128
- [Lemaitre, 1984] Lemaitre, J. (1984). How to use damage mechanics. *Nucl. Engng Des.*, 80:233–245. 46
- [LeMonds and Needleman, 1986] LeMonds, J. and Needleman, A. (1986). Finite element analyses of shear localization in rate and temperature dependent solids. *Mechanics of Materials*, 5:339–361. 83
- [Liebe, 2003] Liebe, T. (2003). *Theory and numerics of higher gradient inelastic material behaviour*. Ph.D. dissertation, University of Kaiserslautern, Kaiserslautern. 27, 127
- [Liebe and Steinmann, 2001] Liebe, T. and Steinmann, P. (2001). Theory and numerics of a thermodynamically consistent framework for geometrically linear gradient plasticity. *Int. J. Numer. Meth. Engng*, 51:1437–1467. 28
- [Lu and Pister, 1975] Lu, S. C. H. and Pister, K. S. (1975). Decomposition of deformation and representation of the free energy function for isotropic thermoelastic solids. *Int. J. Solids Struct.*, 11:927–934. 74
- [Lubarda, 2004] Lubarda, V. A. (2004). Constitutive theories based on the multiplicative decomposition of deformation gradient: Thermoelasticity, elastoplasticity, and biomechanics. *Appl. Mech. Rev.*, 57:95–108. 74
- [Mandel, 1974] Mandel, J. (1974). Thermodynamics and plasticity. In Delgado, J. J., editor, *Foundations of Continuum Thermodynamics*. Macmillan, New York. 43
- [Maugin, 1992] Maugin, G. A. (1992). *The Thermomechanics of Plasticity and Fracture*. Cambridge University Press, Cambridge. 43, 74

- [Mazars and Pijaudier-Cabot, 1989] Mazars, J. and Pijaudier-Cabot, G. (1989). Continuum damage theory - application to concrete. *ASCE J. Eng. Mech.*, 115:345–365. 45
- [Menzel, 2002] Menzel, A. (2002). *Modelling and Computation of Geometrically Non-linear Anisotropic Inelasticity*. Ph.D. dissertation, University of Kaiserslautern, Kaiserslautern. 25
- [Miehe, 1995] Miehe, C. (1995). Entropic thermoelasticity at finite strains. aspects of the formulation and numerical implementation. *Comput. Methods Appl. Mech. Engrg.*, 120:243–269. 49
- [Mikkelsen, 1997] Mikkelsen, L. P. (1997). Post-necking behaviour modelled by a gradient dependent plasticity theory. *Int. J. Solids Struct.*, 34(35-36):4531–4546. 84
- [Müller and Ruggeri, 1993] Müller, I. and Ruggeri, T. (1993). *Extended thermodynamics*, volume 37. Springer Tracts in Natural Philosophy. 92
- [Okazawa, 2009] Okazawa, S. (2009). Structural bifurcation for ductile necking localization. *Int. J. Nonlinear Mech.*, 45:35–41. 33, 84
- [Pamin et al., 2017] Pamin, J., Wcisło, B., and Kowalczyk-Gajewska, K. (2017). Gradient-enhanced large strain thermoplasticity with automatic linearization and localization simulations. *J. Mech. Mater. Struct.*, 12(1):123–146. 16, 66, 92
- [Peerlings et al., 1996a] Peerlings, R. H. J., de Borst, R., Brekelmans, W. A. M., and de Vree, J. H. P. (1996a). Gradient-enhanced damage for quasi-brittle materials. *Int. J. Numer. Meth. Engng*, 39:3391–3403. 47, 129
- [Peerlings et al., 1996b] Peerlings, R. H. J., de Borst, R., Brekelmans, W. A. M., de Vree, J. H. P., and Spee, I. (1996b). Some observations on localisation in non-local and gradient damage models. *Eur. J. Mech. A/Solids*, 15:937–953. 28
- [Peerlings et al., 2001] Peerlings, R. H. J., Geers, M. G. D., de Borst, R., and Brekelmans, W. A. M. (2001). A critical comparison of nonlocal and gradient-enhanced softening continua. *Int. J. Solids Struct.*, 38(44-45):7723–7746. 47
- [Rice, 1976] Rice, J. R. (1976). The localization of plastic deformation. In Koiter, W., editor, *Proc. 14th Int. Cong. Theoretical and Applied Mechanics*, pages 207–220, Amsterdam. North-Holland Publishing Company. 25
- [Ristinmaa et al., 2007] Ristinmaa, M., Wallin, M., and Ottosen, N. S. (2007). Thermodynamic format and heat generation of isotropic hardening plasticity. *Acta Mechanica*, 194:103–121. 74, 77, 108
- [Rooney and Bechtel, 2004] Rooney, F. J. and Bechtel, S. E. (2004). Constraints, constitutive limits, and instability in finite thermoelasticity. *J. Elasticity*, 74:109–133. 25
- [Rots, 1988] Rots, J. G. (1988). *Computational modeling of concrete fracture*. Ph.D. dissertation, Delft University of Technology, Delft. 28

- [Rudnicki and Rice, 1975] Rudnicki, J. W. and Rice, J. R. (1975). Conditions for the localization of deformation in pressure-sensitive dilatant materials. *J. Mech. Phys. Solids*, 23:371–394. 25
- [Simo, 1992] Simo, J. (1992). Algorithms for static and dynamic multiplicative plasticity that preserve the classical return mapping schemes of the infinitesimal theory. *Comput. Methods Appl. Mech. Engrg.*, 99:61–112. 45
- [Simo, 1998a] Simo, J. (1998a). Numerical analysis and simulation of plasticity. In Ciarlet, P. and Lions, J., editors, *Handbook of Numerical Analysis*, volume IV, pages 183–499. Elsevier Science B.V., Boca Raton. 44
- [Simo, 1998b] Simo, J. (1998b). Numerical analysis and simulation of plasticity. In Ciarlet, P. and Lions, J., editors, *Handbook of Numerical Analysis. Numerical methods for solids (Part 3)*, volume VI, pages 183–499. Elsevier Science, Boca Raton. 49
- [Simo and Hughes, 1998] Simo, J. C. and Hughes, T. J. R. (1998). *Computational Inelasticity. Interdisciplinary Applied Mathematics Vol. 7*. Springer-Verlag, New York. 52
- [Simo and Miehe, 1992] Simo, J. C. and Miehe, C. (1992). Associative coupled thermoplasticity at finite strains: Formulation, numerical analysis and implementation. *Comput. Methods Appl. Mech. Engrg.*, 98:41–104. 44, 49, 74, 75, 76, 77, 78, 128, 130
- [Simo and Rifai, 1990] Simo, J. C. and Rifai, M. S. (1990). A class of mixed assumed strain methods and the method of incompatible modes. *Int. J. Numer. Meth. Engrg.*, 29:1595–1638. 51
- [Simone et al., 2003] Simone, A., Askes, H., Peerlings, R. H. J., and Sluys, L. J. (2003). Interpolation requirements for implicit gradient-enhanced continuum damage models. *Communications in Numerical Methods in Engineering*, 19:563–572. (see also [?]). 78
- [Sluys, 1992] Sluys, L. J. (1992). *Wave propagation, localization and dispersion in softening solids*. Ph.D. dissertation, Delft University of Technology, Delft. 25, 28, 89
- [Stankiewicz and Pamin, 2001] Stankiewicz, A. and Pamin, J. (2001). Simulation of instabilities in non-softening Drucker-Prager plasticity. *Computer Assisted Mechanics and Engineering Sciences*, 8:183–204. 26
- [Steinmann, 1999] Steinmann, P. (1999). Formulation and computation of geometrically non-linear gradient damage. *Int. J. Numer. Meth. Engrg.*, 46(5):757–779. 46, 62, 105
- [Steinmann et al., 1999] Steinmann, P., Runesson, K., and Larsson, R. (1999). On the analysis of adiabatic strong discontinuities within thermoplastic solids. In Bruhns, O. T. and Stein, E., editors, *IUTAM Symp. on Micro- and Macrostructural Aspects of Thermoplasticity*, Dordrecht. Kluwer Academic Publisher. 25
- [Stojanović et al., 1964] Stojanović, R., Djurić, S., and Vujošević, L. (1964). On finite thermal deformations. *Arch. Mech. Stos.*, 16:103–108. 74

- [Taylor, 1938] Taylor, G. I. (1938). Plastic strain in metals. *J. Inst. Met.*, 62:307–324. 43
- [Taylor and Quinney, 1934] Taylor, G. I. and Quinney, H. (1934). The latent energy remaining in a metal after cold working. *proc. Royal Soc. Lond. A*, 143:307–326. 77, 130
- [Tejchman and Wu, 1993] Tejchman, J. and Wu, W. (1993). Numerical study on patterning of shear bands in a Cosserat continuum. *Acta Mechanica*, 99(1-4):61–74. 28
- [Thomas, 1961] Thomas, Y. (1961). *Plastic Flow and Fracture of Solids*. Academic Press, New York. 25
- [Tvergaard, 1999] Tvergaard, V. (1999). Studies of elastic-plastic instabilities. *ASME J. Appl. Mech.*, 66:3–9. 25
- [Vardoulakis and Sulem, 1995] Vardoulakis, I. and Sulem, J. (1995). *Bifurcation Analysis in Geomechanics*. Blackie Academic & Professional, London. 25
- [Wcisło, 2016] Wcisło, B. (2016). Simulations of thermal softening in large strain thermoplasticity with degradatio. *Engineering Transaction*, 4(64):563–572. 76
- [Wcisło and Pamin, 2013] Wcisło, B. and Pamin (2013). Numerical simulations of strain localization for large strain damage-plasticity model. *Computer Methods in Materials Science*, 13(2):231–237. 16, 34
- [Wcisło and Pamin, 2014] Wcisło, B. and Pamin, J. (2014). Entropic thermoelasticity for large deformations and its AceGen implementation. In Łodygowski, T. et al., editors, *Recent Advances in Computational Mechanics, Proc. 20th International Conference on Computer Methods in Mechanics CMM-2013, Poznań, August 27-31, 2013*, pages 319–328, London. CRC Press/Balkema. First published as short paper in Proc. 20th International Conference on Computer Methods in Mechanics CMM-2013, Poznań, August 2013, p. TS03-13-14. 74
- [Wcisło and Pamin, 2017] Wcisło, B. and Pamin, J. (2017). Local and non-local thermomechanical modeling of elastic-plastic materials undergoing large strains. *Int. J. Numer. Meth. Engng*, 109(1):102–124. 16, 74, 79, 83, 92, 94, 95, 113
- [Wcisło et al., 2013] Wcisło, B., Pamin, J., and Kowalczyk-Gajewska, K. (2013). Gradient-enhanced damage model for large deformations of elastic-plastic materials. *Arch. Mech.*, 65(5):407–428. 16, 55
- [Winnicki et al., 2001] Winnicki, A., Pearce, C. J., and Bićanić, N. (2001). Viscoplastic Hoffman consistency model for concrete. *Comput. & Struct.*, 79:7–19. 28
- [Wriggers, 2008] Wriggers, P. (2008). *Nonlinear finite element methods*. Springer-Verlag, Berlin Heidelberg. 19, 126

- [Wriggers et al., 1992] Wriggers, P., Miehe, C., Kleiber, M., and Simo, J. (1992). On the coupled thermomechanical treatment of necking problems via finite element methods. *Int. J. Numer. Meth. Engng*, 33:869–883. 74, 75, 76, 77
- [Yang et al., 2006] Yang, Q., Stainier, L., and Ortiz, M. (2006). A variational formulation of the coupled thermo-mechanical boundary-value problem for general dissipative solids. *J. Mech. Phys. Solids*, 54:401–424. 108
- [Żebro et al., 2008] Żebro, T., Kowalczyk-Gajewska, K., and Pamin, J. (2008). A geometrically nonlinear model of scalar damage coupled to plasticity. *Technical Transactions*, 20:251–262. Series Environmental Engineering 3-Ś/2008. 46
- [Zienkiewicz and Taylor, 1989] Zienkiewicz, O. C. and Taylor, R. L. (1989). *The Finite Element Method*. McGraw-Hill, London, fourth edition. 37, 127

Streszczenie

Termomechaniczne modele materiału uwzględniające duże odkształcenia, niesprężystość, niestateczność i regularyzację gradientową

ROZDZIAŁ 1: WPROWADZENIE

W eksperymentach laboratoryjnych przeprowadzanych na takich materiałach jak metale, ich stopy lub kompozyty można zaobserwować duże (często trwałe) odkształcenia, którym niejednokrotnie towarzyszy lokalizacja odkształceń w pewnej objętości materiału, gdy pozostała jego część ulega odciążeniu. Zjawisko to, którego przyczynami mogą być degradacja materiału, osłabienie termiczne lub efekty geometryczne może prowadzić nawet do zniszczenia materiału. Takie zachowanie, mimo iż jest obserwowane w skali makro, może mieć swoje źródło w mikrostrukturze, np. przez powstawanie mikrouszkodzeń. Istotnym aspektem, którego nie powinno się pominąć w modelowaniu konstytutywnym jest sprzężenie termomechaniczne, które może mieć duży wpływ na zachowanie materiału, a przejawia się m.in. przez zależność parametrów materiałowych od temperatury czy wytwarzanie ciepła w czasie procesu plastycznego.

Wraz z rozwijającymi się technologiami informatycznymi obok podstawowych filarów nauki, jakimi są teoria i eksperyment pojawił się trzeci element - symulacja komputerowa. Testy numeryczne, które pozwalają na weryfikację formułowanych modeli materiałowych, niejednokrotnie wymagają przygotowania własnych procedur. Dlatego też wykorzystywanie nowych metod usprawniających proces implementacji modeli jest bardzo ważne.

Mając na uwadze powyższe aspekty, celem badań prowadzonych w ramach projektu doktorskiego jest sformułowanie i numeryczna weryfikacja modeli materiału uwzględniających nieliniowe związki geometryczne (duże odkształcenia) i konstytutywne (plastyczność, uszkodzenie) ze zwróceniem szczególnej uwagi na niestateczne zachowanie materiału. W pierwszej kolejności analizowane są modele izotermiczne, następnie modele z pełnym sprzężeniem termomechanicznym.

Rozwijane modele mogą opisywać materiały takie jak metale lub izotropowe kompozyty, jednakże w pracy uwaga jest poświęcona przede wszystkim modelowaniu pewnych

zachowań materiału i zjawisk zachodzących w czasie dużych deformacji, a nie dostosowaniu opisu do konkretnego materiału. Modele materiałów przedstawione w pracy są fenomenologiczne, ale przez zastosowanie uśredniania gradientowego i związanej z nim wewnętrznej skali długości, mogą uwzględniać efekty mające swoje źródło w mikrostrukturze materiału. Co więcej, z punktu widzenia mechaniki obliczeniowej, zastosowane uśrednianie regularyzuje opis kontinuum, powodując, że problem brzegowy nie traci eliptyczności.

Testy numeryczne, których wyniki zaprezentowane są w dysertacji, zostały wykonane w środowisku obliczeniowym *AceFEM*, z kolei wszystkie procedury skończenie elementowe dla modelowanych materiałów opracowano samodzielnie przy użyciu generatora kodów *AceGen*, który wyposażony jest w automatyczne różniczkowanie (ang. *automatic differentiation* – *AD*) i optymalizację wyrażeń. W pracy przyjęte są następujące założenia: ciągłość i izotropia materiału, związki fizyczne opisujące sprężystość, plastyczność ze stowarzyszonym prawem płynięcia bez członów wiskotycznych. Zostały pominięte efekty bezwładnościowe, ale w modelach termomechanicznych uwzględniono nieustalony przepływ ciepła. Wszystkie opisy materiałów, algorytmy i kody skończenie elementowe są rozwijane dla przestrzeni trójwymiarowej.

ROZDZIAŁ 2: PODSTAWY PROBLEMU DUŻYCH ODKSZTAŁCEŃ

W Rozdziale 2 przedstawione są podstawowe sformułowania i definicje potrzebne do opisu materiału ulegającego dużym odkształceniom na podstawie literatury [Bonet and Wood, 2008, Wriggers, 2008, Gurtin et al., 2010]. W pierwszej kolejności wprowadzone są fundamentalne pojęcia jak konfiguracja odniesienia i aktualna, opis materialny i przestrzenny, funkcja ruchu oraz przemieszczenie. Następnie przedstawiono podstawowe miary deformacji i naprężenia oraz różniczkowanie wybranych wielkości względem czasu. W ostatnim podrozdziale zawarte są sformułowania mocy sił wewnętrznych dla różnych, sprzężonych ze sobą, miar deformacji i naprężenia.

ROZDZIAŁ 3: NIESTATECZNOŚĆ

Lokalizacja odkształceń, która dla rozciąganych próbek może przyjmować formę pasm ścinania lub szyjki jest ściśle związana z pojęciem utraty stateczności, które może mieć swoje źródło w osłabieniu materiału, efektach geometrycznych lub wynikać z wpływu temperatury na zachowanie materiału.

Pojęcie niestateczności materiału zostało przedstawione po raz pierwszy w pracy [Hill, 1958], w której materiał określono jako stateczny, gdy spełniona jest następująca zależność określona dla prędkości tensora odkształcenia $\dot{\epsilon}$ i tensora naprężenia $\dot{\sigma}$

$$\dot{\epsilon} : \dot{\sigma} > 0$$

Niejednokrotnie wraz z utratą stateczności można w materiale zaobserwować pojawienie się powierzchni nieciągłości, na której występuje skok gradientu prędkości. Analiza równowagi na takiej powierzchni nieciągłości z uwzględnieniem związków kon-

stytutowych prowadzi do sformułowania warunku zachowania eliptyczności, w którym wyznacznik tensora akustycznego ma być dodatni. Warto wspomnieć, że warunek utraty eliptyczności może być również wyprowadzony z analizy propagacji fal w materiale, zobacz np. [Liebe, 2003].

Jeżeli opis materiału uwzględni nieliniowości geometryczne, to warunek równowagi na powierzchni nieciągłości, a co za tym idzie tensor akustyczny, mogą być sformułowane na kilka sposobów, w zależności od przyjętych miar naprężenia i odkształcenia.

W pracy zaprezentowano pilotażowe wyniki badań warunku eliptyczności przy użyciu definicji tensora akustycznego obliczonego na podstawie pierwszego tensora naprężenia Pioli-Kirchhoffa i gradientu deformacji [Kowalczyk-Gajewska, 2016]. Analiza przeprowadzona jest dla rozciąganej idealnie sprężysto-plastycznej płytki w płaskim stanie odkształcenia.

W dalszej części Rozdziału 4 omówiony jest wpływ temperatury na niestateczne zachowanie materiału. W niniejszej pracy osłabienie termiczne materiału jest zdefiniowane jako degradacja granicy plastyczności wraz ze wzrostem temperatury, który może być powodowany przez ciepło pochodzące z dysypacji plastycznej. Uwzględnienie w opisie sprzężenia termomechanicznego może mieć efekt regularyzacyjny dzięki przewodności cieplnej. Warto również dodać, że dla modelu termomechanicznego warunek równowagi na powierzchni nieciągłości jest uzupełniony o dodatkowy warunek zerowego skoku temperatury, strumienia ciepła i jego pochodnej po czasie.

W ostatniej części Rozdziału 4 zwięźle omówiono na czym polega osłabienie geometryczne dla modelu sprężysto-plastycznego oraz zaprezentowano przykłady zjawiska lokalizacji w rozciągającym przecie, które mogą przyjmować formę zlokalizowaną (*localized*) lub rozproszoną (*diffuse*).

ROZDZIAŁ 4: PODEJŚCIE OBLICZENIOWE

Modele materiału analizowane w pracy zawierają nieliniowości geometryczne (duże odkształcenia), materiałowe (plastyczność, uszkodzenie), uśrednianie gradientowe oraz pełne sprzężenie termomechaniczne. Weryfikacja tak złożonych modeli jest dokonywana za pomocą symulacji komputerowych, gdyż ich rozwiązanie analityczne jest praktycznie niemożliwe. Do numerycznego rozwiązania zagadnienia brzegowego zastosowano metodę elementów skończonych (MES) [Zienkiewicz and Taylor, 1989], która jest powszechnie stosowana do rozwiązywania problemów mechaniki ciała stałego. Prezentowane modele w większości nie są oprogramowane w dostępnych programach MES, zatem konieczne było przygotowanie własnych procedur skończenie elementowych. Układ równań nieliniowych wynikający z aproksymacji zagadnienia jest rozwiązywany metodą Newtona-Raphsona, której główną zaletą jest kwadratowa zbieżność, jednakże metoda ta wymaga przeprowadzenia kosztownej obliczeniowo linearyzacji równań.

Implementacja wszystkich modeli zaprezentowanych w dysertacji została przeprowadzona przy użyciu symboliczno-numerycznych pakietów *AceGen/FEM* [Korelc, 2011] pracujących w środowisku *Wolfram Mathematica*. Pierwszy z pakietów jest generatorem kodów wyposażonym w optymalizację wyrażeń i automatyczne różniczkowanie – szczególnie istotne z punktu widzenia linearyzacji zagadnienia brzegowego. Na bazie

kodu napisanego w specjalnym meta-języku można wygenerować procedury w języku *C*, *FORTRAN* i innych, jak również pliki wsadowe dla dostępnych programów MES jak *ABAQUS* czy *FEAP*.

Drugi z pakietów – *AceFEM*, jest programem MES, który zawiera solver oraz pre i postprocesor, obsługiwane z poziomu notatnika programu *Mathematica*. Istotną jego zaletą jest doskonała współpraca z generatorem kodów oraz pełna kontrola użytkownika nad parametrami symulacji i przebiegiem obliczeń (np. przez dostępną paletę debugera).

Zastosowanie symboliczno-numerycznego oprogramowania wymaga opracowania specjalnych algorytmów. Zgodnie z rekomendacją autora pakietów, w pracy zastosowano podejście bazujące na potencjałach budowanych dla równań rządzących – tak otrzymany kod jest efektywny obliczeniowo. W podejściu tym, należy zdefiniować wektor stopni swobody oraz interpolację niewiadomego pola, a następnie potencjał dla równań bilansowych. Na podstawie poprawnie określonych zależności między niewiadomymi a potencjałem, korzystając z automatycznego różniczkowania, można obliczyć wektor residuum na poziomie punktu całkowania (jako pochodną potencjału względem wektora stopni swobody) oraz macierz styczną (jako pochodną residuum względem wektora stopni swobody). Warto zaznaczyć, że użytkownik może dodać do procesu automatycznego różniczkowania pewne dodatkowe informacje (często niezbędne dla poprawności rozwiązania) poprzez tzw. wyjątki (*AD exceptions*).

ROZDZIAŁ 5: IZOTERMICZNE NIESPREŻYSTE MODELE MATERIAŁÓW

W Rozdziale 5 uwaga skupiona jest na modelowaniu materiałów w warunkach izotermicznych. Pierwsze podrozdziały zawierają opis kinematyki dla problemu sprężysto-plastycznego, bazujący na multiplikatywnym rozkładzie gradientu deformacji [Lee and Liu, 1967], definicję energii swobodnej oraz związki konstytutywne plastyczności [Simo and Miehe, 1992]. W dalszej części rozdziału przedstawione są dwa lokalne modele opisujące osłabienie materiału wywodzące się z przedstawionego wcześniej modelu sprężysto-plastycznego. Pierwszy z nich to model z uszkodzeniem (*elasto-plasticity with damage*), w którym sprężysta energia swobodna jest redukowana przez człon zależny od skalarnego parametru uszkodzenia. Parametr ten, oparty na pewnej mierze odkształcenia, może przyjmować wartości od 0 dla nieuszkodzonego do 1 dla całkowicie zniszczonego materiału. W pracy zaproponowano dwie takie miary odkształcenia, jedna z nich uwzględnia zmianę objętości materiału, a druga jest obliczana na podstawie dodatnich wartości głównych tensora odkształceń Almaziego. O tym, czy w materiale dojdzie do uszkodzenia i jego ewolucji decyduje kryterium uszkodzenia.

Drugi model uwzględnia degradację granicy plastyczności przez człon zależny od plastycznego parametru uszkodzenia [Geers, 2004]. W pracy jest on powiązany ze skalarną miarą odkształceń plastycznych.

Aby uniknąć utraty dobrego postawienia zagadnienia brzegowego dla powyższych modeli zawierających komponenty powodujące osłabienie materiału, opisy te wzbogacono o gradienty wyższego rzędu przez użycie uśredniania typu *implicit* [Peerlings et al.,

1996a]

$$z - l^2 \nabla^2 z = z_{loc} \quad (8.10)$$

Powyższe równanie określa zależność między wielkością lokalną z_{loc} a jej nielokalnym (uśrednionym) odpowiednikiem z . Parametr l jest wewnętrzną skalą długości, która wpływa na szerokość strefy lokalizacji odkształceń. Regularyzacja gradientowa w modelach z uszkodzeniem i degradacją jest zrealizowana przez zastąpienie zmiennych lokalnych, które wywołują osłabienie, ich nielokalnymi odpowiednikami. Warto zwrócić uwagę, że w geometrycznie nieliniowym modelu uśrednianie można wykonać w konfiguracji odniesienia (uśrednianie materialne) lub aktualnej (uśrednianie przestrzenne).

W dalszej kolejności przedstawione są równania zagadnienia brzegowego oraz podejście numeryczne i stosowne algorytmy.

Pozostała część Rozdziału 5 zawiera wyniki symulacji numerycznych wykonanych dla przedstawionych modeli izotermicznych. Dla gradientowego modelu sprężysto-plastycznego z uszkodzeniem wykonano symulacje rozciąganego pręta o zmiennym kwadratowym przekroju oraz rozciąganej płytki perforowanej. Analizie zostały poddane wybrane aspekty:

- *Zastosowanie różnych elementów skończonych.*

Wykonano serię symulacji dla różnych wariantów modelu i następujących elementów skończonych: H1, H1 z F -bar i H2S. Dla elementów H1 uzyskano wyniki z fałszywym wzmocnieniem spowodowanym przez zjawisko blokady (*locking*). Ze względu na kosztowność obliczeń wykonywanych dla elementów z kwadratową interpolacją przemieszczeń, kolejne symulacje są wykonane tylko dla elementów z modyfikacją F -bar, które dawały zbliżone wyniki do tych otrzymanych przy użyciu H2S.

- *Porównanie uśredniania materialnego i przestrzennego*

Analizie poddano rozciągany pręt o zmiennym przekroju wykonany z materiału opisanego nielokalnym modelem sprężystym z uszkodzeniem (dla tej grupy testów pominięto zachowanie plastyczne). Analiza wykazała, że uśrednianie przestrzenne nie chroni w pełni przed zależnością wyników od siatki w przeciwieństwie do uśredniania materialnego.

- *Testowanie zaproponowanych miar odkształcenia rządzących uszkodzeniem*

Przeprowadzone symulacje wykazały, że w przypadku materiału sprężystego z uszkodzeniem odpowiedź materiału jest inna dla różnych miar odkształcenia, natomiast nie wpływają one jednak znacząco na wyniki dla modelu sprężonego z plastycznością.

- *Analiza różnych funkcji plastyczności*

Przebadano zachowanie materiału, dla którego zakres plastyczny jest opisany przez funkcje plastyczności Hubera-Misesa-Henckyiego (HMH) lub Burzyńskiego-Druckera-Pragera (BDP). Testy wykazały, że dobór funkcji może mieć istotny wpływ na odpowiedź materiału sprężysto-plastycznego z uszkodzeniem.

Nielokalny model sprężysto-plastyczny z degradacją został następnie przetestowany na rozciąganej prostokątnej płycie w płaskim stanie odkształcenia. Testy wykonane dla dwóch typów elementów skończonych (z modyfikacją F -bar oraz bez niej) wykazały, że zwykle elementy z liniową interpolacją symulują fałszywe wzmocnienie, które może powodować jakościowo inną odpowiedź materiału – brak zlokalizowanej formy deformacji. Dla elementów z F -bar uśrednianie gradientowe determinuje szerokość strefy lokalizacji i powoduje brak zależności wyników od zastosowanej siatki elementów skończonych. Porównanie wybranych wyników dla płaskiego stanu odkształcenia przy użyciu dwu i trójwymiarowych elementów z F -bar jest zawarte w Załączniku A.

ROZDZIAŁ 6: LOKALNY TERMOMECHANICZNY MODEL MATERIAŁU ULEGAJĄCYCH DUŻYM ODKSZTAŁCENIOM

Rozdział 6 jest poświęcony geometrycznie nieliniowemu modelowi termo-sprężysto-plastycznemu bez włączenia do opisu gradientów wyższego rzędu. Model ten zawiera pełne sprzężenie termomechaniczne, tzn. rozszerzalność cieplną, zależność parametrów materiałowych od temperatury, wpływ zmiany geometrii na przepływ ciepła oraz wytwarzanie ciepła w procesie plastycznym. W pracy uwaga jest poświęcona materiałom energetycznym [Holzapfel, 2000]. W rozdziale przedstawiono równania konstytutywne dla termo-sprężysto-plastyczności bazujące na publikacji [Simo and Miehe, 1992], która uwzględnia: hipersprężystość, stowarzyszoną plastyczność z miarą naprężeń HMH, izotropowym wzmocnieniem liniowym i saturacyjnym oraz liniowym termicznym osłabieniem. Strumień ciepła jest określony przez prawo Fouriera, a ciepło pochodzące z plastycznej dysypacji energii jest zdefiniowane w sposób uproszczony korzystając z podejścia [Taylor and Quinney, 1934].

Po omówieniu implementacji analizowanego dwupolowego modelu w pakietach *AceGen/FEM*, przedstawione są wyniki symulacji numerycznych. W pierwszej kolejności analizie jest poddany rozciągany pręt o przekroju kołowym, dla którego jedynym źródłem zaburzenia jest konwekcja na całej zewnętrznej powierzchni (implementacja warunków konwekcyjnych została omówiona w Załączniku B). W trakcie procesu rozciągania odkształcenia lokalizują się w szyjce (forma *diffuse*). Przewodność cieplna wpływa w tym przypadku na wyniki w sposób ilościowy, a nie na formę deformacji końcowej. Z kolei w przypadku analizowanej prostokątnej płytki w płaskim stanie odkształcenia przewodność cieplna znacząco wpływa na wyniki. W zależności od wartości współczynnika przewodności cieplnej k pasmo ścinania przyjmuje różną szerokość, a dla przypadku adiabatycznego lub małego k obejmuje dwa rzędy elementów, co wpływa na zależność wyników od dyskretyzacji.

Ostatnia część Rozdziału 6 obejmuje wyniki symulacji rozciągania płytki przeprowadzonego z różną prędkością. Przedstawione wyniki potwierdzają silną zależność właściwości regularyzacyjnych przewodnictwa od czasu trwania procesu: dla próbek rozciąganych szybciej odpowiedź konstrukcji była zbliżona do przypadku adiabatycznego, dla próbek rozciąganych wolniej - przewodność powoduje większą ciągliwość materiału i wpływa na poszerzenie strefy lokalizacji. Warto zaznaczyć, że jest to efekt odwrotny do wpływu członów wiskotycznych, które powodują, że zwiększenie prędkości odkształ-

cenia lepiej regularyzuje odpowiedź materiału.

ROZDZIAŁ 7: NIELOKALNE TERMOMECHANICZNE MODELE MATERIAŁU ULEGAJĄCEGO DUŻYM ODKSZTAŁCENIOM

W tym rozdziale przedstawione są dwa modele termo-sprężysto-plastyczne ze wzbogaceniem gradientowym zrealizowanym przez uśrednianie typu implicit (jak w Rozdziale 5). Modele te mogą być szczególnie przydatne, gdy konieczne jest wprowadzenie regularyzacji do opisu termo-sprężysto-plastycznego, np. gdy przewodność cieplna jest niewielka bądź równa zero (przypadek adiabatyczny).

Pierwszy z zaprezentowanych modeli zawiera uśrednianie przyrostu temperatury, który wpływa na redukcję granicy plastyczności. Symulacje numeryczne wykonane dla rozciąganego pręta o przekroju kołowym i prostokątnej płytki dla przypadku adiabatycznego potwierdziły regularyzacyjne właściwości zastosowanego uśredniania. Porównując otrzymane rezultaty z wynikami uzyskanymi dla lokalnego modelu termo-sprężysto-plastycznego (Rozdział 6) można stwierdzić, że globalna odpowiedź analizowanych próbek dla różnych wartości przewodności cieplnej jest podobna do odpowiedzi uzyskanej dla przypadku adiabatycznego i różnych wartości wewnętrznej skali długości dla uśredniania wzrostu temperatur. Obserwowane są jednak różne przyrosty temperatury w próbkach. Wykonano również testy modelu gradientowego z przewodnością cieplną. W takiej symulacji otrzymano ewoluujące pasmo ścinania, które w trakcie deformacji poszerza się, a jego ekstremum się przesuwa.

Drugi model jest termomechanicznym rozszerzeniem gradientowego modelu sprężysto-plastycznego z degradacją. Teraz granica plastyczności jest redukowana nie tylko przez wzrost parametru plastycznego uszkodzenia, ale i przez wzrost temperatury, a regularyzacja może być otrzymana przez przewodność cieplną lub uśrednianie gradientowe. Symulacje rozciąganej prostokątnej płytki wykonano zatem dla trzech przypadków: regularyzacja tylko przez przewodność, tylko przez uśrednianie lub obie jednocześnie. Dla przypadku adiabatycznego i uśredniania gradientowego można zaobserwować regularne pasmo zlokalizowanych odkształceń, którego szerokość zależy od wewnętrznej skali długości. Dla samej przewodności pasma te są mają wygięty kształt. Natomiast zastosowanie obu regularyzacji powoduje, że na końcu procesu deformacji pasmo jest szerokie i lekko zakrzywione.

ROZDZIAŁ 8: PODSUMOWANIE

Niniejsza praca prezentuje opisy konstytutywne i symulacje numeryczne modeli materiału, które zawierają duże odkształcenia, nielokalność, nieliniowe związki fizyczne w izotermicznych i nieizotermicznych warunkach ze szczególnym uwzględnieniem analizy niestatecznego zachowania materiału. W pierwszych wprowadzających rozdziałach przedstawiono podstawy geometrycznie nieliniowej mechaniki, omówiono różne rodzaje niestateczności oraz zastosowane narzędzia obliczeniowe. Kolejny rozdział został poświęcony modelom izotermicznym obejmującym nielokalną sprężysto-plastyczność z uszko-

dzeniem lub degradacją. Wykonano symulacje numeryczne pozwalające na zbadanie wybranych aspektów, np. jak sposobu uśredniania gradientowego. W dalszej części pracy przedstawiono termo-sprężysto-plastyczny model materiału i wykonano symulacje rozciąganego pręta i płytki w płaskim stanie odkształcenia. Zbadano wpływ przewodności cieplnej na lokalizację odkształceń. Następnie zaproponowano dwa modele termo-sprężysto-plastyczne z uśrednianiem gradientowym i przetestowano je dla przypadku adiabatycznego oraz dla przypadku z przewodnością cieplną.

Dla wszystkich przedstawionych w pracy modeli opracowano stosowne algorytmy i procedury dla MES. Warto jeszcze raz podkreślić znaczenie zastosowanych narzędzi symboliczno-numerycznych *AceGen/FEM*. Dzięki nim linearyzacja równań konstytutywnych była wykonywana automatycznie przez technikę AD. Pakiety te są względnie nowe, dlatego w dysertacji poświęcono dużo uwagi na przedstawienie podejścia i algorytmów bazujących na potencjałach opracowanych dla rozwijanych modeli.

Ostatni rozdział zawiera również możliwe kierunki pracy, będące kontynuacją projektu doktorskiego. Obejmują one m.in.: analizę innych nielokalnych modeli (np. gradientowa plastyczność), porzucenie założenia o izotropii materiału, rozszerzenie opisu o dynamikę i człony wiskotyczne w plastyczności oraz badanie eliptyczności dla sprzężonych modeli termomechanicznych.